Study of Eukaryotic Cellular Process by Mathematical Modeling: Chemotaxis and Mitosis

by

Changji Shi

A dissertation submitted to The Johns Hopkins University in conformity with the requirements for the degree of Doctor of Philosophy.

Baltimore, Maryland

March, 2014

Abstract

Chemotaxis, the directed cell movement in response to external chemical gradients, is a vital biological process. Single cell organisms, such as bacteria and amoebae, rely on chemotaxis for feeding. In multicellular organisms, it plays an important role during embryogenesis, the immune system, wound healing, and in cancer metastasis.

In eukaryotic cells, a complex signaling system involving over one hundred biochemical components and numerous redundant pathways mediates chemotaxis. Because of the complexity of this system, it has proved to be advantageous to study chemotaxis by isolating the chemotactic response into a set of simpler processes: motility, gradient sensing, and polarization. Research into chemotaxis has also benefited from numerous theoretical and computational treatments that complement experimental studies.

Here, we developed a computational framework using a modular view of the chemotactic behavior in *Dictyostelium* cells. The starting point is a proposed model that suggests that cells rely on firings of an excitable network to generate pseudopods. In the absence of chemoattractant stimuli, these firings are triggered by stochastic

Abstract

perturbations in the signaling system. However, chemottractants bias the location of the firings by altering the level of the threshold. Here, we carry out tests of this local-excitation, global-inhibition biased excitable network (LEGI-BEN) hypothesis. In particular, we couple the model to a viscoelastic description of the cell and test through simulation how well the model recreates the observed behavior of chemotactic cells. Based on these simulations and on new experimental findings, we propose several modifications to the existing model. One additional component incorporates a polarity module that endows cell movement with persistence. A second addition is an oscillatory cytoskeletal network that recreates fast oscillations observed in cells.

In addition to the research in chemotaxis, this dissertation also reports on the development of a mathematical model describing mitotic matrix formation after nuclear envelope breakdown. Recent reports show that lamin B, a component of the nuclear lamina in interphase, localizes around the spindle and reassembles to form a mitotic matrix. How this process occurs, however, and what effect it has on the mitotic spindle is unclear. Here, we develop a computational model based on a continuum description to represent the abundance and location of the various molecular species involved during mitosis. We use this model to examine the role for the matrix during spindle formation and to test between several hypotheses regarding the formation of the mitotic matrix.

Primary Reader: Pablo A. Iglesias

Secondary Reader: Peter N. Devreotes

Acknowledgments

I have received so much help and support from a lot of people while working on this dissertation. I could not have gotten so far without them. First of all, I should thank my advisor, Dr. Pablo Iglesias. Pablo taught me and helped me with endless patience, insightful guidance, and generous support through my Ph.D.. I also would like to thank Dr. Peter Deverotes, who has been my second advisor and an excellent collaborator. I also wish to thank Dr. Yixian Zheng, with whom we collaborated of the mitotic spindle matrix formation project. I need to thank all the collaborators from the Department of Cell Biology. Chuan-Hsiang Huang helped me to work on the polarity project described in Chapter 5. He and Ming Tang were both collaborators in the cytoskeletal oscillating network project described in Chapter 6. In addition, Ming-Jie Wang worked with me in the coupling of adaptive and excitable networks project. Additionally, I would like to thank the members of the Iglesias lab, particularly Krithika Mohan, Yuan Xiong, Chris Poirier, Josh Porter, and Wilbur Channels, as well as the other members of the Devreotes lab and Doug Robinson's lab for their advice and encouragement.

Acknowledgments

Especially, I would like to thank my wife Muzi Na. She is always my biggest supporter in life. She gives me enormous encouragement, patience, love and intellectual inspiration. I am also grateful to my parents, Xiaoping Shi and Xingyun Cheng for their support and love throughout my life. Finally, I want to thank my friends at Hopkins for so much happy time here.

Dedication

This thesis is dedicated to my wife, Muzi Na.

Contents

Contents

Contents

List of Tables

List of Figures

List of Figures

Chapter 1

Introduction

This dissertation describes a number of mathematical models used to study two essential cellular processes: chemotaxis and mitosis.

1.1 Chemotaxis

Many cells have the ability to move around in their environment, and often they use an internal "compass" that enables them to sense, and direct their migration along gradients of extracellular chemicals (chemotaxis), electric fields (electrotaxis), or mechanical forces (mechanotaxis). Chemotaxis is vital to a wide range of biological processes and fundamental to the proper development and functioning of eukaryotic organisms [1]. For example, chemotaxis is important for cell migration events, organ formation, and wiring of the nervous system during embryogenesis. Chemotaxis is critical for the trafficking of immune cells and in inflammation, regenerative processes

such as wound healing, and maintenance of tissue architecture [2]. During cancer metastasis, cells escape the primary tumor, enter the circulation, and emigrate to specific tissues by chemotaxis [3]

Chemotaxis is a complex mechanochemical process and can be conceptually divided into three separate but interrelated processes: motility, gradient sensing, and polarization [1]. The whole process needs perfect incorporation of numerous key events in signaling, cytoskeletal, membrane, and adhesion systems. Although different kinds of chemotactic cells have cell type-specific and stimulation-dependent morphological and functional characteristics, the chemotactic behaviors are very similar in human leukocytes and free-living amoebae [4], indicating that a unified mechanisms of chemotaxis might be conserved among eukaryotic cells. Thus, a mathematical framework may reveal the underlying mechanism of chemotaxis despite the seemingly diverse behavior of cells.

To accomplish this theoretical work, we need mathematical tools that explain various functions of cells, such as the spatial and temporal signaling response to stimuli, polarization and shape change, directional migration and cytoskeletal organization. These tools include mathematical models of signaling networks, image processing algorithms and simulation methods that can incorporate cell shape changes, etc.

As it will be reviewed in Chapter 2, there are already many models proposed to explain chemotaxis. However, none of the existing models can account for all behaviors observed in chemotaxing cells. Thus, one of the main goals of my research has

been developing a comprehensive, unified mathematical framework that incorporates all experimental observations. To form my model, I adopt a modular approach to first build pieces and then connect them together in the end. During chemotaxis, cells undergo large cellular morphology changes. Spatiotemporal signaling events alone are not enough to evaluate the correctness of model. Using a model of a deformable cell, we can simulate various experiments in silico. Thus, another focus of my research has been to develop a mathematical tool that can simulate large cell shape changes.

1.2 Mitosis

Mitosis is the process by which a cell, which has previously replicated its genetic materials, separates into two identical sets. The formation of the mitotic spindle is a key step before cell division representing one of nature's great examples of self-assembly [5]. It requires the concerted action of microtubules (MTs), mitotic motors, and associated proteins. A long-standing hypothesis has postulated that a static, non-MT structure might support the assembly of the mitotic spindle as well as supply a mechanical scaffold allowing the spindle to generate force [6]. Until recently, the existence, much less the nature and molecular identity, of this spindle matrix was uncertain. However, experiments have now provided support for both the existence of the matrix, as well as suggesting that it forms from several nuclear proteins. Tsai et al. showed that the intermediate filament protein lamin B assembles during mitosis into a matrix-like network in a RanGTP-dependent manner in Xenopus egg extracts [7].

Subsequent experiments have demonstrated that the matrix contains a number of spindle assembly factors, including dynein and Nudel [8].

How lamin B, a component of the nuclear lamina in interphase, and other intranuclear proteins assemble and localize around the spindle to form a mitotic matrix is unclear [9]. To answer these questions, I developed a computational model that describes the formation of the mitotic matrix and investigated the role that the resultant spindle matrix has on spindle morphology.

1.3 Organization of this dissertation

In Chapter 2, I review experimental characteristics and current mathematical models of chemotactic cells. My starting point is the LEGI-BEN (local excitation, global inhibition-biased excitable network) model. In Chapter 3, I explore an alternative to the LEGI scheme and several realizations of LEGI. In Chapter 4, I use the level set method to simulate changes of cell morphology driven by LEGI-BEN. Through these simulations, I show that, alone, the LEGI-BEN model exhibits no polarity. Thus, in Chapter 5, I introduce a polarity module to the LEGI-BEN. In Chapter 6, I develop a fast oscillatory network to account for recently reported observations regarding the nature of the cyteoskeletal network. Finally, in Chapter 7, I integrate the different modules to form a complete model that explains most experimental results. In Chapter 8, I introduce a mathematical model of mitotic spindle matrix formation. Finally, I summarize my work and point out future research directions in Chapter 9.

Chapter 2

Background: chemotaxis in vitro and in silico

Many cells use an internal "compass" that enables them to sense gradients of extracellular chemicals and to use this information to direct their migration. This ability, called chemotaxis [1], is similar in human leukocytes and free-living amoebae, suggesting that a unified mechanisms might be conserved among eukaryotic cells [4]. Thus, a mathematical framework may reveal the underlying mechanism of chemotaxis despite the seemingly diverse behavior of cells [10].

To motivate a comprehensive model of chemotaxis, we first need to understand various features of chemotactic cells. In this chapter, I review characteristics observed in chemotaxing cells and then briefly outline some mathematical efforts motivated by these observations. Finally, I introduce the *local excitation, global inhibition-*

biased excitable network (LEGI-BEN), a conceptual model proposed to explain the chemotactic response that will serve as the starting point of my work.

2.1 Characteristics of chemotactic cell

2.1.1 Chemotaxis involves three separate processes

Chemotaxis can be conceptually divided into three separable, but interconnected processes: motility, directional sensing, and polarity (Figure 2.1) [1].

Motility refers to the cell's ability to move around its environment [1]. In amoeboid cells, like *Dictyostelium discoideum* or mammalian neutrophils, motility is characterized by periodic extensions of actin-rich protrusions known as *pseudopods*. No chemotactic signaling is needed to generate pseudopods. For example, *Dictyostelium* cells migrate in the absence of chemotactic cues [11]. Moreover, pseudopods generated by these ramdomly migrating cells are similar to those generated in chemotaxing cells.

Gradient sensing refers to the cell's ability to recognize external chemical gradients and to guide internal proteins to the site with higher chemoattractant concentration [1]. In *Dictyostelium* and mammalian neutrophil cells, chemoattractants are interpreted by G-protein-coupled receptors and associated G proteins that are uniformly distributed along the cell perimeter but direct downstream signaling events toward or away from the higher side of the gradient [12]. For example, activation of Ras proteins and PI3-kinase, accumulation of phosphatidylinositol (3,4,5) trisphos-

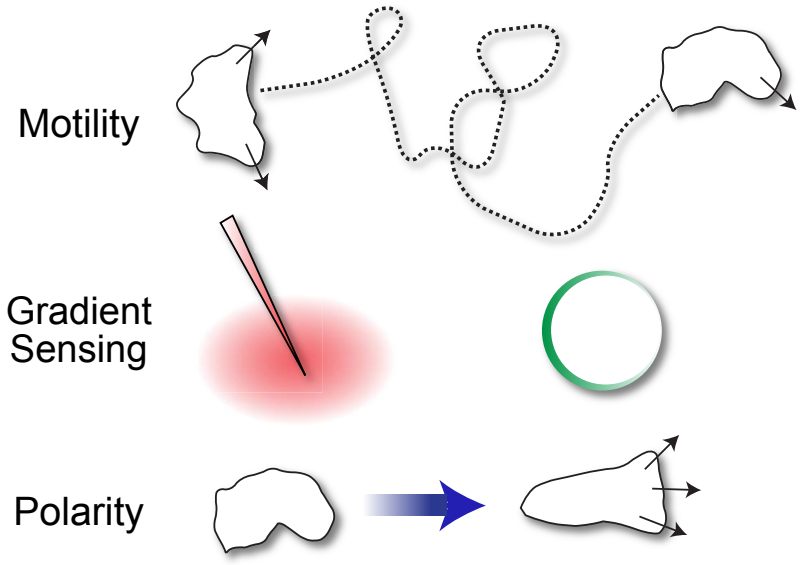

Figure 2.1: Chemotaxis is composed of motility, polarity, and directional sensing. Motility: amoeboid cells extend pseudopodia and move in random directions. Gradient Sensing: spatial sensing, a means of directional sensing, can be demonstrated by the gradient-mediated relocalization of proteins in cells immobilized by actin inhibitors. Polarity: chemotactic cells are often polarized, with a stable leading edge from which pseudopodia are extended. Figure adapted from [1].

phate (PIP3), and actin polymerization occur at the side with highest chemoattractant concentration, which we refer to as the *front* of the cell. In contrast, the PI3-phosphatase, PTEN, and myosin II localize at the side facing lower chemoattractant concentration, referred to as the rear [1]. Eukaryotic cells treated with Latrunculin, a drug that impairs the cell's motility by inhibiting actin polymerization, still show ability of gradient sensing, indicating that cells employ a spatial sensing mechanism that does not depend on movement [12, 13].

Polarity refers to the establishment and maintenance of distinct anterior and posterior regions, even in the absence of a gradient or in a uniform concentration of chemoattractant [14]. In *Dictyostelium*, polarity leads to elongated cell morphology. Polarity is not required for chemotaxis, but can enhances its efficiency as polarized cells usually move faster and with greater directional accuracy in a fixed gradient. The degree to which a cell is polarized can be observed in the behavior of cells that experience changes in the direction of the chemoattractant gradient [14]. Whereas unpolarized cells are equally sensitive along the perimeter and form a new front when exposed to a fresh gradient, polarized cells exposed to shallow gradients gradually turn while maintaining the same leading edge [15]. However, sufficiently steep gradients can work against the internal polarity and generate a new front from the rear of a polarized cell. In contrast to gradient sensing, polarization relies on intact cytoskeleton, which suggests polarity property may come from cytoskeletal network [13].

2.1.2 Key features

Because we seek to develop mathematical models that can succesfully recreate the chemotactic behavior of cells, it is useful to list some of the behaviors observed under various experimental conditions.

1. Pseudopodia that bring about random migration coincide with patches of elevated signaling as well as cytoskeletal activity [16–18].

2. Cytoskeletal and signaling activities propagate as waves which lead to the patches of activity seen on the pseudopodia [10, 19–23]. The propagating waves suggest that these networks are excitable.

3. New pseudopodia appear to split from previous ones [11, 15, 24]. Moreover, the observed pattern of pseudopod formation appears to "zig-zag" with newly formed pseudopods appearing in a left-right-left etc. pattern.

4. When exposed to spatially uniform chemotactic stimuli, cells "freeze" movement and then round up or "cringe", then spread projections in multiple directions, and finally resume normal migratory behavior [25].

5. During persistent stimulation cells eventually adapt to the current level of stimulation (Figure 2.2) but will respond again if the stimulus is increased or is reapplied after a period of recovery [16, 17, 26, 27].

6. Adaptation enables chemotactic cells to adjust their sensitivity and respond

only to the steepness but not the midpoint concentration of the gradient [13].

7. These events are driven by a stereotypical kinetically complex signaling response (i.e. Ras activation or PIP3 production) which is observed in immobilized as well as control cells. Within seconds of stimulus addition, cells produce an initial response around the whole perimeter that shuts off rapidly within 30 seconds and is followed by secondary patches lasting several minutes [18, 28, 29].

8. When cells are exposed to a gradient of chemoattractant, they produce directional responses and migrate directionally.

9. In immobilized cells, patches of response are stochastic but biased towards the high side of the gradient [30]. Cells are able to sense both steep and shallow external gradients (where the difference between front and back receptor concentration is as small as 1%-2%) within a vast range of concentrations. Polarization leads to an amplification of this asymmetry to some macroscopic level.

10. The directional response is amplified compared to the external gradient in the sense that it is confined to the anterior of the cell [13, 31].

11. Immobilized cells exposed to two gradients produce responses on both ends, while migrating polarized cells choose one or the other sources [13].

12. Cells can spontaneously become polarized - that is, they establish an axis of asymmetry in the absence of spatial cues and generate persistent random motion

[11, 32–36].

13. The intrinsic polarity of cells is regulated. In *Dictyostelium*, for example, developed cells are more polarized than young cells. Polarity can also be enhanced by a period of migration in a gradient [37].

14. Polarized cells will turn when the gradient is shifted rather than creating a new front [15, 37].

15. In many types of cells, polarity is maintained after the triggering stimulus is removed (maintenance). Some evidence suggests that this persistence requires an intact cytoskeleton.

2.1.3 Open questions

The above observations lead to a number of questions. For example:

1. How is adaptation achieved? Because numerous signaling events exhibit adaptation, can these be explained in a unified system?

2. How do cells amplify the steepness of the external gradient, so that the spatial distribution of intracellular markers is steeper than those of the external chemoattractant gradient?

3. How is polarization maintained after the external gradient is removed? Is the polarization mechanism the same scheme that cells use to achieve persistent migration in the absence of external gradients?

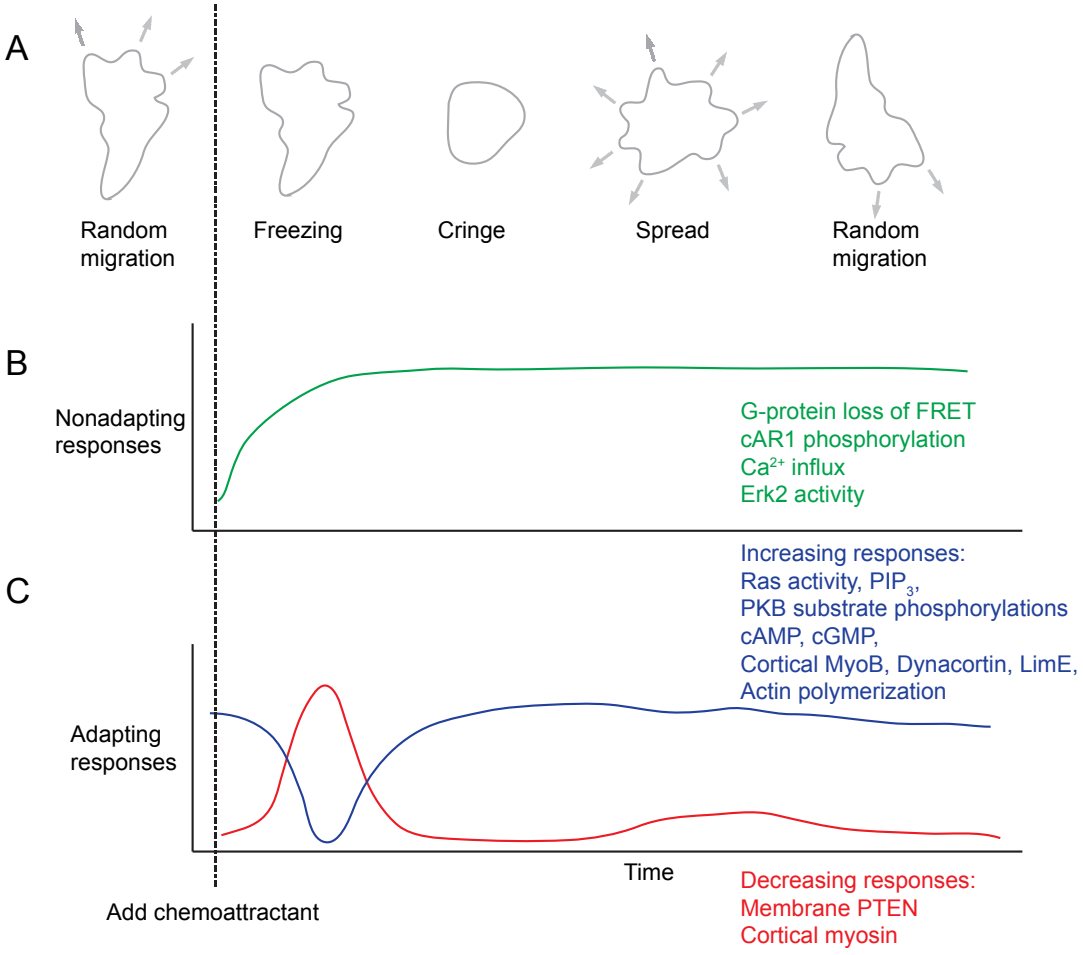

Figure 2.2: (A) Cell's morphological behavior during adaptation. (B) Nonadapting responses. (C) Adapting responses. Figure adapted from [1, 10].

4. How does the cytoskeleton enable cells to maintain their polarity?

5. What is the relationship between excitability with chemotaxis?

6. How do cells cope with stochastic fluctuations in the external signal?

7. How do cells resolve multiple conflicting stimuli to establish a single ultimate "front" of activity?

8. Motility, gradient sensing and polarity are interconnected but also seem to be separable. Do they reside in different modules?

These questions have motivated my research. In this dissertation, I will offer solutions.

2.2 A brief review of some relevant mathematical models

The study of chemotaxis has benefitted greatly from the interplay between experimental and theoretical studies. Although, to date, none of the proposed models can explain all the features pf chemotactic cells mentioned above, many work well to explain certain aspects. Here, I review several of the relevant models. This is not meant as an exhaustive review, but rather as an introduction of the models that will be used in this dissertation.

Models that explain the polarization mechanism, namely the cell's ability to transition from a spatially homogeneous state into an heterogeneous state with distinctive front and rear, has been a long-standing area of interest in the mathematical modeling community. One influential series of models originates from the concept of a

diffusion-induced instability, proposed by Alan Turing [38] and further refined by Hans Meinhardt and Alfred Gierer [39]. These models fall under two broad classes: activator-inhibitor systems, and substrate-depletion schemes [40,41]. Models describing the establishment of polarity have been reviewed thoroughly in [42, 43].

The ability to sense gradients has also received considerable attention, though a general consensus has arisen suggesting that cells employ some form of local-excitation, global-inhibition mechanism (LEGI) scheme [12, 44]. As shown below, the LEGI mechanism explains adaptation and gradient sensing. A variation of the LEGI mechanism is the *balanced inactivation model* [45] which adds an additional slow activator to LEGI. This change generates a switch-like behavior responding to gradient.

Cell motility arises from the cooperation of protrusion from actin polymerization, contraction of cytoplasm and adhesion. As such, much of the theoretical work in this field focuses on the dynamics of actin polimerization. For a thorough review, see [46]. Recently, there has been a lot of attention on reports of traveling waves in the actin network [19, 21, 47, 48]. It has been suggested that this wave propagation is the result of an underlying excitable network [10]. The implications of this excitable behavior hypothesis are reviewed in [49, 50].

2.3 Local-excitation, global-inhibition-biased excitable network

Xiong et al. proposed combining the LEGI mechanism with an excitable network (EN) to explain the spatio-temporal signaling activities in chemotaxis cells [10]. Here I provide a mathematical description of this mechanism.

2.3.1 Local-excitation, global-inhibition

The LEGI mechanism was proposed to explain two important chemotactic behaviors: adaptation and gradient sensing [12, 44, 51]. In the LEGI model, a signal (S) activates a fast, local excitation (E) and a slow, global inhibition (I). The balance between excitation and inhibition control the production of a response regulator (R) that further controls downstream activity (Figure 2.3A). There are numerous ways of implementing the LEGI mechanism [52]. One specific mathematical representation is shown below:

$$\frac{\partial E}{\partial t} = -k_{-E}E + k_E S \tag{2.1}$$

$$\frac{\partial I}{\partial t} = -k_{-I}I + k_I S + D_I \nabla^2 I \tag{2.2}$$

$$\frac{\partial R}{\partial t} = -k_{-R}IR + k_R(R_T - R)E. \tag{2.3}$$

Qualitatively, the LEGI mechanism accounts for the response observed of various biosensors that: 1) are seen to translocate to or be activated transiently on the cell cortex during uniform stimulation; and 2) move to or be activated at the front (e.g.

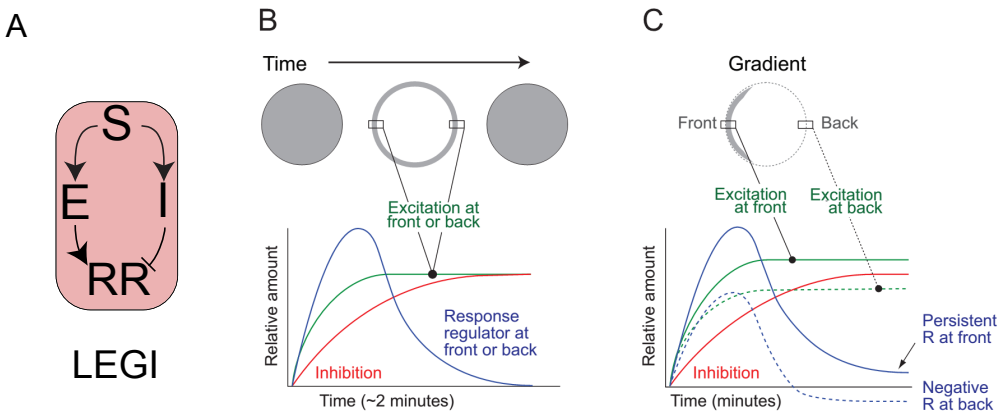

Figure 2.3: LEGI scheme and mechanism. (A) In LEGI, both excitation (E) and inhibition (I) are driven by an external stimulus (S). The excitation process activates the production of the response regulator, RR. In contrast, the I inhibits RR. (B) The excitation reflects the local receptor occupancy, whereas the inhibition depends more closely on the average level of receptor occupancy. When a uniform stimulus is applied to cell, the excitation grows faster than inhibition; the response regulator rises transiently until the slower inhibitor catches up. The cells adapt perfectly at the front and back. (C) When a gradient is applied, there is an initial response. However, when it reaches a steady state, the excitation exceeds the inhibition at the front of the cell while it is lower at the back. This difference leads to a response regulator that, relative to basal levels, is persistently higher at the front and lower at the back. Figure reprinted with permission from [10]. Copyright 2010 National Academy of Sciences USA.

Ras, PI3K, PH domains, actin binding proteins) or rear (e.g. PTEN, myosin) in a gradient.

Biologically, excitation reflects the level of local receptor occupancy, whereas inhibition depends on the average level of receptor occupancy. When a uniform stimulus is applied to a cell (Figure 2.3B), both excitation and inhibition are activated and rise to same level proportional to the external stimulus. However activation rises faster than inhibition, thus the response regulator is activated until the inhibition reaches to the same level as activation. This process ensures a perfect adaptation.

The timescale of the inhibition and response regulator are on the order two minutes. When a gradient is applied to cells (Figure 2.3C), both activation and inhibition are also activated. However, when the system reaches a steady state, the excitation exceeds the inhibition at the front of the cell while it is lower at the back. This difference leads to a response regulator that, relative to basal levels, is persistently higher at the front and lower at the back. This gives a persistent response at the front of cell facing gradient [51].

2.3.2 Excitable network

Excitability is a systematic behavior in which sub-threshold perturbations are attenuated, but those above a threshold elicit a large burst of activity before eventually returning to basal level. These systems exhibit a recovery time known as the *refractory period* during which the system cannot be further stimulated. Excitability can also lead to traveling waves in media. In biology, a form of an excitable system was proposed to account for the "all-or-nothing" behavior of action potentials in neurons by Hogkin and Huxley [53]. FitzHugh and Nagumo simplified the mathematical model that recreated the dynamics of excitability [54, 55]. The FitzHugh-Nagumo model is special case of the activator-inhibitor systems, in which one component acts as an activator, as it holds an autocatalytic loop and activates the downstream component, the inhibitor, which provides negative feedback to the activator.

Motivated by the FitzHugh-Nagumo model, Xiong et al. proposed an excitable network to account for the observed behaviors in signaling and cytoskeletal activity

in chemotactic cells [10]. This network is described by a reaction-diffusion network, consisting of the partial differential equations:

$$\frac{\partial X}{\partial t} = \alpha \frac{X^2}{k^2 + X^2} - \beta X - \gamma Y + \rho U + D_X \nabla^2 X \tag{2.4}$$

$$\frac{\partial Y}{\partial t} = \delta X - \epsilon Y + D_Y \nabla^2 Y. \tag{2.5}$$

This system is a special case of an activator-inhibitor scheme. Component X acts as the activator: it is autocatalytic, and also activates the downstream component, which was referred to as the feedforward loop. The Y component provides negative feedback to X (Figure 2.4A). Figure 2.4B shows the time course of one excitable firing. X and Y are initially at equilibrium (point a). Noise, or a change in the response regulator of the LEGI mechanism, alters the amount of X. If a small increase in X reaches a "threshold," then positive feedback causes X to increase greatly (from a to b), forcing a delayed increase in Y which begins the shutoff of X (from b to c). This continues until X reaches its minimum (d) and then the system settles to its new equilibrium (e). The timescale for this response is relatively fast, lasting approximately ten seconds.

In a phase-plane diagram (Figure 2.4C), the system equilibrium is the point where the two nullclines meet (i.e., indicating zero rate of change of X and Y; initially at point a). The increase in X raises the X-nullcline which shifts the equilibrium to a new point (e). As the system is no longer in equilibrium, X and Y must change. Owing to the positive feedback, X changes greatly and Y changes slightly, causing the system to move away from the new equilibrium toward point b. The high level of

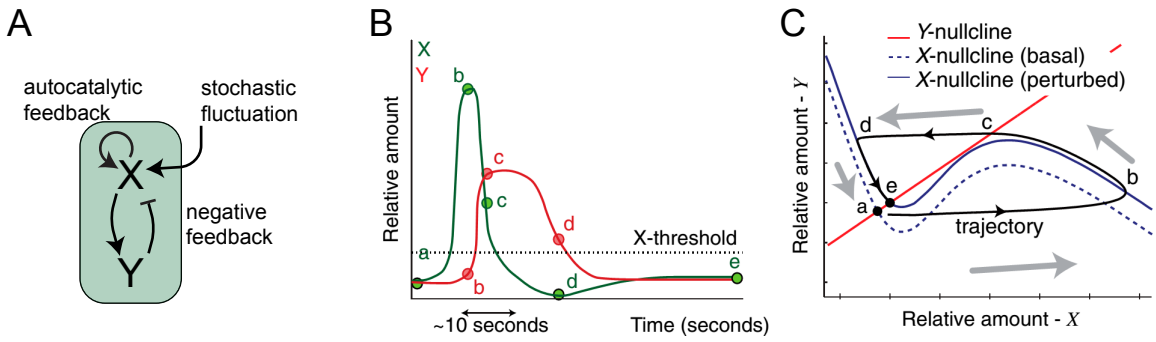

Figure 2.4: Excitable network based on an activator-inhibitor scheme. (A) The activator,X, is autocatalytic and also activates the inhibitor, Y, which in turn, provides negative feedback enabling a shutoff of the network. The systems can be triggered by stochastic perturbations, or by external signals. (B) Sample time course of X and Y in the excitable network. It shows the process of one firing. (C) Phase-plane trajectory of this firing. The line labeled "trajectory" plots changes in both values at the same time. The phase-plane diagram also shows "nullclines", determined by setting the expressions for the rates of change of X and Y equal to zero, which helps predict the response of the system to perturbation. Vector arrows indicate the direction a trajectory must take. Figure reprinted with permission from [10]. Copyright 2010 National Academy of Sciences USA.

X leads to an increase in Y which counteracts X. At point b, X reaches its maximum as it crosses the new X nullcline. As Y continues to increase to point c, the decrease of X continues until the trajectory again crosses the X nullcline at point d. From there, the system settles to its new equilibrium (e).

In the EN, both components diffuse spatially, with different diffusion coefficients. This diffusion allows the activity of both species to propagate outward from the spot of the initial firing. However, if the diffusion of the Y component is faster, this species will eventually pass the activator, causing further propagation to cease.

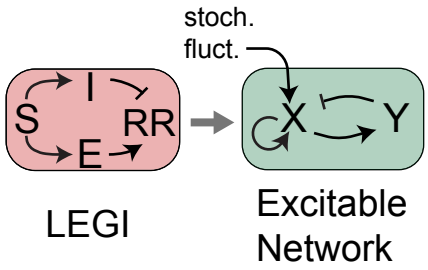

Figure 2.5: The structure of the LEGI-biased excitable network. It consists of a LEGI module, in which the external signal, S, drives excitation, E, and inhibition, I, which in turn control a response regulator, RR. The RR is a positive driver of an excitable network. The excitable network is represented, for simplicity, by interactions between variables X and Y and can be also triggered by stochastic noise.

2.3.3 Properties of the combined LEGI-BEN model

Alone, neither the LEGI nor the EN mechanisms account for all the observed behaviors of chemotactic cells. However, as we illustrate below through simulation, when the two mechanisms were combined, the resultant LEGI-BEN model captured many of these behaviors (Figure 2.5, [10]). To facilitate tracking of the temporal and spatial responses of the model, simulations were carried out on a circular domain and the activity of the simulated cell was represented as a kymograph of Y (Figure 2.6). Kymograph is made by stacking vertical lines stretched from cell perimeter. The patches (Figure 2.6) represent activities at cell cortex. The X-axis of kymograph is time and Y-axis is location on cell perimeter represented by angle.

1. Without stimulus, localized patches of activity appear randomly. As seen in the kymograph of a cell in the absence of stimulation, patches of activity can appear simultaneously, either far from each other (Figure 2.6) or sufficiently

close to give the appearance of a single, wider crescent. The patches spread out laterally and in some cases, a smaller secondary increase emerged at the edge of a patch.

2. A spatially uniform stimulus gave rise to a burst of activity that covered nearly the entire perimeter (Figure 2.7). This response declined rapidly by 30 seconds due to the negative feedback loop within the excitable network. A second phase of high activity then appeared, though it was not as consistent in space as the initial response. The frequency of patches remained higher than prestimulus levels for a few minutes, corresponding to the timescale of the LEGI module. Eventually, the system adapted and the spontaneous activity returned completely to the prestimulus level as the response regulator disappeared.

3. The application of a chemoattractant gradient caused a series of localized patches appeared with temporal regularity, primarily aligned with the external gradient (Figure 2.8).

2.4 Simulating cell shape changes during chemotaxis

The models described above aim to reproduce localized patterns of activity in cells, or the translocation of biochemical species in response to chemoattractant stimuli. However, to test the model's effectiveness in recreating chemotaxis, we must have a way of testing a model's ability to propel a cell. Here I review a framework based on level set methods (LSM) that incorporates a viscoelastic model of *Dictyostelium*

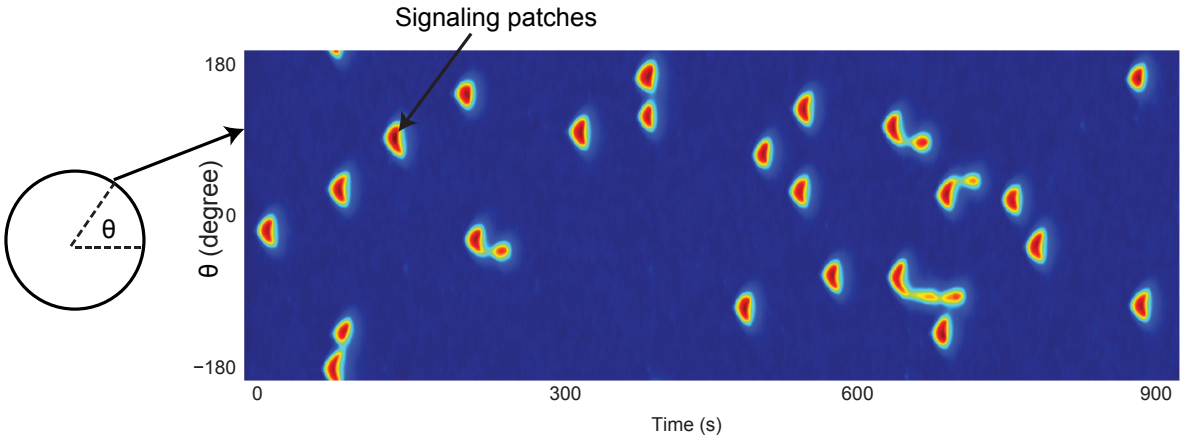

Figure 2.6: Spontaneous activities without stimulus. Random patches can be seen around the cell perimeter.

cells based on mechanical perturbations obtained using micropipette aspiration, that was developed to simulate large cellular deformations such as those observed during chemotaxis [56].

2.4.1 Level set formulism

In the level set method, the cell shape is defined implicitly using a potential function (Figure 2.9A) [57, 58]. The cell shape is deformed by evolving this potential function. This implicit representation of cell shape gives the level set method advantages in model simplicity and computational expense over other traditional methods.

In short, in the level set method (LSM), the cell is described as the zero-level set of a potential function $\varphi(x,t)$, $x \in \mathbf{R}^2$. We use a signed distance function as the

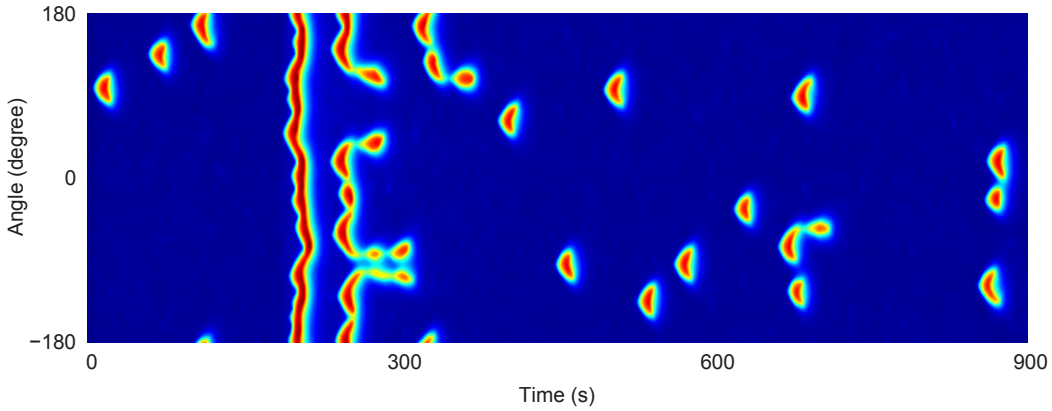

Figure 2.7: Simulation with addition of uniform stimuli. Response of model to addition of uniform stimuli denoted by the bar above the kymograph.

potential function, defined by:

$$\varphi(x,\Gamma) = \begin{cases} -d(x,\Gamma), & \text{if } x \text{ is inside the cell,} \\ d(x,\Gamma), & \text{if } x \text{ is outside the cell,} \\ 0, & \text{otherwise.} \end{cases} \tag{2.6}$$

Here, $d(x,\Gamma)$ is the distance of position x to the cell boundary (initially a sphere of radius 5.1 μm). The evolution of the potential function is described by the Hamilton-Jacobi equation:

$$\frac{\partial\varphi(x,t)}{\partial t} + v(x,t)|\nabla\varphi(x,t)| = 0, \tag{2.7}$$

where $v(x,t)$ describes the local speed in normal direction of the potential function (Figure 2.9B).

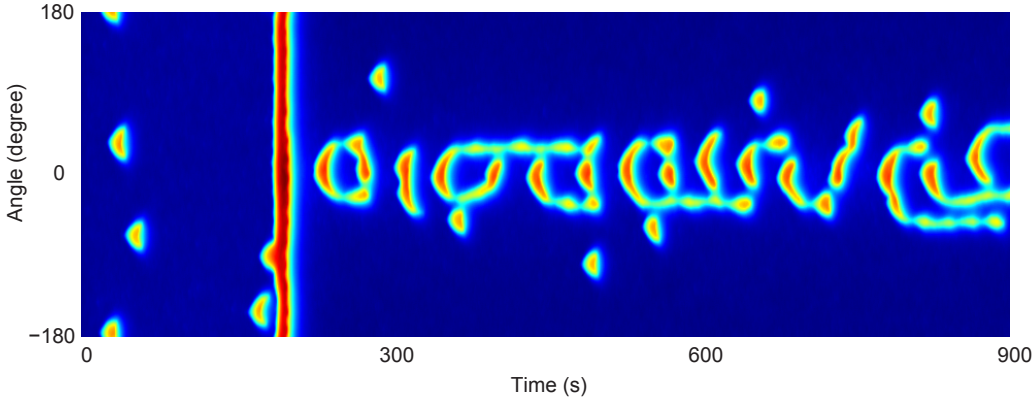

Figure 2.8: Response of the model to applied spatial gradients. A steep spatially graded stimulus was applied at 180 s.

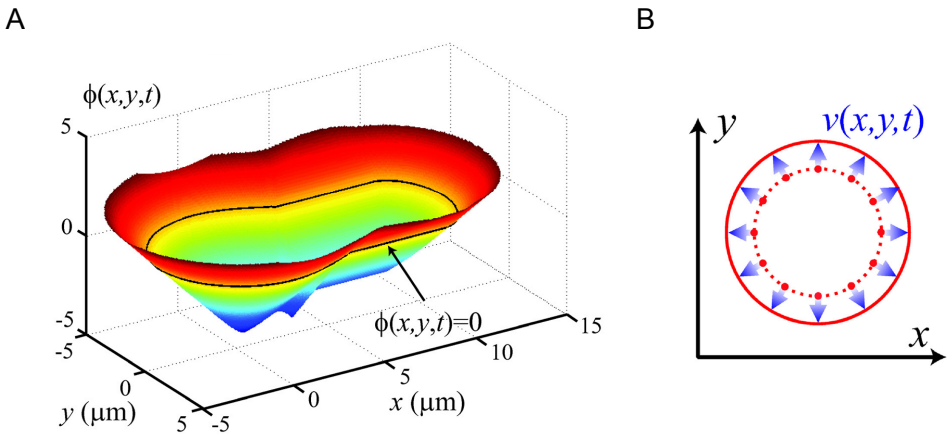

Figure 2.9: The level set formulism. (A) The implicit representation of cell boundary by connecting the points with zero level of potential function $\varphi(x,t)$. (B) The local velocity to evolve the cell boundary. Figure reprinted with permission from [56]. Copyright 2008 BioMed Central Ltd.

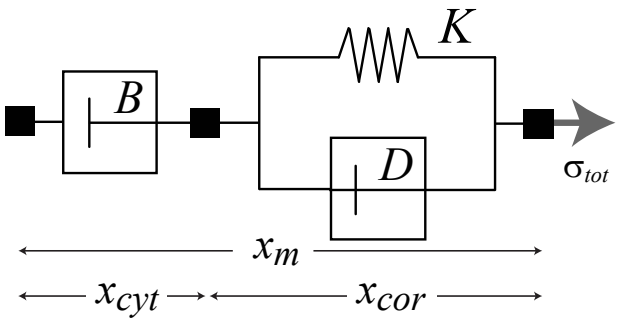

Figure 2.10: Viscoelastic model of cell. Cell boundary/membrane displacements (x_m) are generated by moving the potential function according to the total stress applied, σ_{tot} (2.8). The spring-dashpot (K, D) elements represent the mostly elastic cortex, which moves a distance x_{cor} (2.9). The viscous component (B) represents the cytosol, which moves a distance x_{cyt}. Figure reprinted with permission from Ref [59]. Copyright 2012 CC-BY.

2.4.2 Viscoelastic cell mechanical model

To obtain the speed, $v(x,t)$, we apply different stresses to the cell and use a viscoelastic mechanical model (Figure 2.10) of the cell to determine the local velocity.

The mechanical description of the cell was previously identified based on micropipette aspiration experiments using *Dictyostelium* cells [56]. It incorporates several passive stresses, including the effect of cortical tension driving Laplace-like pressures on the cell, and volume conservation. It also includes active stresses allowing us to test the effectiveness of the EN in driving cellular motion. In our simulations, the activity of the EN was coupled to protrusive forces, so that higher activity at one location gave stronger protrusive stress.

Table 2.1: Viscoelastic mechanical parameters

Parameter	Value	Units	Parameter	Value	Units
K	0.098	$\mathrm{nN}\,\mu\mathrm{m}^{-3}$	D	0.064	$\mathrm{nN}\,\mu\mathrm{m}^{-3}$
B	6.09	$\mathrm{nN\,s}\,\mu\mathrm{m}^{-3}$	γ	1.00	$\mathrm{nN}\,\mu\mathrm{m}$
σ_0	35	$\mathrm{nN\,s}\,\mu\mathrm{m}^{-3}$	k_{area}	1	$\mathrm{nN}\,\mu\mathrm{m}^{-2}$

Mathematically, the viscoelastic model is described by:

$$\dot{x}_m = -(K/D)x_{cor} + (1/D + 1/B)\sigma_{tot} \tag{2.8}$$

$$\dot{x}_{cor} = -(K/D)x_{cor} + (1/D)\sigma_{tot} \tag{2.9}$$

where σ_{tot} is the total stress applied on the cell, x_m and x_{cor} are the local displacements of the boundary and cortex, respectively, and K, D and B are viscoelastic components of the cell describing the elasticity (K) and viscosity D) of the membrane, and the viscosity (B) of the cytoplasm. The speed is given by:

$$v(x,t) = \frac{dx_m}{dt} \tag{2.10}$$

The parameters of viscoelastic model were obtained using by fitting experimental measurements of aspirated *Dictyostelium* cells using a micropipette, as previously reported [56, 59]. The parameters are shown in Table 2.1:

2.5 Summary

In this chapter, I reviewed the three main processes of chemotaxis: motility, directional sensing, polarity and characteristic behaviors of chemotactic cells. Motivated

by these observations, numerous models attempting to explain these features have been proposed. However, none of these models accounts for all the observed features.

I subsequently reviewed the LEGI-BEN model that will serve as the starting point of my research. The LEGI-BEN mechanism captures important experimental observations. In the absence of stimulation, the excitable network generates spontaneous spots of activity. Chemoattractant stimulus triggers an initial burst of patches followed by localized secondary events. After a few minutes, the system adapts, again displaying random activity. In gradients, the activity patches are directed continuously and selectively toward the chemoattractant, providing an extraordinary degree of amplification. The LEGI-BEN hypothesis incorporates many of the features and surmounts many of the difficulties posed by other schemes proposed to explain chemotaxis, although there are still some open questions. Finally, I discussed the level set method with which I will simulate cell shape changes driven by the LEGI-BEN mechanism.

Chapter 3

Gradient Sensing

Chapter 2 reviewed a gradient sensing module—the local-excitation, global-inhibition (LEGI)—that ensures that cells adapt in response to external spatially homogeneous stimuli, but also respond persistently in the presence of a gradient [12, 44, 51]. The implementation of the LEGI is based on an incoherent feedforward (IFF) scheme, in which parallel signals from the stimulus regulate a response regulator in complementary ways (excitation and inhibition). The IFF topology is one of two means for achieving perfectly adapting responses [60]. A second scheme, involving a *negative feedback* (NFB) loop can also realize perfect adaptation [61–63]. The role of the NFB scheme in gradient sensing, however, has not been previously investigated. In this chapter, I show that the NFB topology, coupled to local excitation and global inhibition, can also recreate the two features of the IFF-LEGI: adapation and static spatial sensing.

3.1 A LEGI module involving negative feedback

The system being considered consists of two components: a local excitation (E) and a global negative feedback inhibitor (I) as illustrated in Figure 3.1A. The stimulus (S) activates the excitation process, which subsequently activates the inhibitor. The latter provides inhibition to the excitation (the negative feedback loop) to bring back E to prestimulus levels. As in the IFF-LEGI, the excitation is assumed to be local (so that it does not diffuse) and inhibition global, with diffusion rate $D \gg 0$. Under spatially uniform stimulation, this diffusion does not play any role, but it is key in gradient sensing.

A mathematical representation of our system is:

$$\frac{\partial E}{\partial t} = -k_{-e}EI + k_e S \tag{3.1}$$

$$\frac{\partial I}{\partial t} = -\frac{k_{-i}I}{\epsilon + I} + k_i E + D\nabla^2 I. \tag{3.2}$$

Note that we assume that the degradation of the inhibitor follows a Michaelis-Menten form: $\frac{k_{-i}I}{\epsilon+I}$. The parameter ϵ is the Michaelis-Menten coefficient. Typically, if adaptation is to be achieved, this coefficient is assumed to be small relative to the concentration of I, so that the enzyme is working at saturation.

3.1.1 Adaptation

Before demonstrating the gradient sensing capabilities of the system, we show that the system can achieve perfect adaptation. In this case we consider the situation when a spatially uniform stimulus is applied. Because of the spatial homegeneity, the

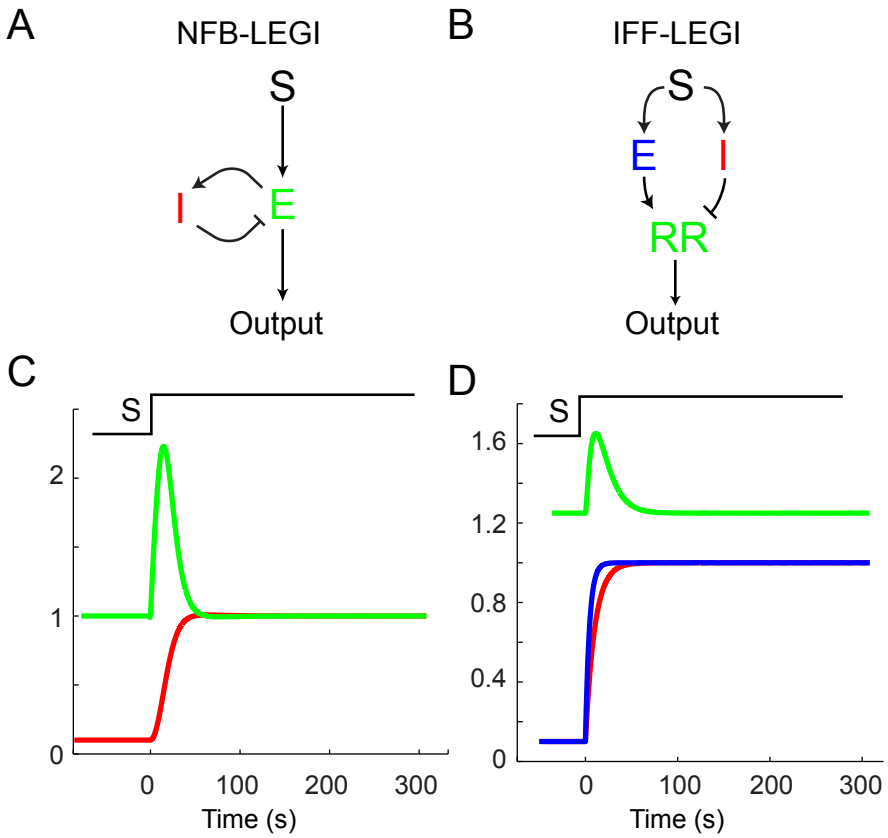

Figure 3.1: Negative feedback network achieves perfect adaptation. (A) The negative feedback scheme. (B) The LEGI scheme. (C) In NFB model, E (blue) adapts perfectly after uniform stimulus while I's (red) steady state is proportional to input stimulus S (black). (D) In LEGI, both E (blue) and I (red) have same steady state proportional to input stimulus S (black). The response regulator (RR) (green) adapts under uniform stimulus.

diffusion term can be disregarded. Assuming a constant stimulus $S = S_0$, we compute the steady state of E_0 and I_0. By setting the derivatives of E and I to zero, we have:

$$-k_{-e}E_0I_0 + k_eS_0 = 0$$
$$-\frac{k_{-i}I_0}{\epsilon + I_0} + k_iE_0 = 0.$$

This simplifies to:

$$E_0 = \frac{k_e}{k_{-e}}\frac{S_0}{I_0} \tag{3.3}$$
$$\frac{k_i}{k_{-i}}E_0 = \frac{I_0}{I_0 + \epsilon}. \tag{3.4}$$

Substituting E_0 from Equation 3.3 into Equation 3.4 and defining the notation: $\alpha = k_e/k_{-e}$ and $\beta = k_i/k_{-i}$, we obtain an equation for I_0:

$$I_0^2 - \alpha\beta S_0 I_0 - \alpha\beta\epsilon S_0 = 0.$$

Solving this equation and discarding the negative solution, we obtain the steady-state levels of the inhibition:

$$I_0 = \frac{\alpha\beta S_0 + \sqrt{\alpha^2\beta^2 S_0^2 + 4\alpha\beta\epsilon S_0}}{2},$$

and excitation:

$$E_0 = \frac{2\alpha S_0}{\alpha\beta S_0 + \sqrt{\alpha^2\beta^2 S_0^2 + 4\alpha\beta\epsilon S_0}}.$$

To achieve perfect adaptation, the steady state of E_0 needs to be independent of the input stimulus S_0. We do further transformation of the steady-state value of E_0:

$$E_0 = \frac{2\alpha}{\alpha\beta + \sqrt{\alpha^2\beta^2 + 4\alpha\beta\epsilon/S_0}}.$$

Thus, we want $\alpha\beta\epsilon \approx 0$. Setting $\alpha = 0$ implies that $k_e = 0$ which means that the stimulus does not reach the system. If $\beta = 0$, then the inhibitor signal is zero, which means that the equation for E is unstable (as it merely integrates S) and hence there is no equilbrium. Thus, the only means for achieving a perfectly adapting equilbrium is for $\epsilon = 0$. In this limit, we have:

$$\lim_{\epsilon \to 0} E_0 = \frac{1}{\beta} \quad \text{and} \qquad \lim_{\epsilon \to 0} I_0 = \alpha\beta S_0.$$

Thus, perfect adaptation is achieved in this case. Note that perfect adaptation comes from the fact that the negative feedback term is providing integral control, since

$$\frac{dI}{dt} \approx -k_{-i} + k_i E = -k_i \left(\frac{k_{-i}}{k_i} - E(t) \right)$$

implies that

$$I(t) = -k_i \int_0^t E_0 - E(t)\, dt.$$

In this case, the present value of $E(t)$ is compared to the steady-state value (E_0) and the difference integrated. This integral control motif is a special case of a more general theory of control engineering, referred to as the internal model principle [64].

Note that if all we seek is for approximate perfect adaptation [65], then we do not need $\epsilon = 0$ but rather that $I \gg \epsilon$, in which case the Michaelis-Menten term that describes the degradation term for the inhibitor is acting at saturation.

3.1.2 Gradient sensing

We now consider the NFB-LEGI scheme under a spatially varying stimulus. To simplify the analysis we assume that $\epsilon = 0$ and a one-dimensional spatial domain

with periodic boundary conditions. We denote the spatial variable by θ. In this case, the partial-differential equations are given by:

$$\frac{\partial E}{\partial t} = k_e S(\theta) - k_{-e} E(\theta) I(\theta)$$
$$\frac{\partial I}{\partial t} = -k_{-i} + k_i E(\theta) + D\frac{\partial^2 I}{\partial \theta^2}.$$

We can simplify the analysis if we redefine some terms. Let $\hat{E} = k_{-e} k_i E$, in which case

$$\frac{\partial \hat{E}}{\partial t} = k_e k_{-e} k_i S(\theta) - k_{-e} \hat{E}(\theta) I(\theta)$$
$$\frac{\partial I}{\partial t} = -k_{-i} + \frac{1}{k_{-e}} \hat{E}(\theta) + D\frac{\partial^2 I}{\partial \theta^2}.$$

We now define $\hat{I} = k_{-e} I$, in which case the system is:

$$\frac{\partial \hat{E}}{\partial t} = k_e k_{-e} k_i S(\theta) - \hat{E}(\theta)\hat{I}(\theta)$$
$$\frac{\partial \hat{I}}{\partial t} = -k_{-i} k_{-e} + \hat{E}(\theta) + D\frac{\partial^2 \hat{I}}{\partial \theta^2}.$$

Define a scaled external stimulus: $\hat{S} = k_e k_{-e} k_i S$ and constant $k = k_{-i} k_{-e}$. These changes lead to:

$$\frac{\partial \hat{E}}{\partial t} = \hat{S}(\theta) - \hat{E}(\theta)\hat{I}(\theta) \tag{3.5}$$
$$\frac{\partial \hat{I}}{\partial t} = -k + \hat{E}(\theta) + D\frac{\partial^2 \hat{I}}{\partial \theta^2}. \tag{3.6}$$

Note that the system now has only one free parameter, k. For the rest of the analysis we use this formulation of the system and drop the "$\hat{}$" notation.

Suppose that the external gradient satisfies a simple sinusoidal relationship [66]:

$$S(\theta) = s_0 + s_1 \cos\theta, \qquad -\pi \leq \theta \leq \pi,$$

where $s_0 > s_1 > 0$ to ensure that the concentration is positive everywhere. Now, assume that the steady-state concentrations of E and I are given by:

$$E(\theta) = e_0 + \sum_{n\geq 1} e_n \cos(n\theta) + \hat{e}_n \sin(n\theta)$$

and

$$I(\theta) = i_0 + \sum_{n\geq 1} i_n \cos(n\theta) + \hat{i}_n \sin(n\theta),$$

respectively.

At steady-state, Equation 3.6 simplifies to

$$k = \left(e_0 + \sum_{n\geq 1} e_n \cos(n\theta) + \hat{e}_n \sin(n\theta)\right) - D\left(\sum_{n\geq 1} n^2 i_n \cos(n\theta) + \hat{i}_n \sin(n\theta)\right).$$

Because the cosine and sine terms are orthogonal, if follows that $e_0 = k$, $e_n = Dn^2 i_n$, and $\hat{e}_n = Dn^2\hat{i}_n$ for $n \geq 1$. Note that this means that the coefficients of i_n and $\hat{i}_n$ must decay at least n^2 times faster than those of e_n and $\hat{e}_n$ and also means the diffusion D determines the gradient sensing efficiency.

We can now solve for these coefficients using Equation (3.5), evaluated at steady state. In particular,

$$\begin{aligned} s_0 + s_1\cos\theta &= \left(e_0 + \sum_{n\geq 1} e_n \cos(n\theta) + \hat{e}_n \sin(n\theta)\right)\left(i_0 + \sum_{n\geq 1} i_n \cos(n\theta) + \hat{i}_n \sin(n\theta)\right) \\ &= \left(k + D\sum_{n\geq 1} n^2[i_n \cos(n\theta) + \hat{i}_n \sin(n\theta)]\right)\left(i_0 + \sum_{n\geq 1} i_n \cos(n\theta) + \hat{i}_n \sin(n\theta)\right). \end{aligned}$$

In general, solution of this equation is impractical. However, we take advantage of the fact that the terms are decreasing rapidly and write down the first few terms.

Dropping terms higher than first order, we have:

$$\begin{aligned} s_0 + s_1\cos\theta &\approx \Big(e_0 + e_1\cos\theta + \hat{e}_1\sin\theta\Big)\Big(i_0 + i_1\cos\theta + \hat{i}_1\sin\theta\Big) \\ &= e_0 i_0 + [e_0 i_1 + e_1 i_0]\cos\theta + [e_0\hat{i}_1 + \hat{e}_1 i_0]\sin\theta \\ &\quad + [e_1\hat{i}_1 + \hat{e}_1 i_i]\cos\theta\sin\theta + e_1 i_1\cos^2\theta + \hat{e}_1\hat{i}_1\sin^2\theta. \end{aligned}$$

Substituting the identities

$$\cos^2\theta = \tfrac{1}{2}\left(1 + \cos 2\theta\right)$$

$$\sin^2\theta = \tfrac{1}{2}\left(1 - \cos 2\theta\right)$$

$$\sin\theta\cos\theta = \tfrac{1}{2}\sin 2\theta,$$

and dropping the higher order terms leads to the following:

$$\begin{aligned} s_0 + s_1\cos\theta &\approx e_0 i_0 + \tfrac{1}{2}[e_1 i_1 + \hat{e}_1\hat{i}_1] + [e_0 i_1 + e_1 i_0]\cos\theta + [e_0\hat{i}_1 + \hat{e}_1 i_0]\sin\theta \\ &= k i_0 + \tfrac{D}{2}[i_1^2 + \hat{i}_1^2] + [k i_1 + D i_0 i_1]\cos\theta + [k\hat{i}_1 + D i_0\hat{i}_1]\sin\theta. \end{aligned}$$

From orthogonality of the sinusoidal terms, we have three (nonlinear) equations in three unknowns:

$$s_0 = k i_0 + \tfrac{D}{2}[i_1^2 + \hat{i}_1^2] \tag{3.7}$$

$$s_1 = k i_1 + D i_0 i_1 \tag{3.8}$$

$$0 = k\hat{i}_1 + D i_0\hat{i}_1. \tag{3.9}$$

Note that the last equation can be rewritten as

$$\left(k + D i_0\right)\hat{i}_1 = 0$$

from which it follows that either $k + Di_0 = 0$ or $\hat{i}_1 = 0$. If the former is true then, by Equation 3.8,

$$s_1 = (k + Di_0)\, i_1$$

is impossible. Thus, $\hat{i}_1 = 0$ and we are left with two equations:

$$s_0 = ki_0 + \tfrac{D}{2} i_1^2$$

$$s_1 = ki_1 + Di_0 i_1.$$

Replacing i_0 from the first equation into the second, leads to a third order equation for i_1:

$$s_1 = ki_1 + \frac{D}{k}\Big(s_0 - \tfrac{D}{2} i_1^2\Big) i_1.$$

Equivalently,

$$\frac{D^2}{2k} i_1^3 + \left(k - \frac{DS_0}{k}\right) i_1 - s_1 = 0. \tag{3.10}$$

Equation 3.10 is a cubic equation. Its discriminant is:

$$\Delta = -4\frac{D^2}{2k}\left(k - \frac{DS_0}{k}\right)^3 - 27 s_1^2 \frac{D^4}{4k^2}$$

When Δ is less than zero, which is equivalent to:

$$4\frac{D^2}{2k}\left(k - \frac{DS_0}{k}\right)^3 + 27 s_1^2 \frac{D^4}{4k^2} > 0 \tag{3.11}$$

there is only one real solution for Equation 3.10. We consider the function:

$$f(x) = \frac{D^2}{2k} x^3 + \left(k - \frac{DS_0}{k}\right) x - s_1$$

Table 3.1: NFB-LEGI model parameters

Parameter	Value	Units	Parameter	Value	Units
k_E	0.15	s^{-1}	k_{-E}	0.15	s^{-1}
k_I	0.03	s^{-1}	k_{-I}	0.03	s^{-1}
D_I	100	$\mu m^2\, s^{-1}$			

that when $x = 0$, $f(x) = -s_1 < 0$ and when $x \to +\infty$, $f(x) \to +\infty$. Thus, we know there is a positive value of x that makes $f(x) = 0$. Since Equation 3.10 has only one real solution, then we know the solution i_1 for Equation 3.10 must be strictly greater than zero. Moreover, $e_i = Di_1 > 0$, implying that species E follows the gradient.

3.1.3 Simulation results

We now carry out simulations using the NFB-LEGI and compare its performance with that of the IFF-LEGI, reviewed in Chapter 3. The parameters used to simulate the NFB-LEGI are given in Table 3.1:

We first tested the system's response under uniform stimulus. Both the NFB and IFF achieve perfect adaptation; see Figure 3.1C, D. Both responses from the systems adapt in approximately one minute.

We next tested this model's response to a spatial chemoattractant gradient. The front and back responses under gradient are shown in Figure 3.2. In the NFB-LEGI, both E and I form gradients in the direction of the external gradient, as expected from the analysis above.

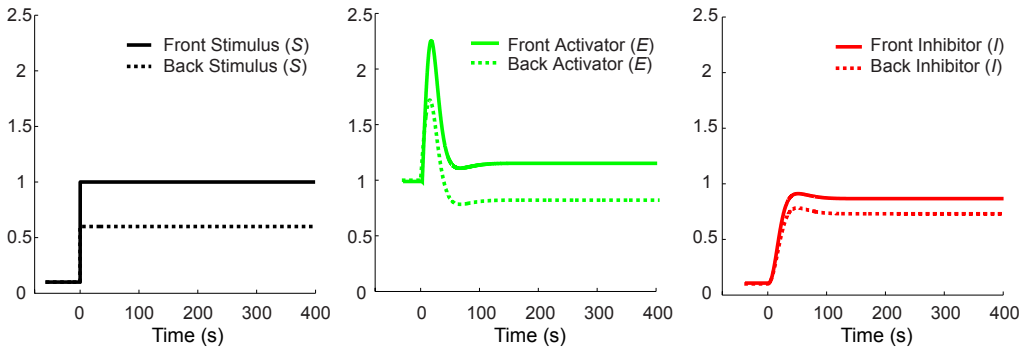

Figure 3.2: Negative feedback network realizes gradient sensing. Under a gradient, the cell front senses higher stimulus level than the back. Correspondingly, the signal E at the front is higher than at the back, while I shows a smaller difference between front and back.

To test the effect of the diffusion coefficient on the ability to sense the gradient, we set a gradient $s = 1 + 0.3\cos\theta$ to both the NFB-LEGI and IFF-LEGI. The responses are shown in Figure 3.3. By measuring the signals at the front and back, we compued the ratio of the signals; for example,

$$G_{\text{out}} = \frac{RR(0)}{RR(\pi)} \qquad \text{and} \qquad G_{\text{in}} = \frac{S(0)}{S(\pi)}$$

for the IFF-LEGI model, and defined the gradient sensing strength according to $G_{\text{out}}/G_{\text{in}}$ under different diffusion coefficients; see Figure 3.4. Given the parameter sets used, the NFB-LEGI mechanism appears to be more efficient in gradient sensing than the IFF-LEGI.

3.1.4 Response after removal of the stimulus

We have shown that, at steady-state, the NFB-LEGI has desirable properties in terms of adaptation and gradient sensing. How does it respond to dynamic input?

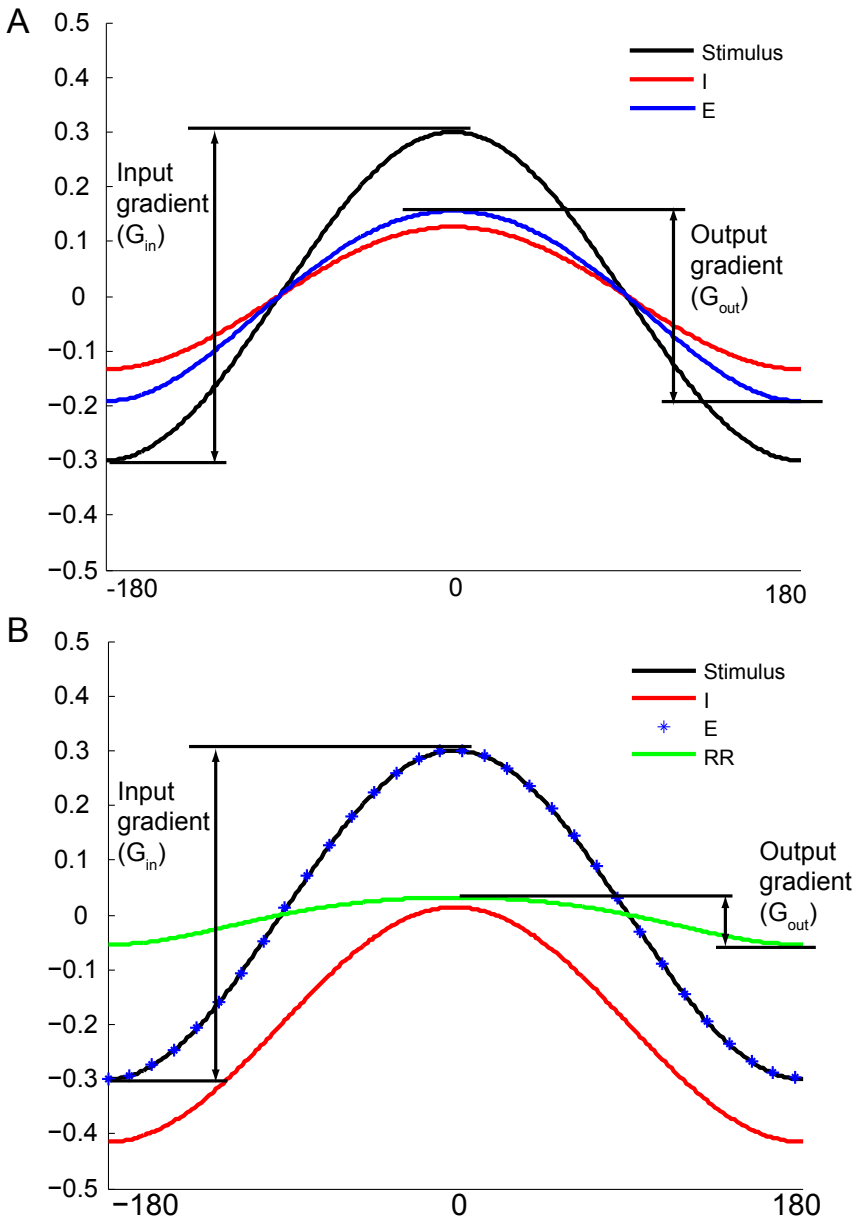

Figure 3.3: Gradient sensing in both the NFB-LEGI and IFF-LEGI. The θ-axis represents the angle around cell perimeter. All signals are shifted vertically by their mean level. G_{out} and G_{in} measure the signal differences between front and back.

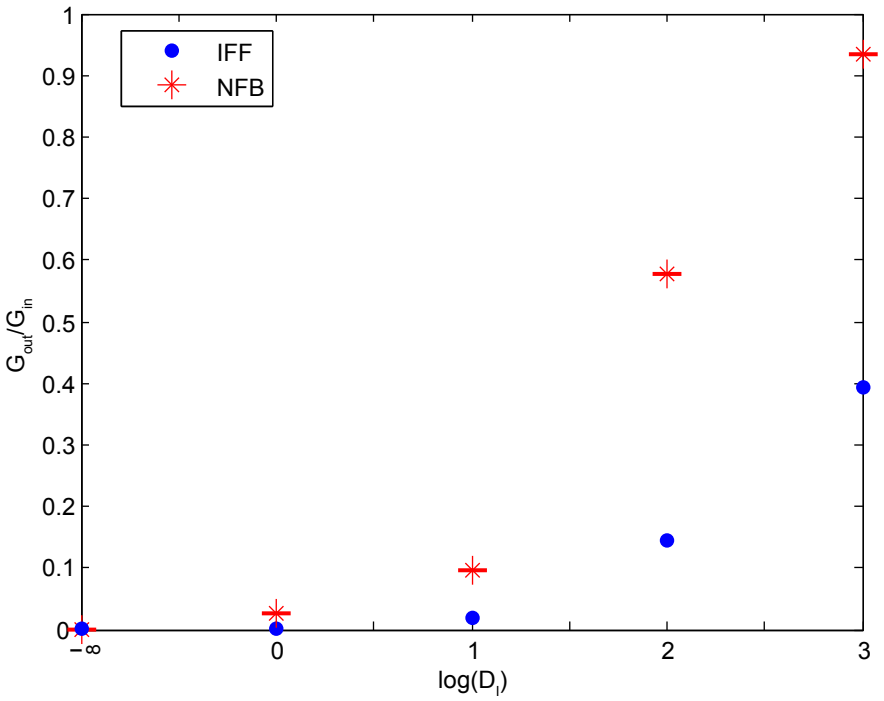

Figure 3.4: Gradient sensing efficiency of the NFB-LEGI and IFF-LEGI modules. The $-\infty$ in the x-axis means no diffusion.

3 Gradient Sensing

To test the NFB's capability, we compared the NFB-LEGI and IFF-LEGI modules in one simple situation: removal of a spatially homoegeneous stimulus from an adapted state. Simulations of this experiment using the NFB-LEFI displays damping oscillatory behavior after (Figure 3.5A). These oscillations take a long time to die out. In contrast, the IFF-LEGI shows only one shut-off before re-adapting (Figure 3.5B). We note that in both these cases, there is not complete removal of the stimulus, but rather the stimulus is reduced to 10% of the original level. It can be shown that after complete removal of the stimulus, the IFF does not return to its prestimulus value [67].

The damping oscillatory behavior can be explained as follows. The Jacobian matrix of systems at steady state (E_0, I_0) is:

$$J = \begin{bmatrix} -k_{-e}I_0 & -k_{-e}E_0 \\ k_i & -k_{-i}\frac{\epsilon}{(\epsilon+I_0)^2} \end{bmatrix}$$

If $I_0 \gg \epsilon$ then, using the fact that $E_0 = k_{-i}/k_i$ and $I_0 = k_e S_0/k_{-e}$, this is

$$J = \begin{bmatrix} -k_e S_0 & -k_{-e}k_{-i}/k_i \\ k_i & 0 \end{bmatrix}$$

The eigenvalues are given by

$$\frac{-k_e S_0 \pm \sqrt{k_e^2 S_0^2 - 4k_{-e}k_{-i}}}{2}.$$

When $S_0 > 0$, the real part of the eigenvalues is negative, showing that the system is stable. Moreover, if $k_e^2 S_0^2 > 4k_{-e}k_{-i}$, then both eigenvalues are real.

When the stimulus is removed, we have $S_0 = 0$ and the eigenvalues are imaginary, which makes the system exhibit damped, oscillatory behavior. This oscillatory behavior is not desirable when cells need to respond promptly to changes in the external environment.

We note that, though the real part of the eigenvalues are both zero, we can still show that the response goes to $E_0 = 0$ using LaSalle's invariance principle [68]. In particular, define the function

$$V(E) = \tfrac{1}{2}E^2.$$

Its derivative along the differential equations is

$$\dot{V}(E) = E\dot{E} = -k_{-e}IE^2 \leq 0.$$

If $\dot{V}(E) = 0$ then, either $E \equiv 0$ or $I \equiv 0$. If the latter, then $\dot{I} = 0$ in which case

$$0 = k_i E - k_{-i}\frac{I}{\epsilon + I} = k_i E = 0.$$

Thus, $E = 0$ as required.

3.1.5 Summary

This chapter proposed a new gradient sensing mechanism based on a negative feedback scheme. Using this scheme, we can save one variable compared with IFF-LEGI mechanism but still can realize both adaptation and gradient sensing. The gradient sensing strength is dependent on the inhibitor's diffusion rate. However, retracting stimulus results in damping oscillatory behavior which is not desirable.

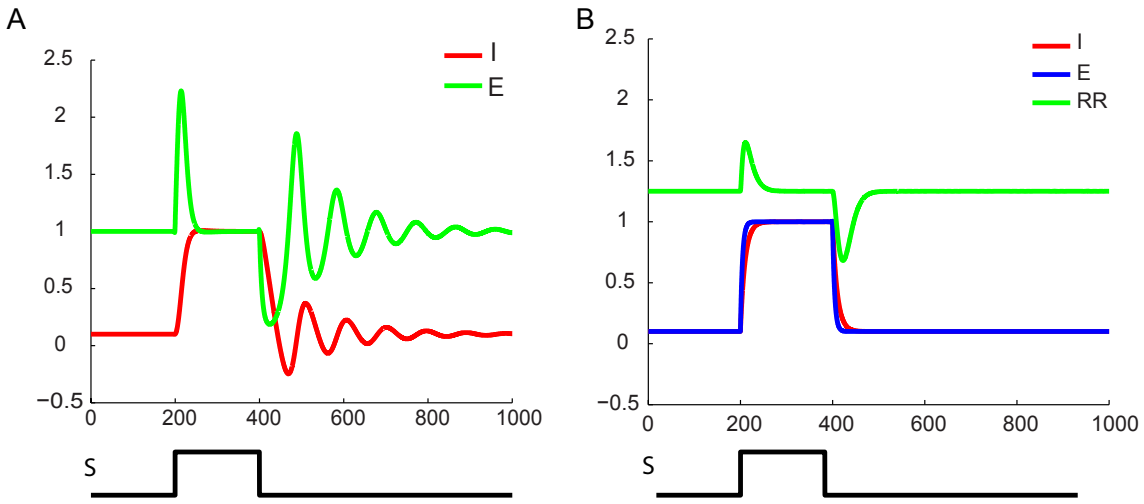

Figure 3.5: Retraction of uniform stimulus. (A) NFB scheme. (B) LEGI scheme.

Chapter 4

Linking the Signaling Activity to Cellular Protrusions

The LEGI-BEN model was reviewed in Chapter 2. It was proposed to account for a chemotactic cell's adaptation, gradient sensing and excitability. The LEGI-BEN model succesfully recreated cellular component's spatio-temporal distribution with or without stimulation [10]. The excitable activity of the signaling and cytoskeletal networks have been observed to be highly correlated with cell protrusions [10, 24] . Thus, Xiong et al. [10] proposed that the excitable activity can generate active forces that drive cell migration. This chapter tests this hypothesis by simulating cell migration using level set methods and assuming that the LEGI-BEN mechanism generates the active forces that drive cellular motion.

4.1 Simulating cell shape change with level set method

The level set method (LSM) and the viscoelastic cell mechanical model we use here were reviewed in Chapter 2. Here, I couple the excitable activity of the LEGI-BEN model to the LSM through the viscoelastic model.

4.1.1 Connecting signaling activity to level set model

The excitable network (EN) explains the spontaneous patches of signaling activity seen in motile cells (Figure 4.1A, B). Presumably, these patches represent localized signaling events, such as actin polymerization, that drive cell protrusions. To determine whether this model could recreate cellular protrusions leading to random cell motility, we coupled the EN to the viscoelastic model of cell cortex implemented in the level set framework (Figure 4.1C).

As discussed in Chapter 2, to evolve the potential function which tracks cell shape change, a membrane velocity $v(x,t)$ is needed, which can be computed by solving the viscoelastic model. Thus, we need to compute the total net stress (σ_{tot}) acting on the cell. This the vector sum of all stresses including contributions from both passive and active components. Specifically, we included:

1. **Surface tension.** This arises from Laplace-like pressures at the interface between two surfaces [69]. It is given by:

$$\sigma_{\text{ten}} = \gamma k(x)\mathbf{n},$$

where γ is the local cortical tension, k is the local curvature, and $\mathbf{n}$ is a normal

unit vector.

2. **Volume conservation.** We include a stress that acts to ensure surface area conservation,

$$\sigma_{vol} = k_{\text{area}}\big(A(t) - A_0\big),$$

where A is the surface area enclosed by the cell boundary either at time t or initially.

3. **EN-generated stress.** The activity of the EN was coupled to protrusive forces, so that higher activity at one location gave stronger protrusive stress (Figure 4.1C, D). We envision that the effects of the EN on the cytoskeleton mediate these protrusive forces, which are proportional to the signal Y (using X leads to similar results) according to

$$\sigma_{\text{pro}} = \sigma_0 \gamma(\theta)\mathbf{n}$$

representing actin polymerization. The conversion factor between the activity Y and the force is $35\,\text{nN}/\mu\text{m}^2$. Based on the typical maximum activity level for Y seen in the simulations (approximately 0.05 A.U.), this resulted in protrusive forces in the range of 1–$3\,\text{nN}/\mu\text{m}^2$, consistent with measured values of the maximum protrusive pressure due to actin polymerization (in the range of a few $\text{nN}/\mu\text{m}^2$).

Using these elements, we compute the total stress

$$\sigma_{\text{tot}} = \sigma_{\text{pro}} + \sigma_{\text{ten}} + \sigma_{\text{vol}}$$

and use this to update the viscoelastic model parameters (x_m and x_{cor}) in Equations 2.8 and 2.9.

The model and all simulations are implemented using Matlab. After solving the concentrations of species from excitable network (e.g. X and Y), we compute the protrusive force using the concentration for Y. Using this protrusive force and coupling with other passive force, we can compute the local membrane velocity $v(x,t)$ by solving the viscoelastic system. The velocity $v(x,t)$ is subsequently used to evolve the potential function in the level set simulations, as described above. The potential function is solved on a Cartesian grid with spatial discretization of 19 points per μm. The assignment of Y activity levels to the protrusive force is done on a point-to-point pairing based on correspondence between angular positions relative to the cell centroid. The level set simulations were carried out using the Level Set Toolbox for Matlab using the first order forward Euler method [70].

4.2 Simulation results

4.2.1 Cell shape change in absense of stimulus

In the level set simulations, local protrusions appeared randomly around the cell, as would be expected in a cell undergoing random motility (Figure 4.1D). Analysis of these simulations over time revealed that the activities were uniformly distributed at the population level over long time scales, though localized fluctuations do occur on shorter time scales (Figure 4.1D, inset). The localized forces caused by these hetero-

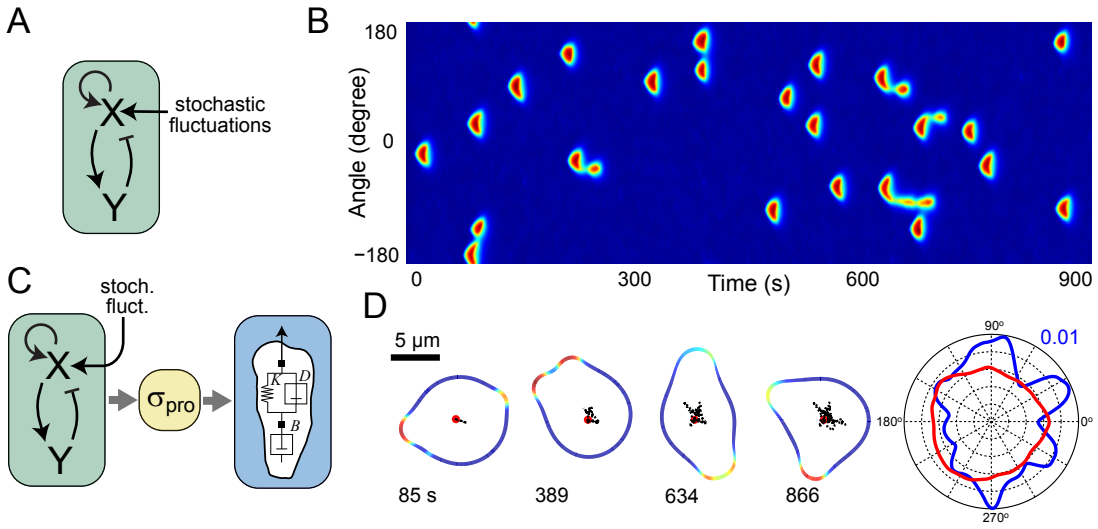

Figure 4.1: Connecting excitable network to level set method. (A) The excitable network module is implemented as an activator (X)-inhibitor (Y) system that is triggered by stochastic fluctuations. (B) Kymograph of a one-dimensional simulation in the absence of chemoattractant stimulus. The colors refer to activity of Y (plots of X show similar, though noisier, behavior) around a cell. Blue indicates low activity; red marks high activity. (C) Coupling of the excitable network to protrusive stresses (σ_{pro}). Our simulations assume that the protrusive stress is proportional to Y. The cell's mechanical behavior is described by the viscoelastic model shown. (D) Level set simulations in which protrusive stresses coincide with the location of high activity drive cellular deformations. The colors around the membrane are the same as in panel B. The dotted lines trace the trajectory of the cell centroid (starting point is the red circle). The directional history of activity for this sample simulation is shown in the radial plot on the right in blue. The red line represents the average activities of 20 simulations lasting 900 seconds. Reprinted from [71].

geneities, however, were not sufficiently persistent to propel the cells in a meaningful way. Thus, the cellular boundary extended in random directions, but the migration rate of the cell was negligible.

4.2.2 Cell migration under gradient

To test the effect of a chemoattractant gradient, we added the LEGI mechanism to the EN, creating a LEGI-BEN system and connected it to the LSM (Figure 4.2A). Because the response regulator in the LEGI mechanism increases at the front and decreases at the back, it brings the excitable system closer or farther from the threshold at the front and back, respectively. This biases the likelihood of triggering activity in response to external chemoattractant signals. When a gradient was applied to an unstimulated cell, the activity of the cell increased everywhere around its perimeter. Thereafter, signaling activity was found preferentially at the side of the cell experiencing the greatest chemoattractant concentration (Figure 4.2B). The cellular response to a change in gradient was nearly immediate, and this was true for both steep (19%) and shallower (6%, not shown) gradients. When simulating cell shape changes elicited by this gradient, we found that after the application of the stimulus, the cell elongated and moved in the direction of the gradient. Analysis of the activity showed that the directional response was quite accurate and most of the activities were within the -30° to 30° region relative to the direction of gradient (Figure 4.2B, inset). The magnitude of the protrusive force was chosen so that, at steady-state, the cells moved at approximately $10\,\mu$m/min. After a shift in the direction of the

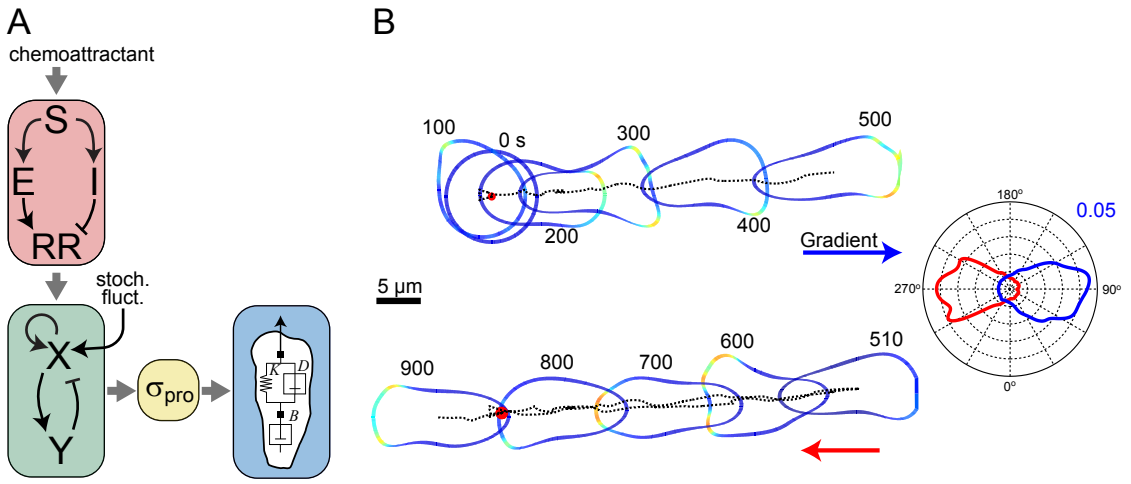

Figure 4.2: Connecting LEGI-BEN to level set method. (A) The local excitation (E)-global inhibition (I) module (LEGI) takes chemoattractant stimulus (S) and drives a response regulator (RR). Response regulator acts to bias the activity of the excitable network. (B) Level set simulations of the cell migrating in response to changing chemoattractant gradients. A gradient was applied at time 180 s at 90° moved at time 500 s to 270°. (Note that, to avoid the cell shapes being superimposed, we have moved the trajectory during the second half of the simulation below that of the first; the dotted lines show how the two halves of the trajectory overlap.) The radial plot shows the average activities in response to the two gradients. The blue line is for the time period from 0 to 500 s; red is from 500 to 900 s. Reprinted from [71].

gradient, the cell stopped and reversed direction nearly instantly.

4.2.3 Pseudopod splitting and cringing

The LEGI-BEN coupled to the mechanical module recapitulates several consistently observed cellular behaviors including "pseudopod splitting" and "cringing". First, cells often generate a new pseudopod by splitting an existing one [11, 15]. In chemotaxing cells, these bifurcations appear as a series of left-right extensions. Our simulations of chemotactic cells also exhibited "pseudopod splitting" (Figure 4.3A).

Because the midpoint of the responding area has the highest activity, negative feedback shuts down this region first, the signals propagate away in opposite directions and the pseudopod splits. Though more pronounced in stimulated cells, it was also observed during spontaneous movement (Figure 4.1D, 389 s). Nascent extensions grew from localized patches of high signaling activity. These pushed the cell forward, but eventually split in two (Figure 4.3A, 20–40 s). While these extensions sometimes co-existed for a while (Figure 4.3A, 80 s), one usually won out, at which point the "losing" pseudopod appeared to retract into the cell (Figure 4.3A, 100–120 s). This pattern often repeated itself, giving rise to the appearance of side-to-side strokes propelling the cell.

Application of a spatially uniform dose of chemoattractant to a *Dictyostelium* cell results in a series of changes in cell morphology. Cells stop moving and then transiently contract (or cringe). This is followed by spreading and eventual resumption of movement. Our simulation also recreated this phenomenon (Figure 4.3B). Approximately 30 s after stimulation, the cell experienced a mostly global rise in signaling activity. At this point the protrusive stresses in our model sought to push out the cell everywhere, but because of the passive constraints on cell morphology, this global increase in activity had the effect of rounding up the cell. The increase of activator subsequently generates more inhibitor. Once the inhibitor prevails, it suppresses activity all around cell. Thus, the global firing was followed by an absence of signaling caused by the refractory period that follows the firing of an excitable network lead-

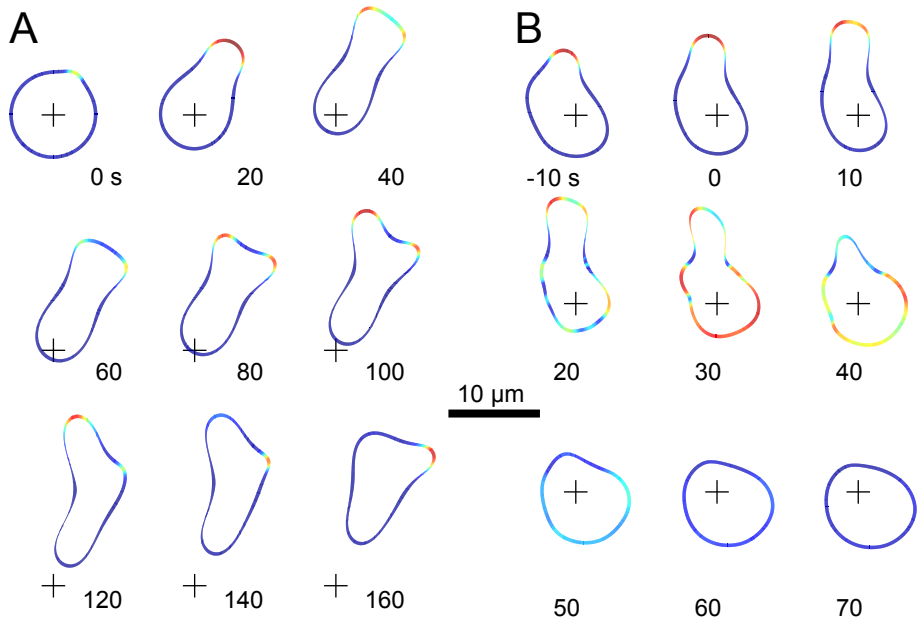

Figure 4.3: Changes in morphology of motile cells. (A) The signaling activity and corresponding cellular morphology is shown for a migrating cell in a gradient. This cell demonstrates pseudopod splitting, pseudopod retractions, and a zig-zag pattern of activity. The cross is placed for spatial reference. (B) This cell experienced a global (spatially uniform) chemoattractant stimulus at 0 s. The ensuing period of high activity (30 s) causes the cell to start rounding up; this rounding increases during the refractory period of the excitable network (70 s). Reprinted from [71].

ing to further rounding of the cell. This was followed by spreading and eventually activities reappeared stochastically around the parameter (not shown).

4.3 Summary

This chapter coupled the level set method to the LEGI-BEN model and successfully simulated cellular morphology changes. This model connects the signaling activities to cell protrusion and generate realistic cell shape change.

While the simulations accurately displayed the chemotactic behavior of unpolarized cells, these cells lacked two important characteristics observed in stably polarized cells. First, polarized cells moving in the absence of chemoattractants travel in a persistent random walk, and this persistence is a result of having pseudopodia extend in the same direction [11, 33–36]. Second, they have an elongated morphology with activity confined to the anterior portion of the cell. *Dictyostelium* cells at an early stage in their developmental program are mostly unpolarized but the degree of polarization increases as they differentiate [28]. In contrast, once activated, neutrophils are highly polarized.

The inability to recreate polarization suggests that the LEGI-BEN model cannot capture all chemotactic behaviors. More features and elements need to be added, and this will be the focus of the next chapter.

Chapter 5

Polarity: A Missing Piece in the Model

Chapters 2 and 3 introduced the LEGI-BEN system. The LEGI mechanism explains adaptation and gradient sensing of the chemoattractant stimuli. The EN explains the spontaneous patches of signaling activity seen in motile cells, which presumably represent localized signaling events that drive cell protrusion and cell motility. When coupled in a LEGI-BEN system, the LEGI mechanism biases the location where these EN-generated patches occur, making their appearance more likely in the direction of the chemoattractant gradient. Chapter 4 incorporated the LEGI-BEN system into the level set method (LSM) and recreated realistic changes of cellular morphology driven by the signaling activities of the LEGI-BEN system. When in a chemoattractant gradient, these simulated cells migrated. The simulations also recreated some

observed characteristic cellular behaviors, including pseudopod splitting and cringing. However, we noted that these cells lacked one important characteristic: polarity. Moreover, in our simulations of randomly generated cell protrusions (Figure 4.1D), the localized forces caused by these heterogeneities were not sufficiently persistent to propel the cells in a meaningful way. Thus, the cellular boundary extended in random directions, but migration of the cell was negligible

Polarity enables cell in the absence of chemoattractants to carry out a persistent random walk, and this persistence is a result of having pseudopodia extend in the same direction [11, 33–36]. Cells with strong persistence make fewer turns, move for prolonged periods of time in the same direction, and thereby effectively extend into the surrounding regions. This suggests that persistence may have a major impact on how cells colonize a new environment. By increasing the persistence time, cells disperse better during food seeking [72], move longer distances during morphogenesis [73, 74] and may escape into the environment during metastasis [75].

5.1 Polarity module

To overcome these limitations and recreate more realistic cellular behavior, we introduced an additional module to create a polarized-LEGI-BEN system. To this end, we incorporated in the excitable network a secondary set of feedback loops from the cytoskeleton. These are indicated by an arrow linking protrusive stress to the signaling element (Figure 5.1). We refer to this complete model as the *polarized*

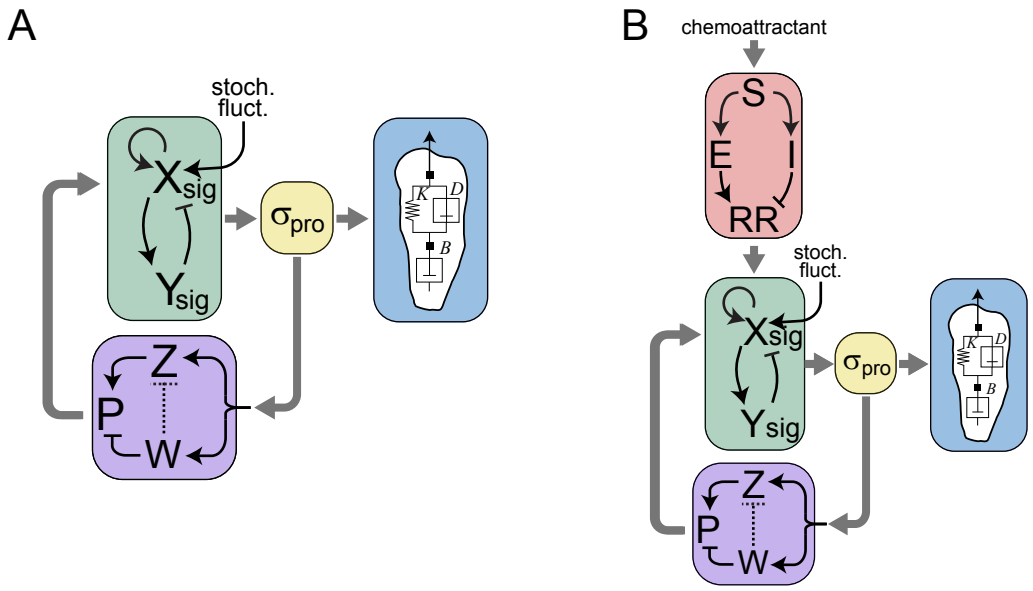

Figure 5.1: LEGI-BEN with polarity module. (A) Polarity influences the excitable network. The polarization mechanism consists of complementary local positive (Z) and global negative (W) feedback loops. The inhibitory term (W) can work either directly on polarity (P) or by inhibiting Z (dotted line). The latter could represent depletion. In simulations we assumed the former. (B) LEGI-BEN with polarity module. LEGI and polarity module together bias excitable activities. Reprinted from [71].

LEGI-BEN.

Positive feedback loops have been a feature of most models of polarization (reviewed in [43, 76]) based on experimental evidence that polarization is a consequence of such loops between actin and signaling proteins [77]. In our context, a local positive feedback loop (element Z in Figure 5.1A) biases the likelihood of subsequent activity at the location of high protrusive stresses. Thus, because stresses are caused by localized increases in signaling activity, whenever high activity occurs at one location, it is more likely that subsequent bursts of activity will reoccur at that position. However,

adding a positive loop is not enough to realize polarity. First, there is a lifetime to this persistence, and so the contribution of this loop is expected to subside. Second, without a counteracting negative feedback, the effect of the loop could increase over time throughout the cell, and so lead to hyperactive cells. We therefore included a global negative feedback loop that reduces the activity throughout the cell. This loop was implemented as a separate component (element W in Figure 5.1A) that acts to reduce polarization. A second possibility for this inhibition would be to act against Z directly (dotted line in Figure 5.1A) as might be expected if the inhibition were in the form of substrate depletion. Negative feedback loops are less common in models of polarization, though several models assume mass conservation of the polarity element, which has the same net effect [78–80]. Importantly, averaged over the surface of the cell, the two loops cancel each other out. However, the net effect of the two components is positive at locations of high stress and is negative elsewhere.

5.2 Polarized-LEGI-BEN

The complete model now consists of three modules: excitable network, polarity module and LEGI. Here we provide a description of the system and carry out simulations of the combined system.

5.2.1 Mathematical description

Polarity module

The polarity mechanism is given by $P = Z - W$, where the individual components are also implemented as a local excitation, global inhibition mechanisms:

$$\frac{\partial Z}{\partial t} = -k_{-Z}Z + k_Z\sigma_{pro} + D_Z\nabla^2 Z \tag{5.1}$$

$$\frac{\partial W}{\partial t} = -k_{-W}W + k_W\sigma_{pro} + D_W\nabla^2 W. \tag{5.2}$$

For simplicity, we let D_W be sufficiently high that W is spatially independent. The polarization module is activated by signal σ_{pro}, which represents actin polymerization and is proportional to Y_{sig}.

LEGI

The LEGI mechanism involves three interacting processes (Figure 5.1B). An external signal, which represents the local level of receptor occupancy (S), drives two of them: a fast, local excitation (E), and a slow, global (diffusible) inhibitor (I). These two control a response regulator, which can be active (R) or not ($R_T - R$), where we have assumed that the total concentration (R_T) of the response regulator is constant. The system equations are given by:

$$\frac{\partial E}{\partial t} = -k_{-E}E + k_E S \tag{5.3}$$

$$\frac{\partial I}{\partial t} = -k_{-I}I + k_I S + D_I\nabla^2 I \tag{5.4}$$

$$\frac{\partial R}{\partial t} = -k_{-R}IR + k_R(R_T - R)E. \tag{5.5}$$

5 Polarity: A Missing Piece in the Model

In the gradient simulations, the initial stimulus level is given by:

$$S(r) = S_0 \frac{\ln r_\infty - \ln r}{\ln r_\infty - \ln r_{needle}} \tag{5.6}$$

where r is distance from each point on the cell boundary to the location of a hypothetical needle, which is either 10 μm (19% gradient) or 100 μm (6% gradient) away. This equation corresponds to the steady-state solution of the diffusion equation from a 5 μm needle in radial coordinates. The gradient is not updated as the cell moves to ensure that the gradient steepness is maintained. The gradient is defined as:

$$\text{Gradient} = 2\frac{S_{\text{front}} - S_{\text{back}}}{S_{\text{front}} + S_{\text{back}}}. \tag{5.7}$$

Excitable network

We assume that the signaling network behaves as an excitable network (Chapter 2, [10]). It consists of two species (Figure 5.1A). Component X_{sig} acts as the activator: it is autocatalytic (it has strong positive feedback), and also activates the downstream component—we refer to this as the feedforward loop. The Y_{sig} component provides negative feedback to X_{sig}. A reaction-diffusion network, consisting of the partial differential equations:

$$\frac{\partial X_{sig}}{\partial t} = \alpha_{sig}\frac{X_{sig}^2}{k_{sig}^2 + X_{sig}^2} - \beta_{sig}X_{sig} - \gamma_{sig}Y_{sig} + \rho_{sig}U_{sig} + D_{X_{sig}}\nabla^2 X_{sig} \tag{5.8}$$

$$\frac{\partial Y_{sig}}{\partial t} = \delta_{sig}X_{sig} - \epsilon_{sig}Y_{sig} + D_{Y_{sig}}\nabla^2 Y_{sig} \tag{5.9}$$

describes the evolution of the activities of these two species. Both components in this subsystem can diffuse spatially, with diffusion coefficients $D_{X_{sig}}$ and $D_{Y_{sig}}$, re-

spectively. The signal U_{sig} is the input to the excitable system, which incorporates several components: a basal level of activation (B), a stochastic component (N), contribution from the LEGI response regulator (R, described above) and the polarization component (P, described below). The contribution of each of these is additive:

$$U_{sig} = B + N + \lambda(R - R_{init}) + \varphi P. \tag{5.10}$$

The stochastic component is modeled as zero mean, white noise process with variance one. Note that, in this context, the external gradient and the internally developed polarity compete to direct cell motion.

5.2.2 Model implementation

The model and all simulations are implemented using Matlab. Simulations were carried out in two steps. First, the PDEs for the signaling were solved around cell perimeter by representing the cell boundary as a one-dimensional system using periodic boundary conditions. This was discretized in space using 360 points. Spatial diffusion terms, which contain the second derivatives, are approximated by central differences in space; and by doing that, the partial differential equations are converted to ordinary differential equations. The solution of the stochastic differential equations was obtained using the SDE toolbox for Matlab [81]. The time step for simulation was set to 0.025 seconds. After solving the concentrations of all species (e.g. X, Y, W, and Z), we compute the protrusive force using the concentration for Y, and use this protrusive force to update the potential function in the level set simulations, as

described in Chapter 4. The potential function is solved on a Cartesian grid with spatial discretization of 19 points per μm. The assignment of Y activity levels to the protrusive force is done on a point-to-point pairing based on correspondence between angular positions relative to the cell centroid. The level set simulations were carried out using the Level Set Toolbox for Matlab using the first order forward Euler method.

5.2.3 Parameters

The parameters are shown in Table 5.1. Parameters for the LEGI and EN components were used in our previously published model [10]. The parameters of viscoelastic model were obtained using by fitting experimental measurements of aspirated *Dictyostelium* cells using a micropipette, as previously reported [56].

To choose the parameters for the polarization model we used as a benchmark that the persistence of cells is in the order of two minutes. Since the equations driving the polarity module are linear, the appearance of a pseudopod (represented by a sudden increase in σ_{pro}) leads to an increase in Z followed by an exponential decay with rate $e^{-k_z t}$ (ignoring diffusion). Our nominal value for k_Z is such that $1/k_Z$ is approximately 1/66 seconds, which implies that the effect of that pseudopod is reduced to only $e^2 \approx 0.13$ after two minutes. Note that during this time, more firings are possible, so that the effect of that initial pseudopod will likely be felt for longer periods. The time scale for the inhibitory element of the polarization module was chosen initially chosen in the same way. To arrive at the final values, we iterated in an ad hoc fashion, making

sure that the activity of the excitable system (X and Y) showed some persistence in angle, but did not become locked in one position (sufficiently large feedback through the polarity module can lead to a bistable system).

5.2.4 Analysis methods

To measure the persistence, we used the autocorrelation function $C(t)$, measured at a fixed angles:

$$C(t) = \frac{\Sigma_i (Y_\theta(t_i) - \mu)(Y_\theta(t_i + t) - \mu)}{\Sigma_i (Y_\theta(t_i) - \mu)^2} \tag{5.11}$$

where μ is the mean level of signal. We also calculated chemotaxis index to measure the precision of directed migration. Chemotaxis index was computed using this formula:

$$\text{CI} = \frac{\Sigma d_i \cos(\theta_i)}{\Sigma d_i}. \tag{5.12}$$

After application of the gradient the cell trajectory was sampled every five seconds: P_i. The values d_i are the distances from sample points P_i and P_{i-1}; θ_i is the angle between the line connecting P_i and P_{i-1}, and direction of the gradient.

5.3 Results

5.3.1 Polarized excitable network in absence of stimulus

We first carried out simulation in absence of external stimulus. Simulations of the polarized-EN system in an unstimulated cell showed persistence in the location of the excitable behavior (Figure 5.2). For example, in the kymographs of Figure 5.2A, high

Table 5.1: Parameters of Polarized LEGI-BEN Model

Excitable network			
$D_{X_{sig}}$	0.016 μm^2/s	$D_{Y_{sig}}$	0.038 μm^2/s
α_{sig}	2.5 s^{-1}	δ_{sig}	0.019 s^{-1}
β_{sig}	2.3 s^{-1}	ϵ_{sig}	0.088 s^{-1}
k_{sig}	0.32	B	-0.063
γ_{sig}	8.6 s^{-1}	R_{init}	1.25
ρ_{sig}	0.8 s^{-1}	λ	2
φ	2		
Polarity module			
k_Z	0.023 s^{-1}	k_{-Z}	0.015 s^{-1}
k_W	0.035 s^{-1}	k_{-W}	0.012 s^{-1}
D_Z	0.04 μm^2/s		
LEGI module			
k_e	0.5 s^{-1}	k_{-e}	0.5 s^{-1}
k_i	0.1 s^{-1}	k_{-i}	0.1 s^{-1}
k_r	0.06 s^{-1}	k_{-r}	0.1 s^{-1}
R_T	2 A.U.	D_I	1 μm^2/s
r_n	5 μm	r_∞	1 m
k_{UX}	0.8 s^{-1}	λ	2
S_0	0.1 A.U.	(0.2 in Figure 5.8C)	

activity during the period 0–500 s was centered around $-90°$ whereas, after 600 s, it was around $+90°$ (Figure 5.2B). These kymographs show that polarity had a localized and transient biasing effect in terms of activity. However, integrating the activity of 40 simulations (each 900 s long) showed that, on average, the location of high activity was uniformly distributed around the cell as would be expected in a randomly migrating cell (Figure 5.2C). To examine the temporal effect of the polarization module on the appearance of excitable behavior in any one direction, we computed the autocorrelation function for the activity at fixed angles (Figure 5.2D) by choosing 10,000 angles and time points at random. Without the polarity module, the autocorrelation decays quickly (to less than 0.2) in approximately 30 seconds. With the nominal parameter values of the polarization module, there is a decay (the initial correlation can be accounted by the firings of the excitable system) but the autocorrelation plateaus at approximately 0.4. Increasing the timescale of the polarization component (by making the degradation slower can increase this plateau). Increasing the degradation constant of Z eliminates any long-term correlation.

To observe the effect of this persistence on cell motility, we used the polarized EN to simulate cell motility and changes in cell morphology (Figure 5.3A). These simulations showed that unstimulated cells could move significant distances, though the direction and net velocity were random (Figure 5.3B). Moreover, as the strength of the polarization increased (by varying parameter φ), the cells drifted farther away from the initial position, as measured by the mean squared displacement (Figure 5.3C,

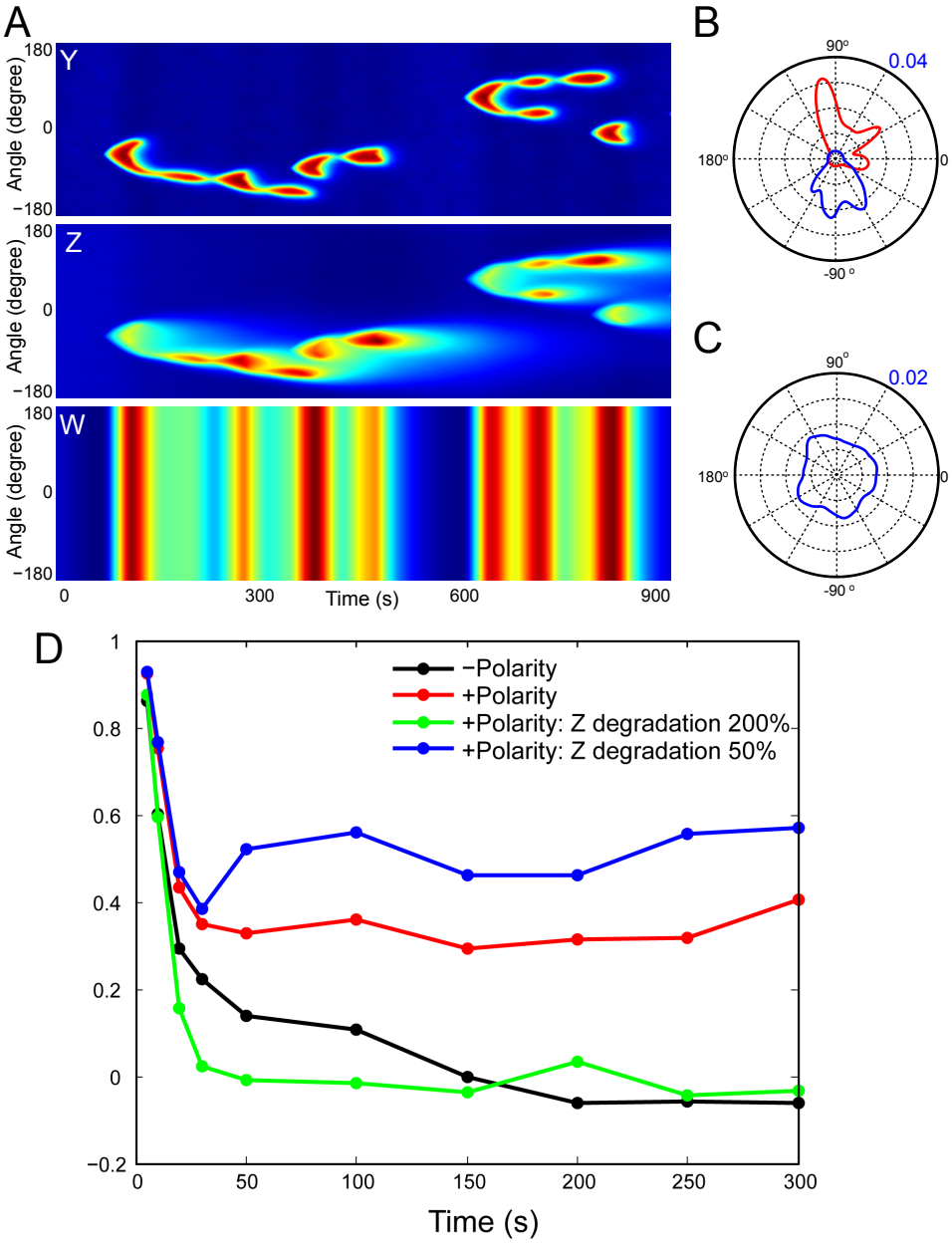

Figure 5.2: Persistent signaling events of polarized-biased excitable network. (A) Simulation results of excitable network with polarity. Kymographs show the spatio-temporal distribution of Y_{sig}, Z and W. (B) Analysis of activity for the simulation of panel A. The blue and red lines represent the activities (Y_{sig}) along the perimeter during the periods 70–490 s and 600–850 s, respectively. (C) Average activity of 40 simulations, each 900 s long. (D) Autocorrelation of the activity of Y_{sig} for fixed angles under varying scenarios on the lifetime of the polarization module. Changes in the lifetime were obtained by varying the parameter k_Z, that specifies the degradation rate of Z. Reprinted from [71].

D). These results follow closely observations which show that randomly migrating *Dictyostelium* cells 5.5 hours into development have mean-squared displacements that are approximately ten times higher than newly developed cells [36]. The length of development time also correlates with the degree of morphological polarization [28].

5.3.2 Response to uniform stimuli

We next simulated the response to a spatially homogeneous stimulus. Before stimulation, the cell displayed random spontaneous activity (Figure 5.4A, B). In response to the stimulus, activity increased transiently around the perimeter, lasting approximately 30 seconds. Thereafter, activity subsided throughout, before resuming their spontaneous activity (as the LEGI mechanism adapted to the uniform stimulus). In contrast to cells lacking the polarity mechanism (Figure 5.4B, bottom), which displayed a strong secondary peak of elevated activity around 120 seconds after the chemoattractant stimulus, cells with the polarity mechanism do not exhibit this secondary peak (Figure 5.4B, top). Consistent with our simulation results, there is widespread experimental evidence for a second peak in early-stage less polarized cells, but it is less pronounced (or nearly absent) in well-developed polarized cells [28]. Without the polarity module, the second peak appears because the LEGI module has not adapted completely, and so secondary firings of the excitable system take place. With the polarization module, the presence of an extra negative feedback loop (W) makes these less likely, effectively eliminating them.

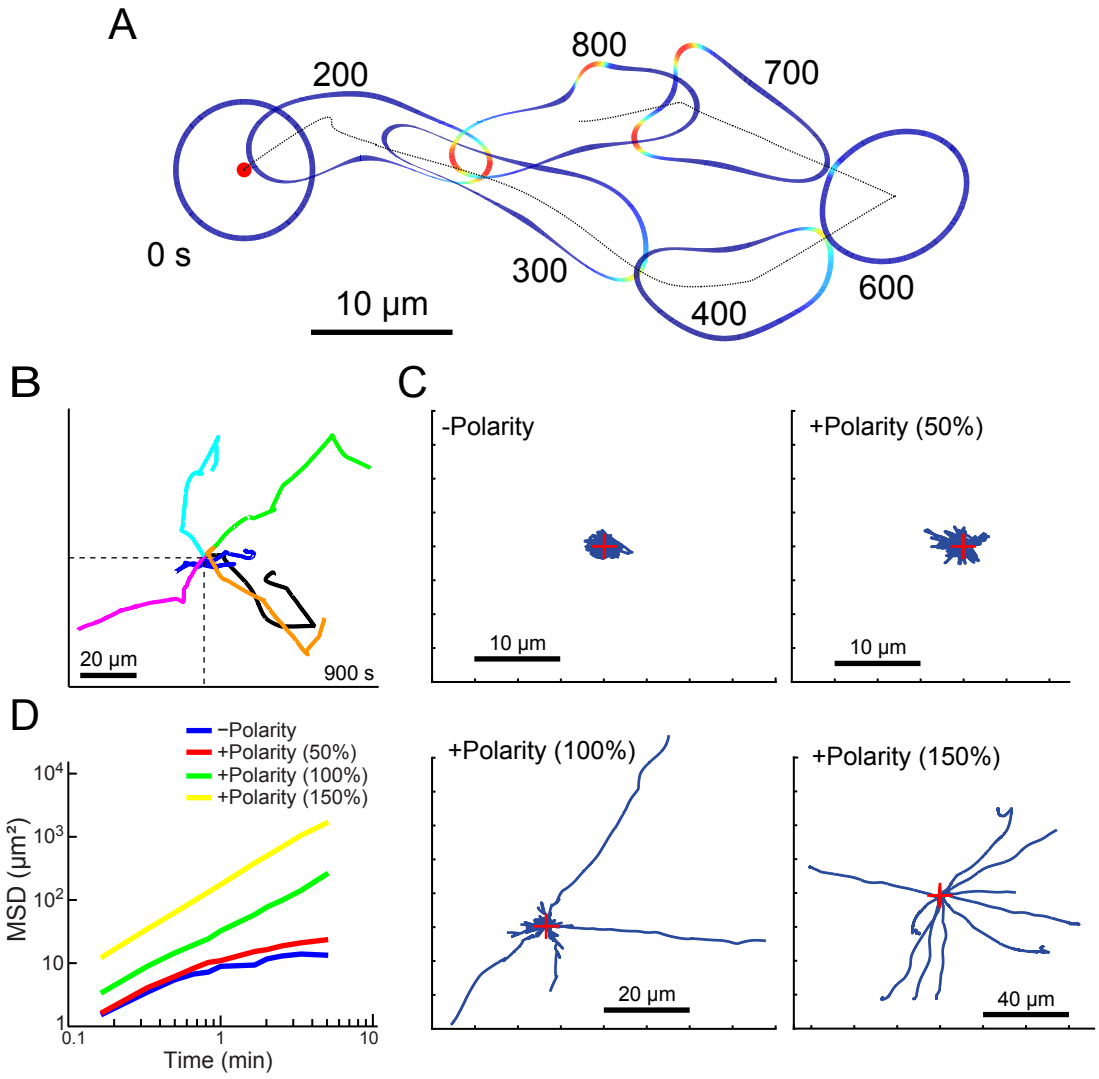

Figure 5.3: Persistent random cell migration simulated using level set method with polarized cell. (A) A cell migration resulting from the signal activity in (Figure 5.2). (B) Centroid trajectories of six different cells during 900 s. (C) Centroids of unstimulated cells with varying strengths of the polarity module's contribution during 600 s simulations ($n = 10$ each). (D) Average mean-square displacements as a function of time for the simulations of panel B. Reprinted from [71].

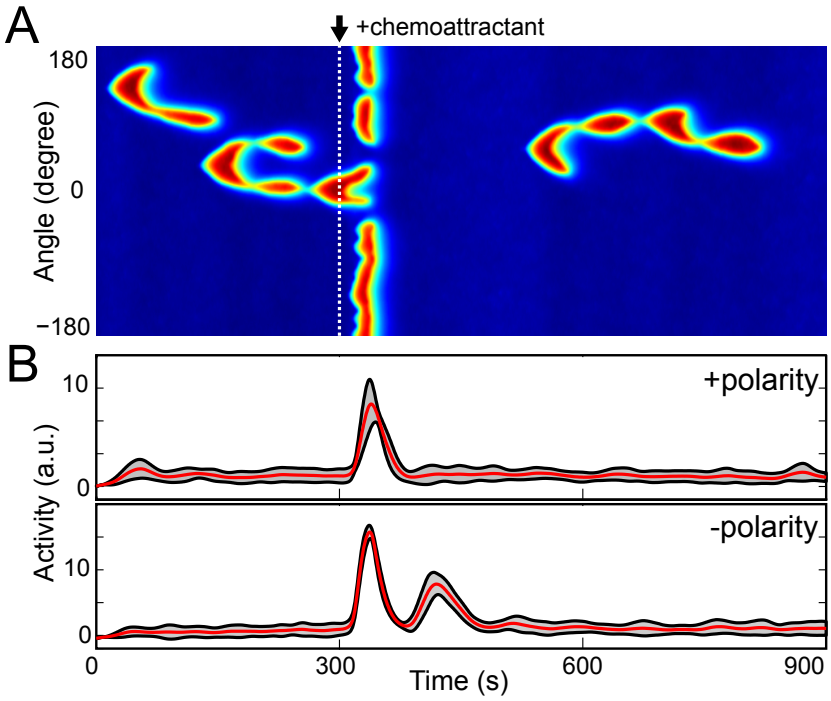

Figure 5.4: Polarized LEGI-BEN under uniform stimulus. (A) Signaling activity (Y_{sig}) around the cell in response to a spatially uniform stimulus at 300 s. (B) Average activity (red) and variance (one standard deviation) for 20 simulations. Activities are integrated around the whole cell perimeter. Top graph represents the results of the polarized, LEGI-BEN; bottom is for the model without polarity. Reprinted from [71].

5.3.3 Response to gradient

We next tested the effect of gradients of varying steepness (Figure 5.5). In all cases the activity of the cell aligned preferentially in the direction of the gradient. In 19% gradients the activity was concentrated in the region around $\pm 30^\circ$ and lateral pseudopods were rarely observed. In 6% gradients the response was still predominantly biased in the direction of the stimulus, but lateral pseudopods were observed occasionally. In 1% gradients, there was alignment, but considerable more spread.

The alignment of the activity with the gradient in simulations of cells lacking the polarity mechanism also showed dependence on the gradient steepness (Figure 5.5A, C, E). In all cases, the activity in polarized cells showed better alignment with the gradient and less variability. Using the level set simulations to compare the trajectory of cells in response to these varying gradients revealed a similar gradient-dependency. Cells responded better to the steeper gradients, as evidenced by straighter trajectories (Figure 5.5G-I) and greater chemotactic indices (CI) (Figure 5.5J). For cells with the polarity module, these ranged between 0.17 ± 0.02 to 0.64 ± 0.21 to 0.93 ± 0.02 in 1%, 6% and 19% gradients, respectively ($n = 7$ in each case). These are similar to reported values in the literature. For example, CIs of 0.2, 0.6 and 0.9 were measured for cells chemotaxing in relative gradients of 1.4%, 4.8% and 10%, respectively [11]. The latter gradients were imposed by a cAMP filled micropipette. In gradients created by microfluidics, which are closer to ours since they are not formed by a point source, CIs of 0.1–0.3, 0.15–0.4 and 0.96–0.99 have been measured in 1.25%, 2.5% [82] and

13.2% gradients [83].

5.3.4 Response to shift gradients

One of the main differences between polarized and unpolarized cells is in the response to changing gradients [14]. In a cell with the polarity module, we first applied a 6% gradient, maintained this for 10 minutes, and then shifted the gradient 90° (Figure 5.6A). Prior to any stimulus, the cell migrated randomly. After sensing the first gradient, the cell slowly aligned itself in the direction of the gradient and began migrating. After the direction of the gradient changed, the cell maintained its axis of activity and began a slow turning motion eventually realigning with the new gradient (Figure 5.6A). A similar turning motion was observed when the direction of the 6% gradient was changed 180° (Figure 5.6B).

We next repeated this simulation in a cell without the polarity mechanism (Figure 5.6C). The response in the direction of the initial gradient was similar, although unpolarized cells lined up faster than polarized cells. Furthermore, after the change in the direction of the 6% gradient, the cell immediately shifted its activity in the new direction, no longer extending pseudopods in the old front but instead focusing its activity in the direction of the new gradient (Figure 5.6C inset). Thus, the cell trajectory exhibited a nearly 90° turn. Finally, we carried out this simulation in a cell with the polarity module, but in the presence of 19% gradients (Figure 5.6D). The response to the initial gradient was similar to the previous simulations, though the activity in response to the steeper gradient was more focused than that toward the

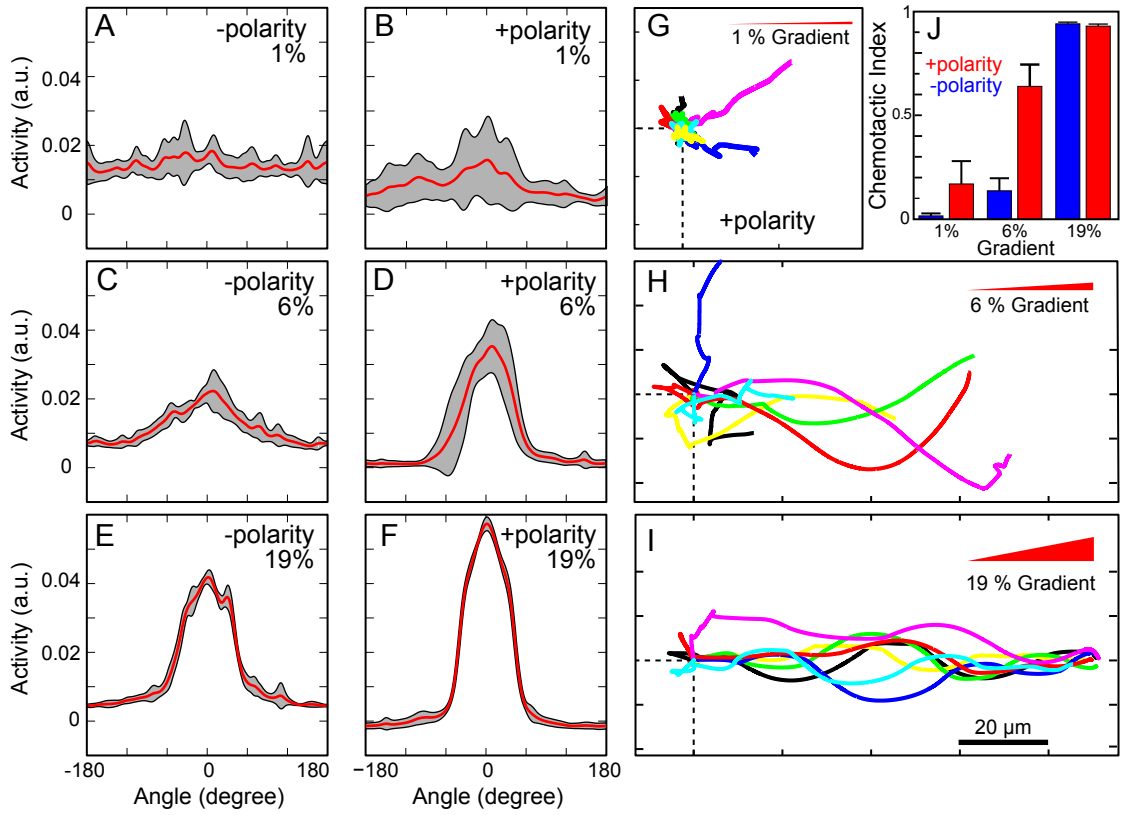

Figure 5.5: Polarized LEGI-BEN under gradient. (A-F) Radial distribution of signaling activities of the model responding to 1% (A, B) or 6% (C, D) and 19% (E, F) gradients. Panels A, C and E are for cells without the polarization module; panels B, D, and F include this module. Data are average for ten simulations of 900 s. Red lines denote mean value and black lines represent one standard deviation. (G-I) Sample trajectories of the cell centroid for level set simulations of cells incorporating the polarization module under various gradients (all pointing to the right). The dotted lines point to the starting point and lines represent individual cells' trajectories. All the simulations were run for 900 seconds. (J) Chemotactic indices for simulations of cells migrating under various gradients with or without the polarization module. Error bars denote one standard deviation based on seven simulations each. Reprinted from [71].

shallower gradient (as previously observed in Figure 5.5) enabling the cell to move further along the gradient during the initial 900 s (compare the location of the cells at 900 s in Figure 5.6A and D). After the change in gradient location, however, the polarized cell made a sharp 90° turn towards the new gradient. Thus, the response of a polarized cell to steep (19%) gradient changes was similar to that of an unpolarized cell to shallower (6%) gradient changes. These simulations show that polarity can be overcome by sufficiently strong gradients.

It has been observed experimentally that polarity can also be reinforced by a period of directed movement in a gradient [25]. To investigate how the time during which a cell is exposed to a gradient affects the development of polarity, we carried out simulations in which the time between application of the two gradients was altered. In Figure 5.6E, F, cells migrated in response to a 12% gradient. The location of this gradient was changed 90° after either 130 (Figure 5.6E) or 430 s (Figure 5.6F). When the initial migration time was small, the cell made a sharp turn, displaying little polarity. However, when the cell had been migrating longer in the gradient, the cell displayed the turning behavior associated with polarized cells. These simulations show that, in our model, as in real cells, polarization is a property that develops over time, and is reinforced by the time during which the cell is exposed to a stable gradient.

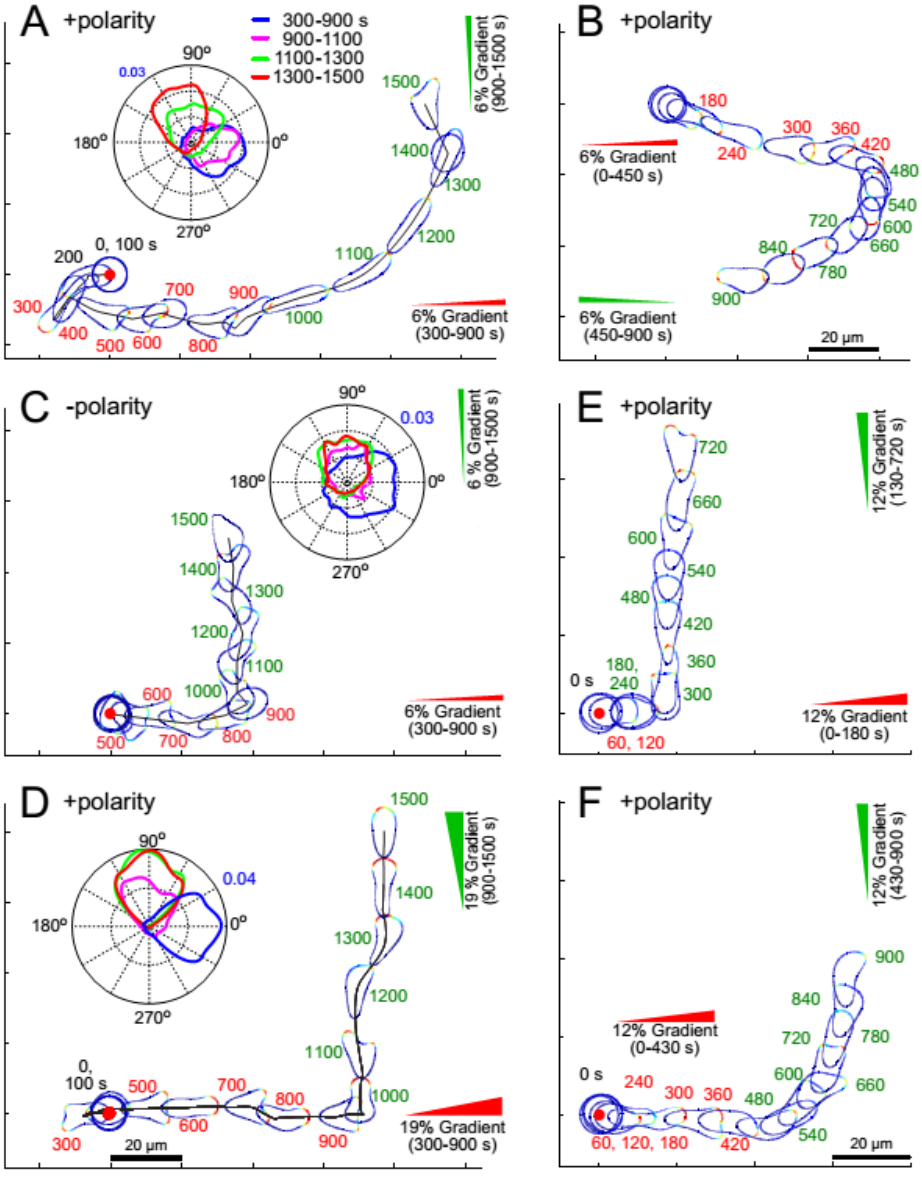

Figure 5.6: Polarized cell's response to changes in the direction of the gradient. (A-D) In these simulations the arrows indicate the direction of the gradient from 300-900 s (red) and from 900-1500 s (green). Cells were unstimulated from 0-300 s. The simulations differ as to the steepness of the gradient: 6% (A-C) and 19% (D), whether the polarity module is active (A, B, D) or not (C), and the direction of the second gradient: 90° (A, C, D) and 180°(B). The insets show the direction of the signaling activity relative to the cell for various time intervals. (E, F) These simulations show the response of a cell with all its modules responding to a change in the direction of a 12% gradient for which the interval during which the first gradient is imposed varies from 130 s (E) to 430 s (F). Reprinted from [71].

5.3.5 Response to multiple gradients

When confronted by conflicting gradients, unpolarized, immobile cells (e.g. Latrunculin-treated) show elevated levels of signaling activity in the direction of both sources [13], a response that is recreated by the LEGI mechanism on its own [60]. Here we simulated the effect of conflicting gradients on the complete model of the cell. We started with a circular, unstimulated cell, applied two 19% gradients 180° apart and maintained these gradients no matter where the cell moved (Figure 5.7A). At first, the cell sometimes hesitated and, in some cases, even tried to extend pseudopods in both directions (e.g. at 120 s). However, as the cell polarized, one direction won out and the cell migrated in this direction. In contrast, cells that lacked the polarity module oscillated but never settled on either source. Thus, polarization enables cells to select between two competing sources [42, 84]. We also simulated the effect of Latrunculin treatment by setting the cytoskeletal link to the mechanical module to zero irrespective of the EN behavior. The simulated Latrunculin treated cells displayed activity in both directions throughout the period of the simulation (Figure 5.7B). Interestingly, however, the stochastic component in the signaling meant that, while the activity peaks pointed towards both gradients "on average," the relative strengths varied over time. This stochastic behavior was also observed in cells that were stimulated with only one gradient (Figure 5.7C). We also simulated cells that were initially moving in response to an external gradient and to which Latrunculin was added, by gradually reducing the link to the mechanical module. These cells rounded up though they

continued to signal in the direction of the gradient (Figure 5.7D)

5.3.6 Generation of "mutant" behavior by altering model parameters

We next considered the effect of altering the strengths of individual loops in the signaling network. We first reduced the strength of the negative feedback loop in the polarization module by 50%. These cells could sense the gradient, however their signaling response, though still pointing on average in the direction of the chemoattractant gradient, was considerably broader (Figure 5.8A, top and middle cells). This resulted in chemotaxing cells that had multiple simultaneous protrusions which, in many cases, did not point directly towards the source. The cell morphology was quite different from the WT cells, with a broad area facing the gradient. The net movement was also slower. Cells where the negative feedback loop in the excitable network was reduced showed similar patterns of activity [10]. We also investigated the effect of diminishing the strength of the positive feedback loop (through Z) by 50%. The signaling in these cells was aligned with the external gradient. However, the overall level of activity was lower and so the cells moved only slowly in the direction of the gradient (Figure 5.8A).

Lastly, we considered the role of the LEGI mechanism in enabling directional migration. We applied gradients to the cell in which the LEGI inhibitor was not regulated by receptor occupancy but is instead kept constant at the basal level. This prevents the LEGI mechanism from adapting to spatially uniform stimuli, although chemoattractant gradients are still sensed and pass on the directional signal to the ex-

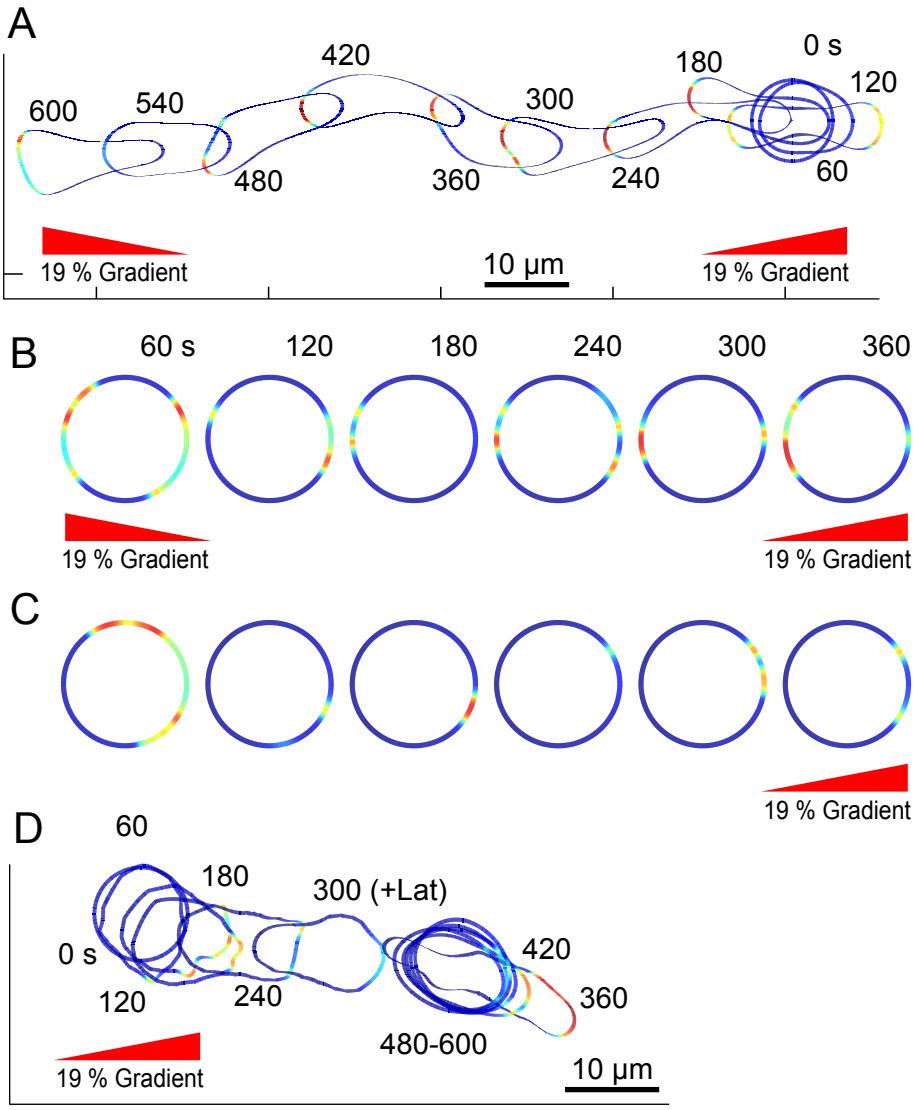

Figure 5.7: Effect of conflicting gradients. (A, B) In these simulations, two 19% gradients were applied 180 degrees apart. Panel A shows the response of a cell with all components; Panel B is that of a cell lacking motility and polarization. (C) Response of an immobile cell to a single 19% gradient. (D) Level set simulation of cell migration under gradient (applied at 0 s) with Latrunculin treatment at 300 s. The total simulation time is 600 s. Reprinted from [71].

citable network. These cells could migrate in the direction of the gradient, though the effectiveness was significantly impaired (Figure 5.8B). When we raised the midpoint of the chemoattractant signal, as might be expected when cells approach a chemoattractant source, the chemotactic efficiency was further impaired compared to WT cells (Figure 5.8C). Comparing the activity of the EN in both situations (Figure 5.8D) shows that the lack of adaptation causes the level of activity to rise throughout the cell perimeter, and this has a negative effect on movement, as multiple pseudopods can occur simultaneously and in the wrong direction. This was not the case for cells with an intact LEGI mechanism, where the inhibitor filters out the mean level of chemoattractant (Figure 5.8D).

In the LEGI without inhibitor model (Figure 5.8B, C), the response regulator is described as follows:

$$\frac{\partial E}{\partial t} = -k_{-E}E + k_E S \tag{5.13}$$

$$\frac{\partial R}{\partial t} = -k_{-R}R + k_R(R_T - R)E. \tag{5.14}$$

5.3.7 Parameter sensitivity analysis

We also carried out parameter sensitivity analysis on several components of the system. Previously, we have demonstrated that the LEGI mechanism is extremely robust to parameter variations. The parameters in the mechanical model were experimentally obtained [56], and tested previously. For this reason we focused our analysis on the polarization module and the excitable network. We had previously

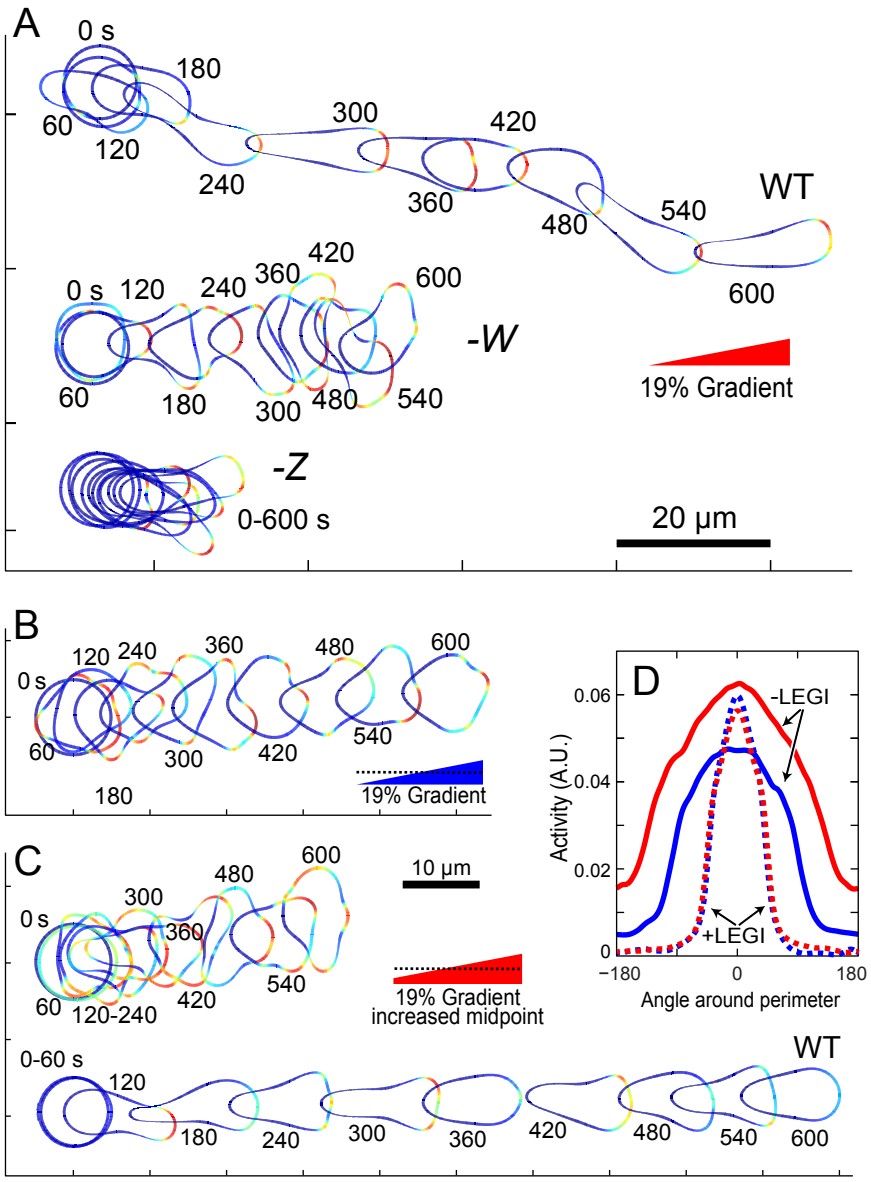

Figure 5.8: Response of cells with altered modules. (A) Response to a chemoattractant gradient of cells with reduction in feedback strengths in W or Z by 50%, compared to WT cells. (B, C) Response of a cell to a gradient in which the LEGI inhibitor is not regulated by receptor occupancy assuming that the midpoint in gradient concentration is changed. The bottom cell in panel C shows the response of a WT cell in response to the increased midpoint concentration. (D) Directional distribution of the responses from panels B (blue) and C (red) with different gradient midpoints. Dotted lines show the corresponding distributions for the model with the LEGI module. Reprinted from [71].

carried out sensitivity analysis on the latter, but because the polarity module acts in feedback with this, we included it in this analysis. This consisted of varying the nominal degradation/production rates and observing the spatial distribution of X and Y, which show similar patterns. Because these drive the mechanical model in open loop, we did not do extensive tests on morphology, being constrained by the computational burden of the level set simulations.

Our results show that small changes ($\pm 20\%$) in the rates controlling X and Y can have quite a strong effect on the excitable behavior (Figure 5.9), as we noted previously [10]. These small differences in the rates of Z and W do not affect the spatial distribution of activity much or the peak levels of activity. To probe the robustness of the polarization module further, we also considered large ($\times 10$ or $\times 1/10$) changes in the parameters of the polarization module (Figure 5.10). Changes of this size on the rates of W change the spatial distributions of Y, but by values smaller than the change in the parameter. For example, increasing the degradation of W ten folds only increased the peak activity level by approximately 60%; decreasing this rate to 1/10th its nominal value decreased the peak level of activity to approximately half. Moreover, the spatial distribution was largely unaffected. Changing the rates of Z had the greatest effect.

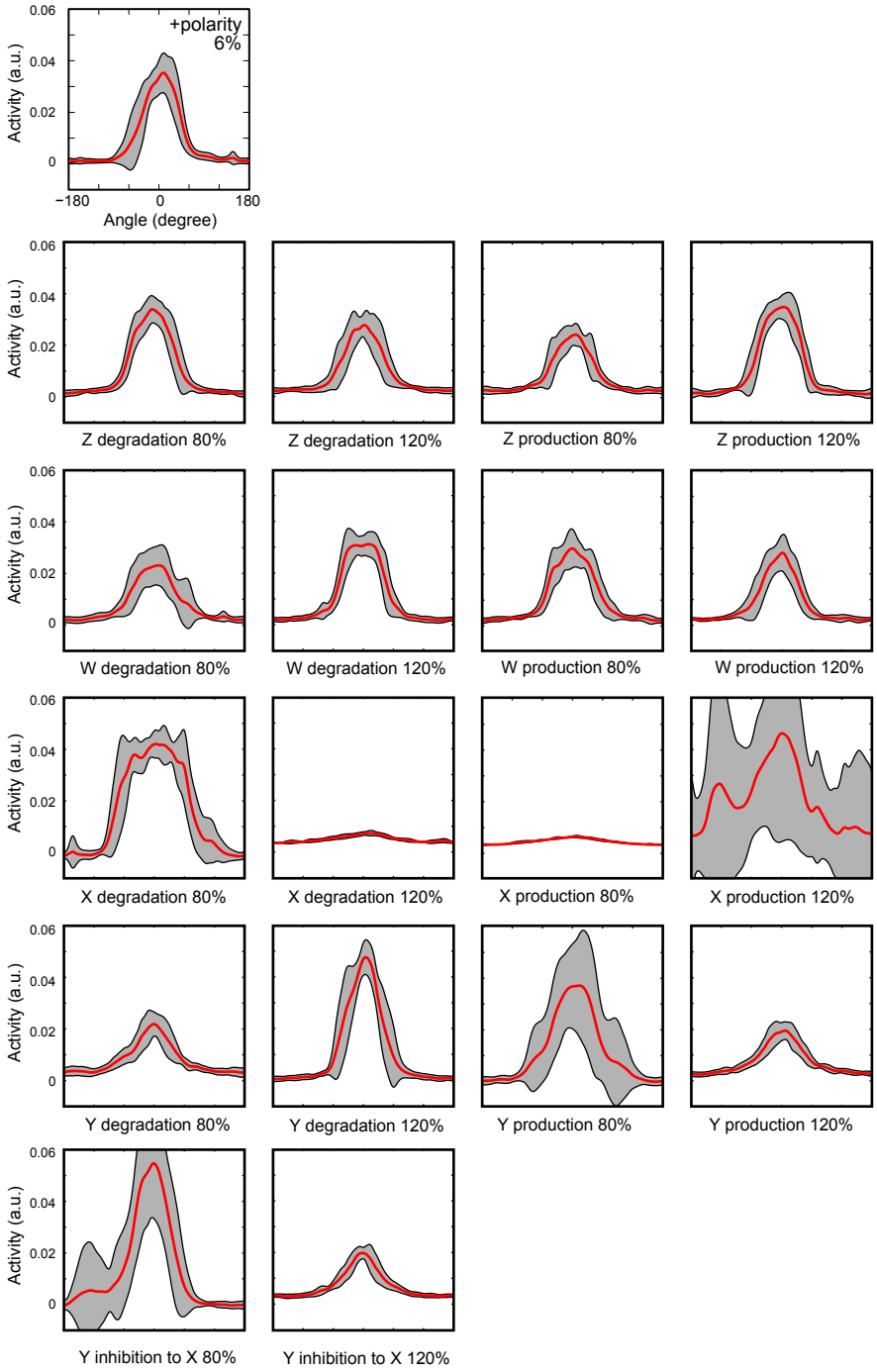

Figure 5.9: Parameter sensitivity. The top one uses the denominated parameters. These plots show the spatial distribution of Y under various parameter perturbations. Red line shows the mean level of activity for twenty, 900 s simulations. The shaded grey area represents one standard deviation. Reprinted from [71].

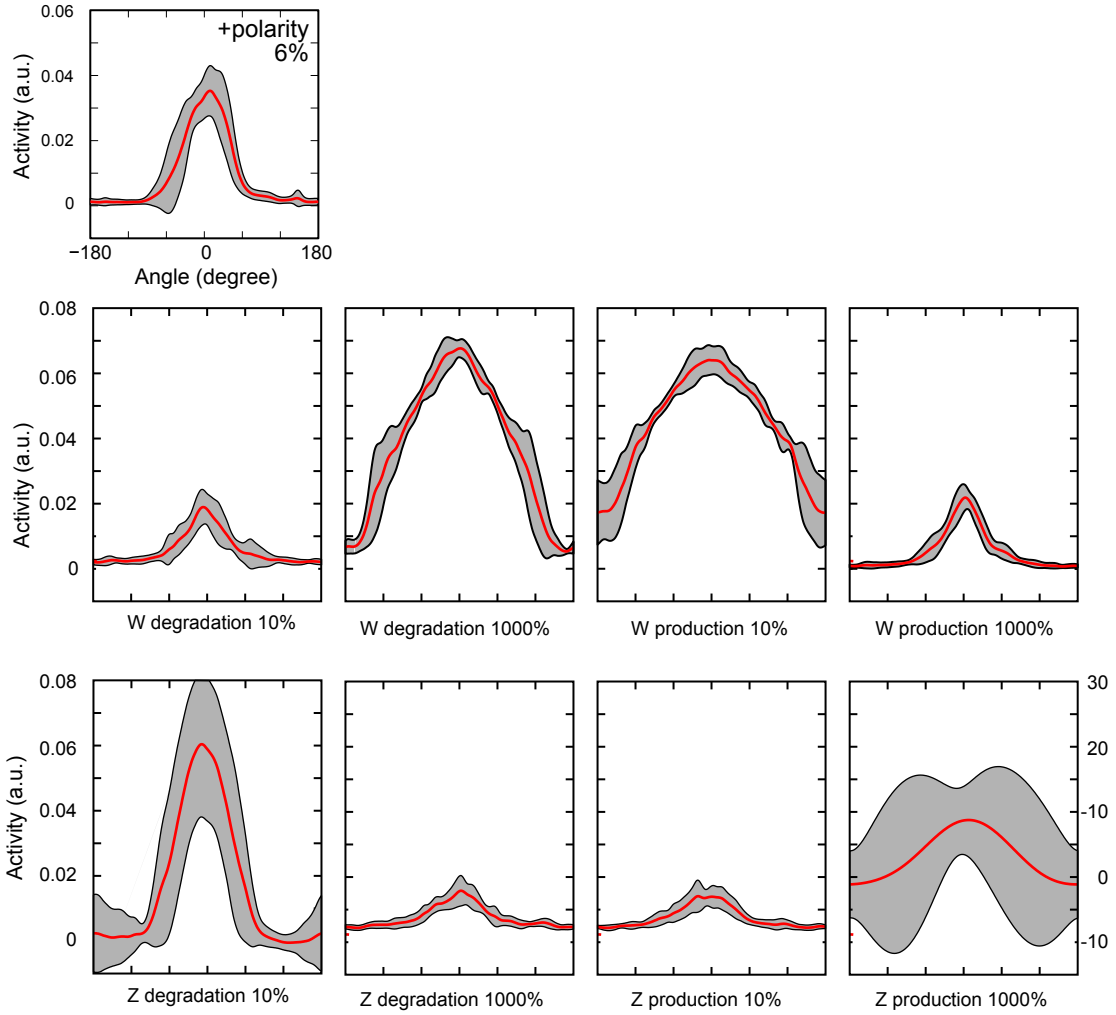

Figure 5.10: Parameter sensitivity for polarization. The top one uses the denominated parameters. These plots show the spatial distribution of Y under various parameter perturbations in the polarization module. Red line shows the mean level of activity for twenty, 900 s simulations. The shaded grey area represents one standard deviation. Reprinted from [71].

5.4 Discussion

5.4.1 Modular framework of the polarized-LEGI-BEN accounts for most experimental observations

None of the current proposed models can account for all the features of chemotactic cells introduced in Chapter 2. As shown in [71], the modular framework of the polarized LEGI-BEN model accommodates all of these behaviors and experimental conditions whereas earlier models only account for various subsets of them.

The overall network topology has similarities with previously published models. Edelstein-Keshet and coworkers have proposed a number of models for cell polarity, motivated by the front-back appearance of Rho GTPases observed in neutrophils. Our model is similar to one of their proposed models (Model 4 in [85]). There, multiple positive feedbacks (or double negative feedback loops, for example Rac⊣Rho⊣Cdc42→Rac, Rac→PIP3→Rac, Rac⊣Rho⊣PIP3→Rac) generate a bistable system. While no direct negative feedback loop is included, each of the GTPases is found in both active and inactive states, and so substrate depletion (the inactive states of the GTPases) can be considered as a negative feedback loop.

The combination of EN and Polarity modules is also comparable to a model proposed by Meinhardt [86] (who did not differentiate between the different processes that comprise chemotaxis) to explain chemotaxis. This model involved a positive feedback loop counterbalanced by two negative feedback loops - one local, the other global. Our combined Polarity-EN (excluding the LEGI mechanism) has two

negative feedback paths, one that is local ($X_{sig}\rightarrow Y_{sig}\dashv X_{sig}$), and the other global ($X_{sig}\rightarrow Y_{sig}\rightarrow W\dashv P\rightarrow X_{sig}$). If we combine the two positive feedback loops of the excitable network ($X_{sig}\rightarrow X_{sig}$) and the polarization model ($X_{sig}\rightarrow Y_{sig}\rightarrow Z\rightarrow P\rightarrow X_{sig}$) then the topology of the models is similar. Neilson et al. carried out level set simulations of the Meinhardt model and generated results similar to ours for polarized cells, including pseudopod splitting, persistent random migration and turns in response to shallow gradients changing direction [87].

Models without a LEGI mechanism, or with only one positive feedback loop, miss out on a number of important aspects of the overall response, however. These models do not adapt when given spatially uniform stimuli and cannot recreate the complex biphasic responses observed. Cells without an adaptation mechanism do not adjust sensitivity when the midpoint of the gradient is raised and hence perform less efficient chemotaxis (Figure 5.8C, D). These simulations, however, show that adaptation is not absolutely required for chemotaxis. In fact, it is known that the response of migrating fibroblasts to uniform PDGF stimulation does not adapt, though these cells can only respond to gradients over a relatively narrow range of chemoattractant concentrations [88], as in our simulations of cells lacking the LEGI mechanism. In models with a single positive feedback loop, the simulated cells are always polarized. In reality, polarized and unpolarized cells can coexist in a population and cells can acquire increased polarity during a period of directed migration.

The ability of the polarized LEGI-BEN to simulate cell movement under a num-

ber of varying scenarios illustrates the relative complexity and sophistication of the chemotactic signaling machinery. Experiments have demonstrated that the pathways governing chemotaxis have considerable redundancy at the biochemical level [1]. Our simulations show a similar redundancy at a systems-level, as they demonstrate that directional migration can be achieved without a LEGI mechanism (Figure 5.8C, D), or without polarity (Figure 4.2B). However, both mechanisms improve efficiency. As argued above, the LEGI mechanism allows the cells to respond to chemoattractant gradients over a wide range of mid-point concentrations. The polarity mechanism enables cells to migrate persistently in the absence of chemoattractant gradients and allows them to use the small directional bias obtained from the gradient to focus most activity towards the source (Figure 5.5B, D).

5.4.2 Experimental assessment of the model

Here we suggest some possible experimental tests of our polarized LEGI-BEN model.

1. One assumption in the model is that the time-scale of adaptation (minutes) is longer than that of the excitable network (20–30 s). This can be tested by exposing cells to chemoattractant for several minutes, thus elevating the level of the global inhibitor in the LEGI module, and then removing the stimulus. Since excitation (E) is predicted to fall more rapidly than the inhibitor (I), the output of the LEGI module will transiently drop below its basal level. During

this period of time, the spontaneous firing of the excitable network as well as its ability to be triggered by external stimulus will be decreased.

2. Currently the major evidence for excitability is observation of propagating waves. Further evidence of excitability could be obtained by testing whether cells generate all-or-none responses to supra-threshold stimuli, and whether they display a refractory period to repeated stimuli. According to our model, these hallmarks of excitable behavior should be largely independent of the actin cytoskeleton.

3. Treatment of cells with inhibitors of the cytoskeleton not only stops motility but also removes the polarity [13]. According to our model, without the mechanical or polarity module, a biased excitable network remains and activity is biased towards the gradient (Figure 5.7C). We have recently found this prediction to be true when observing the dynamics of Ras and PI3K activity in cells treated with latrunculin in a steady gradient.

4. Our model hypothesizes that the persistence observed in unstimulated cells is due to the same mechanism (the polarization module) that leads to polarized cells. One way to test this would be to track, in the absence of chemoattractant stimulus, the persistence of genetically modified cells that show poor polarity (e.g. cells lacking tsunami [89] or dynacortin [90]).

5.5 Summary

This chapter has described a mathematical model which is composed with several separable but interconnected modules: motility, gradient sensing and polarity. These modules are represented with reaction-diffusion equations. Migration and the accompanying changes in cellular morphology are demonstrated in simulations using a mechanical model of the cell cortex implemented with the level set framework. The central module is an excitable network that accounts for random migration. The response to combinations of uniform stimuli and gradients is mediated by a local excitation, global inhibition module that biases the direction in which excitability is directed. A polarization module linked to the excitable network through the cytoskeleton allows unstimulated cells to move persistently and, for cells in gradients, to gradually acquire distinct sensitivity between front and back. Coupling all modules together, we can recreate a complete set of various behaviors observed in chemotaxis cell, while other models fail to do so. This modular view not only demonstrates the internal structure of each module but also how cell coordinate different modules to realize its cellular functions.

When the direction of a shallow gradient is changed, polarized cells slow turn in the direction of the new gradient. In contrast, the turn is more abrupt in steep gradients [15]. Chemotaxis may represent another situation in which persistence could be critical, because cells moving without persistence need a chemotaxis bias for each new pseudopod, while cells moving persistently will accumulate directional accuracy

at each subsequent pseudopod. In the LSM simulation under gradient (Figure 4.2B), the cell generates pseudopod in opposite direction after gradient is shifted without making any turn.

Chapter 6

A Cytoskeletal Oscillating Network

Excitable behavior was first observed in the several cytoskeleton proteins [19, 21–23]. Observations by total internal reflection fluorescence microscopy (TIRFM) revealed propagating waves of recruitment of actin-binding proteins and suppressor of cAMP receptor (SCAR) subunits to the cell cortex. This recruitment could be influenced by chemoattractant stimulus. More recently, observations of Ras and PIP3 waves have demonstrated that excitability is also found in the signaling network that is upstream of the cytoskeleton [10]. These observations also suggest that many, if not all, components of the signaling network display similar excitable behavior which can be perturbed in a defined manner by chemoattractants. Thus, a single excitable network was introduced to account for this excitability (Chapter 2 and [10]).

Recently, however, a new experimental technique has allowed us to have a better look at these excitable activities and suggest a new scheme in which the signaling

network and the actin cytoskeleton behave differently [91]. These findings require modifications to the current excitable network (EN) model. This new model scheme is the focus of this chapter. Before describing the modifications of the model, however, we summarize their findings so as to motivate the new model.

6.1 An excitable signal integrator couples to an idling cytoskeletal oscillator

Our collaborators, Chuan-Hsiang Huang and Peter Devreotes, developed a new technique, in which all the frames of a TIRF time-lapse video are stacked to create a three-dimensional kymograph (Figure 6.1A, B) [91]. This technique, which they called *t*-stack, facilitates the analysis of the spatiotemporal evolution of signaling events. The *t*-stack can be rotated to view the lateral surface, which represents the dynamic activity near the edge of the basal surface of the cell. *t*-stacks reveal features of the dynamic activities of biosensors that are not readily apparent by observation of the videos. This technique was then used to investigate excitable behavior in chemotaxis cells.

6.1.1 The fast oscillatory cytoskeletal network

We first focused on the cytoskeletal network. The dynamic behavior of cytoskeletal events can be observed using the SCAR/WAVE component HSPC300 and an actin polymerization sensor, LimEΔcoil, hereafter abbreviated as LimE. *t*-stacks of cells expressing either HSPC300-GFP or LimE-RFP unexpectedly revealed rapid os-

cillatory activity at convex, non-expanding points around the perimeter of the basal surface of the cell (Figure 6.1C, D). These oscillations had a period of approximately 10 s, which was much shorter than the typical interval between pseudopods.

The cytoskeletal activities exhibited a number of features. First, within the same cell, the oscillations at different spots were not in phase with each other, nor did they have identical frequencies (Figure 6.1E). Second, oscillations could also be found in cells lacking the G-protein β-subunit, in cells lacking the PIP3 phosphatase PTEN, in cells treated with the PI3K inhibitor LY294002, and in cells expressing constitutively active RasC. These results suggested that these rapid cytoskeletal oscillations do not require signal transduction events but did need actin polymerization, which is preceded by the nucleation promoting activity of the SCAR/WAVE complex. Third, t-stacks from interior regions of cells showed transient non-oscillatory activities of LimE across the cell bottom. We refer to this as the *cytoskeletal oscillatory network* (CON).

6.1.2 The slow excitable signal transduction network

In contrast to the cytoskeletal events, the activities of signal transduction markers, which propagated in expanding waves across the basal surface of the surface, were broader and lasted longer. The progression of a wave is clearly seen by the profiles of temporal changes in intensity (Figure 6.2A). The propagating waves of fluorescent-tagged RBD or PH-domain suggest that the signal transduction network is excitable. Whereas Latrunculin at 1 μM blocked cytoskeletal oscillations, the propagating waves

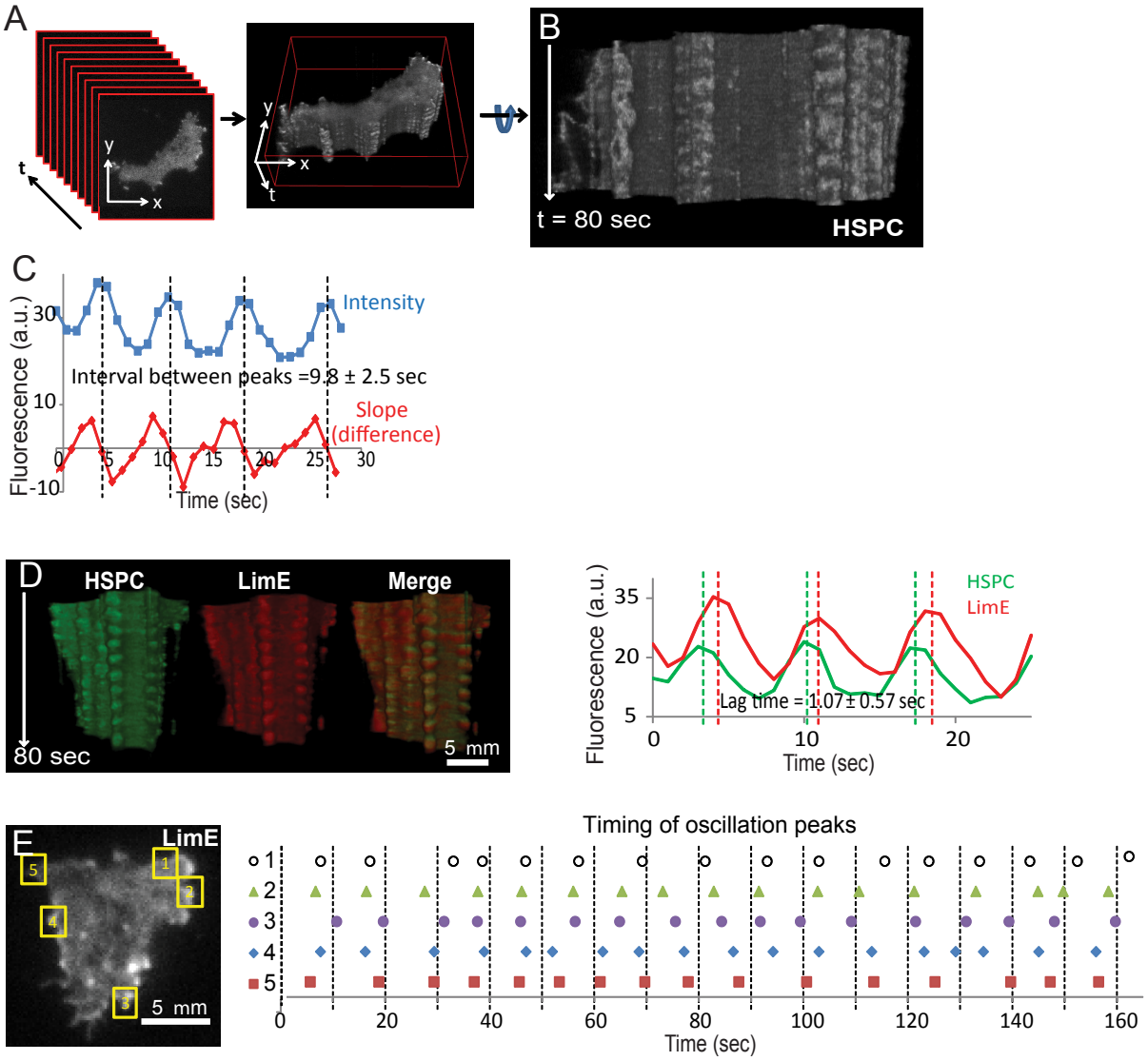

Figure 6.1: Fast oscillations of the cytoskeletal activities revealed by t-stacking. (A, B) A t-stack generated by stacking frames of a TIRF video of a cell expressing HSPC300-GFP. (C) Intensity plot (blue) and plot of difference between successive points (red) of an oscillatory region. Peaks of the intensity plot were interpolated from the zero points of the difference plot (dashed lines). The means±s.d. of intervals between peaks ($n = 178$ cycles from 16 cells) is shown. (D) t-stacks from a cell co-expressing HSPC300-GFP and LimE-RFP (top), and the corresponding intensity plots along an oscillatory region on the periphery (bottom). Dashed lines mark the interpolated peaks. The mean±s.d. of lags between the peaks of HSPC300 and LimE intensity ($n = 117$ cycles from 16 cells) is shown. Frame rate: 1 spf. (E) Timing of peaks of LimE intensity in five oscillatory regions (1-5) within the same cell. Reprinted from [91].

of RBD and PH persisted at 5 μM, although Latrunculin treatment did reduce the frequency of new PH patches (Figure 6.2B), suggesting that the cytoskeletal activities may promote the initiation of signaling events.

The RBD and PH activities were nearly co-localized (Figure 6.2C), but the t-stacks of RBD and PH activities were smooth, indicating the absence of fast oscillations (Figure 6.2D). These evidences suggest that Ras, PIP3 and other signaling network components are in excitable state and are in a different module with cytoskeleton network. We call this network the *signal transduction excitable network* (STEN).

6.1.3 A STEN-CON coupling model of cell migration

Examination of the cortical recruitment of co-expressed LimE-RFP and RBD-GFP showed RBD and LimE signals were both elevated in large expanding regions (brackets), whereas LimE oscillations unaccompanied by RBD were present in non-expanding regions (vertical rectangles) (Figure 6.3A, B). Closer examination revealed LimE oscillations were correlated with the small amplitude undulations of the cell boundary and signal transduction events drive the expansion of cytoskeletal activities in protrusions. Although LimE and RBD activities were both elevated in the expanding regions, their localizations were not identical, with LimE restricted to a thin region near the edge and RBD distributed over a substantial area of the protrusion. Moreover, LimE recruitment occurred in bursts, whereas RBD exhibited a smoother change over the entire event.

Taken together, these new findings suggest that the signaling and cytoskeletal

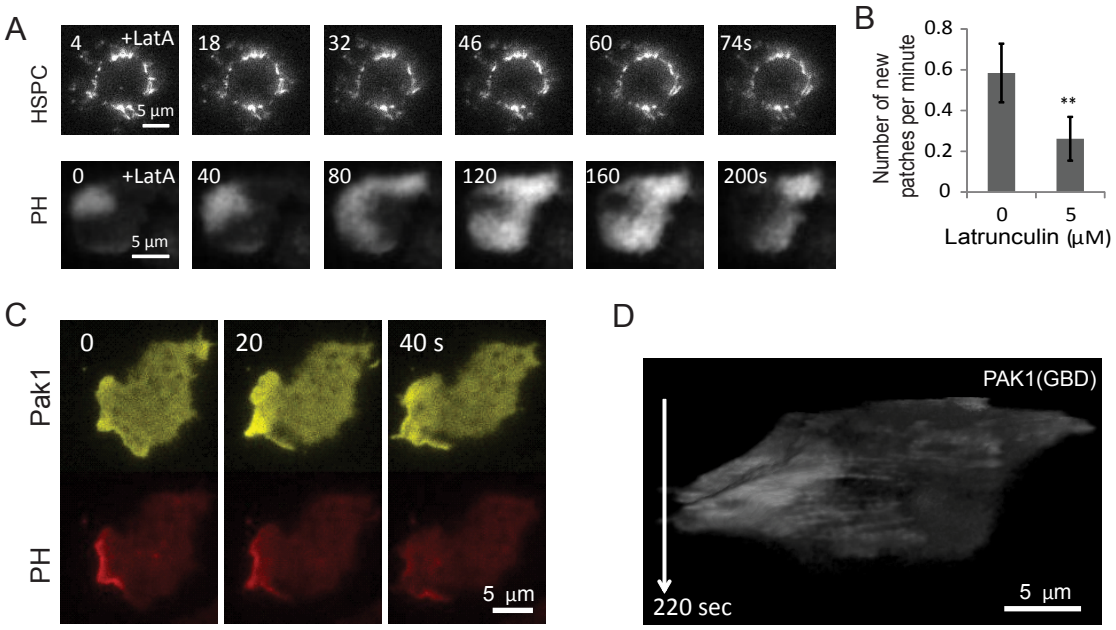

Figure 6.2: The slow, excitable signaling network. (A) Frames from time-lapse TIRF videos of HPSC300-GFP in a cell in 1 μM Latrunculin (upper), and PH-GFP in a cell in 5 μM Latrunculin (lower). (B) (c) The effect of Latrunculin on the frequency of new PH-GFP patches (mean$\pm$s.d., $n = 18$ and 28 cells, $P < 0.001$, Student's t-test). (C) Rac activity correlates with the dynamics of the signaling network. Frames from a time-lapse TIRF video of a cell co-expressing PAK1(GBD)-YFP and PH-RFP. (D) t-stack of a cell expressing the Rac biosensor PAK1(GBD)-YFP showing the absence of fast oscillations. Reprinted from [91].

events belong to two different networks with distinct characteristics, which are designated as the signal transduction excitable network (STEN) and the cytoskeletal oscillatory network (CON), and that cell migration depends on STEN-CON coupling (Figure 6.4A, B). In this coupling model for cell migration, shown schematically in Figure 6.4A , the CON provides the "idling" motor force, which by itself drives only small-amplitude undulations. In large protrusions, the CON is engaged by the activity of the STEN, which acts as the "pacemaker" for cell migration. As a wave of signal transduction activity propagates, it prevents the retraction of expanded areas during the down phase of the cytoskeletal oscillation or completely shifts existing or newly initiated cytoskeletal activities beyond the oscillatory mode to a continuously active state. In either case, the coupling of STEN and CON leads to a widening protrusion. The STEN will fire when the threshold is crossed, whether owing to internal noise or feedback from the CON. The STEN can also be modulated by a variety of external stimuli and perturbations

6.2 The STEN-CON coupling model

The new findings suggest that the signaling and cytoskeletal events belong to two different networks with distinct characteristics, which are designated as the signal transduction excitable network (STEN) and the cytoskeletal oscillatory network (CON). These two networks are separable but also interconnected. They cooperate together biologically to direct cell migration. Thus, a single excitable network, as in

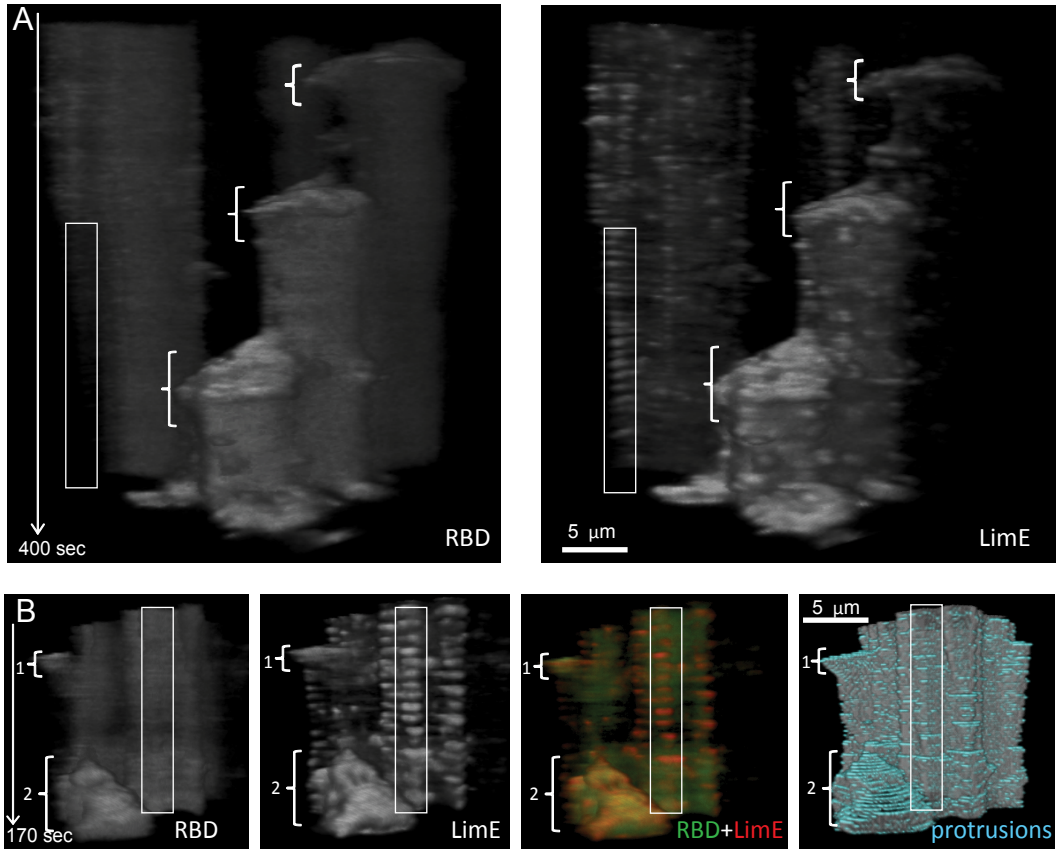

Figure 6.3: Coupling of signal transduction and cytoskeletal networks in protrusions. (A) *t*-stacks from two cells co-expressing RBD-GFP (left) and LimE-RFP (right). In each panel, the cell on the right extends three large protrusions (brackets) during the imaging period. The outlined area on the non-extending cell on the left shows oscillations in LimE-RFP without apparent oscillations in RBD-GFP. (B) *t*-stacks from another cell co-expressing RBD-GFP and LimE-RFP and used for quantitative analysis. The brackets point to two protrusions with high RBD and LimE, which appear yellow in the merged *t*-stack (third panel). The "protrusion" *t*-stack shows regions of cell boundary increases in blue (fourth panel). Reprinted from [91].

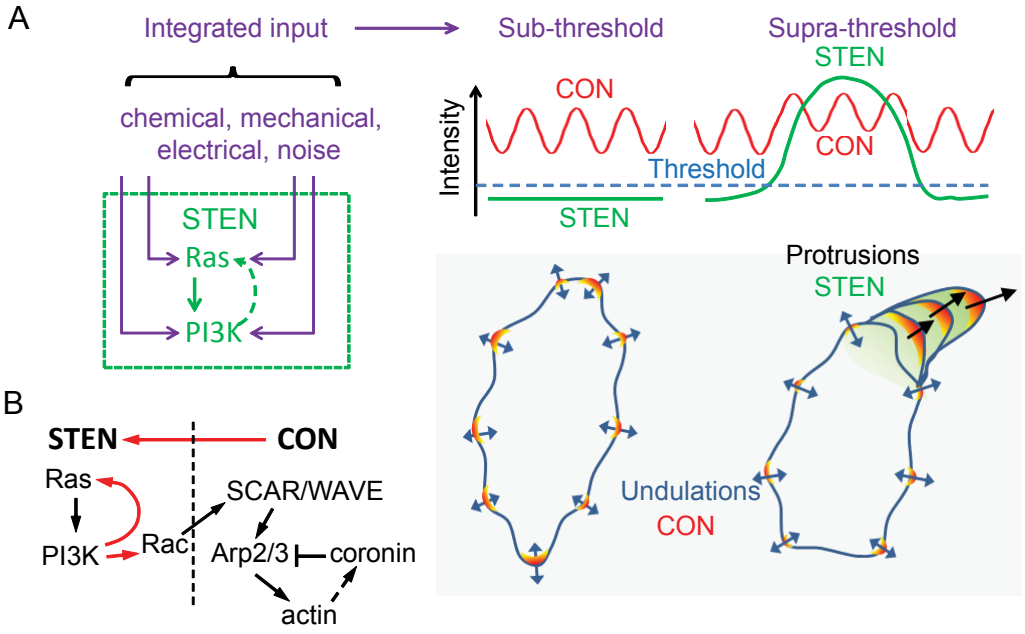

Figure 6.4: The STEN-CON coupling model. (A) In the STEN-CON coupling model, inputs from various sources enter STEN at different points. When the integrated input reaches a threshold level, STEN becomes fully activated and by coupling to CON causes large protrusions. Without STEN activation, the cytoskeletal oscillations cause only small-amplitude undulations of the cell boundary. (B) Schematic of the links between components of the STEN and CON. Red arrows highlight the links demonstrated in this study. Reprinted from [91].

the model described in Chapter 4, is not sufficient to describe the complete system. Therefore, we dissect the excitable network (EN) into two interconnected subsystems, describing STEN and CON, respectively (Figure 6.5A).

6.2.1 Signal-Transduction Excitable Network (STEN)

The STEN is similar to the previously described EN. It has two species (Figure 6.5B). Component X_{sig} acts as the activator: it is autocatalytic and also activates the downstream component-we refer to this as the feedforward loop. The Y_{sig} component provides negative feedback to X_{sig}. In the absence of stimulus, phase-plane analysis shows the STEN system has a single steady state that is stable (Figure 6.5C). The solid black circle represents the unique, stable equilibrium, found at the intersection of the two nullclines. The blue arrows represent the system evolution at different points in the phase plane. Two different trajectories are denoted by the black lines. The dotted black line represents a sub-threshold perturbation from which the system returns quickly to the equilibrium. The solid black line illustrates a super-threshold perturbation that causes the system to undergo a large excursion before returning to the equilibrium.

The mathematical expressions of the STEN are the same as those of the excitable network:

$$\frac{\partial X_{sig}}{\partial t} = \alpha_{sig}\frac{X_{sig}^2}{k_{sig}^2 + X_{sig}^2} - \beta_{sig}X_{sig} - \gamma_{sig}Y_{sig} + \rho_{sig}U_{sig} + D_{X_{sig}}\nabla^2 X_{sig} \tag{6.1}$$

$$\frac{\partial Y_{sig}}{\partial t} = \delta_{sig}X_{sig} - \epsilon_{sig}Y_{sig} + D_{Y_{sig}}\nabla^2 Y_{sig}. \tag{6.2}$$

The difference between this system and that describes earlier is in the input: U_{sig}, since there is feedback from CON to STEN. U_{sig} consists of a basal level of activation B_{sig} and the contribution from the fast system ($f(X_{con})$, described below):

$$U_{sig} = B_{sig} + f(X_{con}). \tag{6.3}$$

Note that in contrast to the biased-excitable network described previously, here we do not incorporate the contribution of receptor signaling. Were this to be included, it would be as an additional term in U_{sig}. We also do not incorporate a stochastic component directly into the slow system, but instead achieve this through the faster system. However, such a stochastic component could explain the signaling patches observed in Latrunculin-treated cells.

6.2.2 Cytoskeletal Oscillatory Network (CON)

The CON can also be described as an activator (X_{con})-inhibitor (Y_{con}) system (Figure 6.5D). In fact, the form of the equations used to described the CON is identical to those of the STEN system:

$$\frac{\partial X_{con}}{\partial t} = \alpha_{con}\frac{X_{con}^2}{k_{con}^2 + X_{con}^2} - \beta_{con}X_{con} - \gamma_{con}Y_{con} + \rho_{con}U_{con} + D_{X_{con}}\nabla^2 X_{con} \tag{6.4}$$

$$\frac{\partial Y_{con}}{\partial t} = \delta_{con}X_{con} - \epsilon_{con}Y_{con} + D_{Y_{con}}\nabla^2 Y_{con}. \tag{6.5}$$

However, this system is now required to represent an oscillatory pattern of activity with period of approximately 10 s. Systems involving cubic nullclines such as those described Figure 6.5E can be oscillatory, as in the popular relay oscillator. In our

system, however, we chose the coefficients so that, in the absence of noise or a contribution from the slow network ($N_{con} = 0$, $g(X_{sig}) = 0$), the system has three steady states, two of which are stable and the other unstable. These two stable steady states are such that small, but superthreshold perturbations, make the system switch from one equilibrium to the other, resulting in oscillatory-like behavior. In this case, noise endows the system with oscillatory behavior. The phase-plane is shown in Figure 6.5E. Red and green lines are nullclines for the activator and inhibitor components, respectively. Thus, the system behaves as a stochastic, bistable oscillator. In this case the system has three equilibria, at the points where the nullclines intersect. The solid black circles denote two stable equilibria, the open black circle the unique, unstable equilibrium. The blue arrows represent the evolution at different points in the phase plane. Trajectories are denoted by the black lines.

The input to this system (U_{con}) consists of three parts:

$$U_{con} = B_{con} + N_{con} + g(X_{sig}). \tag{6.6}$$

Note that the STEN and CON systems are interconnected. STEN directs CON by interrupting and synchronizing oscillations. STEN receives not only upstream signal (e.g. LEGI) but also feedback from the CON.

6.2.3 STEN-CON Coupling

The two systems are coupled in a bidirectional manner. However, because the only external input to the coupled system is through the external stochastic component

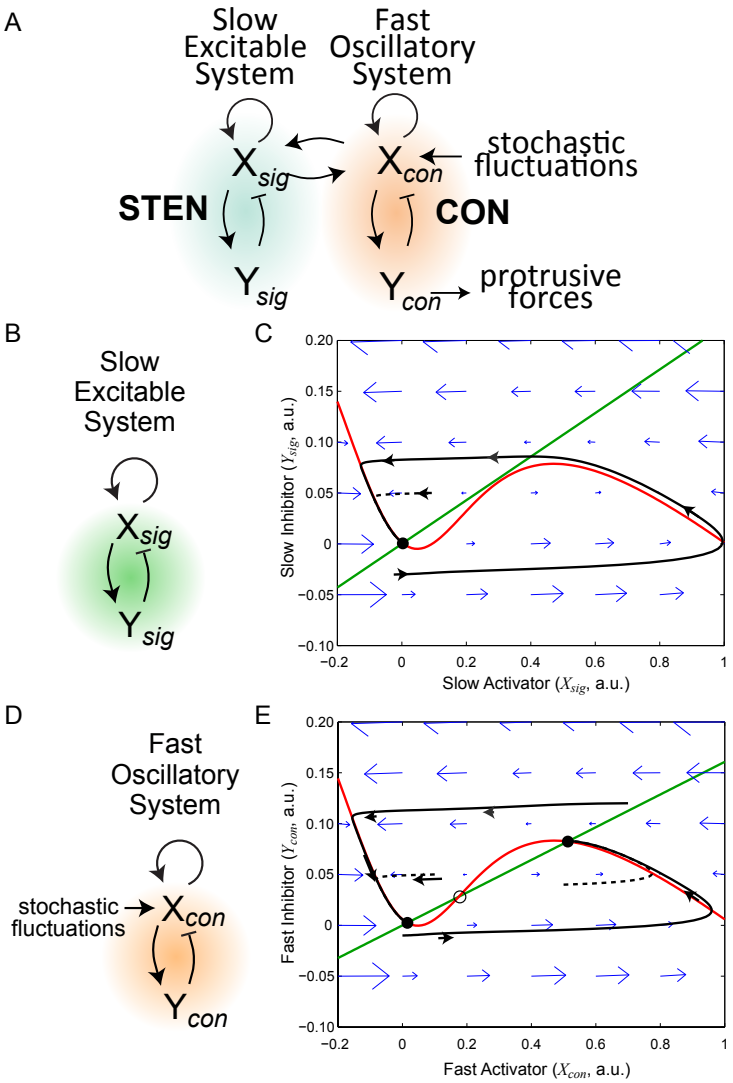

Figure 6.5: Model of coupled STEN-CON System. (A)The behaviors of the STEN and the CON were modelled using reaction-diffusion equations describing slow (X_{sig}, Y_{sig}) and fast (X_{con}, Y_{con}) activator-inhibitor systems solved in one dimension around a circle. (B) The slow excitable system is implemented as an activator (X_{sig})-inhibitor (Y_{sig}) system. (C) Phase-plane plot of the slow excitable system. Red and green lines are nullclines for the activator and inhibitor components, respectively. (D) The Fast oscillatory system is also implemented using an activator (X_{con})-inhibitor (Y_{con}) system and also incorporates the influence of stochastic perturbations. (E) Phase-plane plot of the fast oscillatory system. Reprinted from [91].

of the fast system, perturbations from the respective equilibria have to be initiated through the fast system.

The function $f(X_{con})$ in Equation 6.7 is used as a trigger to the slow system based on the activity of the fast system. First, at each angle $\theta_0 \in (-\pi, \pi]$ along the perimeter of the cell, the activity of the fast system in the neighborhood of θ_0 is summed:

$$\tilde{X}_{con}(\theta_0) = \int_{\theta_0-\Delta\theta}^{\theta_0+\Delta\theta} X_{con}(\theta) d\theta.$$

We used a width of $\Delta\theta = 15°$. This is used to generate a switch-like function:

$$h(X_{con}(\theta)) = \begin{cases} 0, & \text{if } \tilde{X}_{con}(\theta) < \tilde{X}_{con-th} \\ 1, & \text{otherwise.} \end{cases}$$

The coupling term $f(X_{con})$ is obtained by multiplying this function by a white-noise component:

$$f(X_{con}(\theta)) = h(X_{con}(\theta))\tilde{N}_{con}, \tag{6.7}$$

which represents a probabilistic component of the activation. Here $\tilde{N}_{con}$ is a white noise process with unit variance and a mean of 0.05.

After the slow system is triggered, the high activity of X_{sig} starts to regulate and synchronize the fast system. During the time that the slow system fires up, high input from $g(X_{sig})$ drives the fast system into a higher stable steady state. After $g(X_{sig})$ vanishes, the fast system resumes an oscillatory mode. The function of $g(X_{sig})$ is

simply described with an "on-off" switch function:

$$h(X_{con}(\theta)) = \begin{cases} g_B, & \text{if } X_{sig}(\theta) < X_{sig-th} \\ g_s, & \text{otherwise.} \end{cases}$$

6.2.4 Parameters

The model includes a number of parameters. Our starting point for choosing these was the previous model of the biased excitable network [10]. However, we adjusted these parameters so that the activity of the slow system spreads out to about 50 degrees around the perimeter and that the activities last about 100 s, to match the observed experimental behavior of the STEN. These changes were made by reducing the parameters that dictate the speed of the system and by altering the relative contribution of the two diffusion coefficients. For the fast system we chose the parameters so that the system had two stable equilibria (by changing the slope of the Y_{con} nullcline). We also adjusted the speed of the system so that the oscillations lasted about ten seconds. This is accomplished by adjusting the level of the noise. The final parameter values are given in Table 6.1.

6.2.5 Model implementation

The model and all simulations were implemented using Matlab. The cell boundary was represented as a one-dimensional system using periodic boundaries and discretized using 360 points. Spatial diffusion terms, which contain the second derivatives, were approximated by central differences in space (in one dimension); and by

Table 6.1: STEN-CON model parameters

STEN					
$D_{X_{sig}}$	0.0059 μm^2/s	$D_{Y_{sig}}$	0.0151 μm^2/s	α_{sig}	0.7 s^{-1}
β_{sig}	0.63 s^{-1}	γ_{sig}	2.35 s^{-1}	δ_{sig}	0.0051 s^{-1}
ϵ_{sig}	0.024 s^{-1}	k_{sig}	0.32 A.U.	B_{sig}	-0.0138 A.U.
ρ_{sig}	1 s^{-1}				
CON					
$D_{X_{con}}$	0.091 μm^2/s	$D_{Y_{con}}$	0.0236 μm^2/s	α_{con}	0.19 s^{-1}
β_{con}	0.18 s^{-1}	γ_{con}	0.65 s^{-1}	δ_{con}	0.0011 s^{-1}
ϵ_{con}	0.0067 s^{-1}	k_{con}	0.32 A.U.	B_{con}	0.1 A.U.
ρ_{con}	1 s^{-1}				
Coupling					
X_{con-th}	7 A.U.	X_{sig-th}	0 A.U.		
g_B	1.25 A.U.	g_{sig}	1.3 A.U.		

doing that, the partial differential equations were converted to ordinary differential equations. The solution of the stochastic differential equations was obtained using the free SDE toolbox for Matlab [81]. The time step for the simulation was set to 0.025 s.

To determine the effect of the model activities on the shape of a cell we used a level set framework to simulate cell shape changes as previously described (Chapter

4) with one modification: the volume conservation was not implemented, since we wanted to compare our simulations with TIRFM images, which represent the basal surface of the cell. The latter can change in size depending on the cell-substrate contact area.

6.3 Results

We first carried out simulations for unstimulated cells. In a kymograph, the STEN system displayed random patches representing excitable activities which were only activated when CON activities were above a given threshold (Figure 6.6A). At the same time, the CON system displayed oscillatory behavior around the cell membrane (Figure 6.6B). The oscillations had a period of about 10 s.

We also recapitulated different modes of the CON with or without STEN activity. We observed oscillations in the absence of activity of the STEN (region 1 in Figure 6.6A, B), and the broadening of the CON activities accompanied by the activation of the STEN while preserving the characteristic time constants (region 2 in Figure 6.6A, B). This broadening and synchronization represents STEN's regulation on CON.

We further used the activity of the coupled systems to drive the movement of the boundary of a cell and simulated realistic behavior using level set method. Using the boundary to represent the edge of the basal cellular surface we produced t-stacks resembling those derived from TIRFM videos of real cells (Figure 6.6C). Our results

recreated the experimental observations.

6.4 Summary

The STEN-CON coupling model provides a framework for understanding cell migration. The "idling" activity of the CON provides the force, but it is the "pacemaker" activity of the STEN that determines the timing and size of protrusions in migrating cells. We have developed a mathematical framework to model these two separable and interconnected modules. Our simulations successfully recreated the experimental observations.

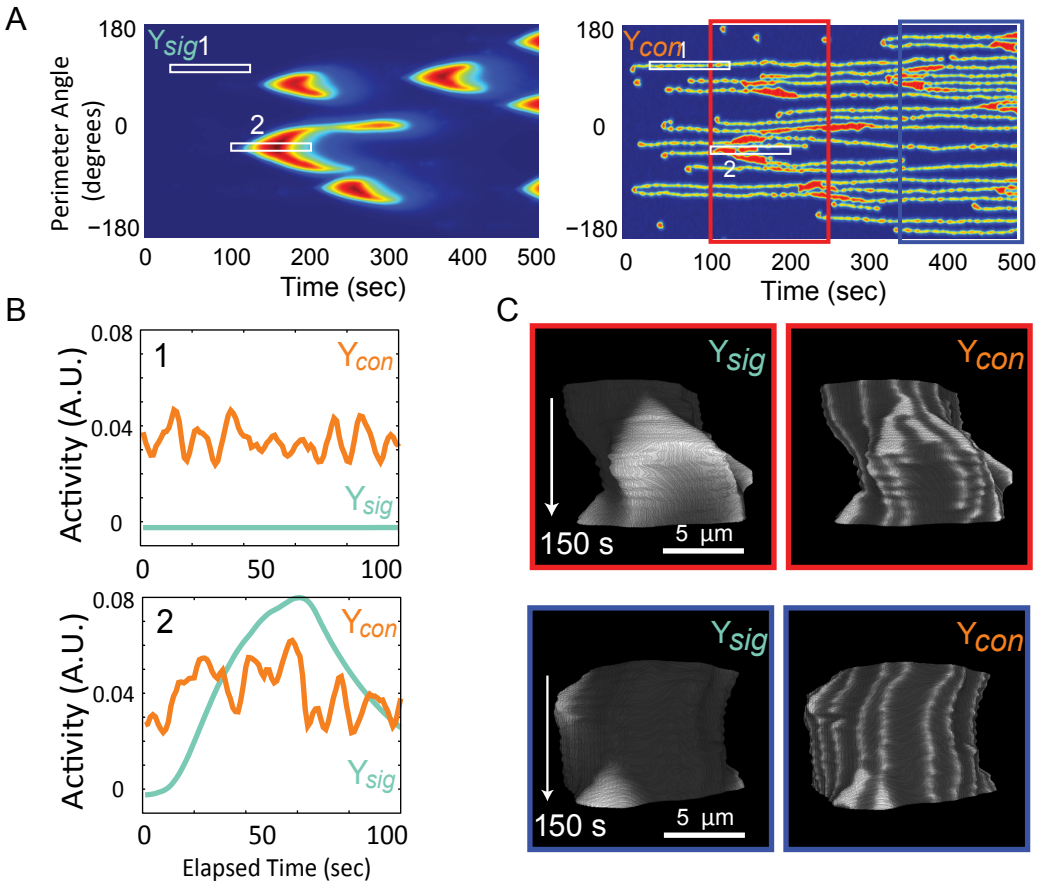

Figure 6.6: Simulation of STEN-CON coupling. (A) Kymograph describing the activities of the slow (Y_{sig}) and fast (Y_{con}) systems around the perimeter of the circle using a jet color map. (B) Intensity plots of the slow and fast systems corresponding to rectangles 1 and 2 in A. (C) The activities of the slow and fast systems were used to control the boundary of a hypothetical cell. t-stacks of the activities of Y_{sig} and Y_{con} on the boundary of the hypothetical cell with a grey color map corresponding to the period from 100 to 250 s (red rectangle) and 350 to 500 s (blue rectangle) in A are shown. Reprinted from [91].

Chapter 7

A Modular View of Chemotaxis

Previous chapters argued the suitability of a modular view for studying the chemotaxis. This modular view originates from the fact that the chemotactic system itself displays separable activities, in gradient sensing, motility and polarity. This modular approach is particularly useful to study complex system when there is only partial understanding of the network. With the development of new techniques and new discoveries, we can both improve our understanding, not only by updating existing models, but also by adding new modules without altering the overall behavior of the other modules.

To date, we have introduced a number modules: the local excitation, global inhibition (LEGI) mechanism, the signaling transduction excitable network (STEN), the cytoskeletal oscillatory network (CON), and the polarity mechanism (POL). These are all conceptual modules. We have not assigned biochemical entities to specific

model components or modules. This abstract settings allows us to understand the underlying core functional mechanism despite the complex signaling pathways.

This chapter will develop a complete model by assembling LEGI, STEN, CON and POL modules.

7.1 A complete scheme

The complete model is described in Figure 7.1. Chemotactic cells employ a LEGI mechanism to perceive chemoattractant signals through receptor and subsequently bias downstream signaling events. The LEGI mechanism's core functionalities are adaptation and gradient sensing. The STEN is the central module in this scheme. The STEN displays excitability and can amplify the gradient sensed from LEGI to generate more distinct front-back regions so as to guide cell migration. The intrinsic cellular polarity feeds to the STEN to interact with external signal. CON provides cell with "idling" motor force and also promotes intrinsic polarity. POL works as a bias to maintain cell polarization. Our modular constructions are based on biological observations.

7.1.1 Mathematical description

All the modules have been described in detail in previous chapters. I will only describe the linkage between the modules.

The input to STEN is denoted by U_{sig}, which consists of output of LEGI (R), intrinsic polarity ($Z - W$):

$$U_{sig} = B + N + \lambda(R - R_{init}) + \varphi(Z - W). \tag{7.1}$$

where, B is a basal level of activity and N is the white noise. The regulation of STEN to CON is described by a 'on-off' switch function:

$$h(X_{con}(\theta)) = \begin{cases} g_B, & \text{if } X_{sig}(\theta) < X_{sig-th} \\ g_s, & \text{otherwise.} \end{cases} \tag{7.2}$$

The CTON activates the POL module by a switch function:

$$h(X_{pol}(\theta)) = \begin{cases} P_B, & \text{if } X_{con}(\theta) < X_{con-th} \\ P_s, & \text{otherwise.} \end{cases} \tag{7.3}$$

The parameters are shown in Table 7.1

7.2 Results

Simulations were carried out on a circular periodic boundary discretized by 360 points, using Matlab as previously described. The time step was 0.025 s.

7.2.1 In absence of stimulus

Without stimulus, localized patches of activity in STEN appear randomly. As seen in the kymograph of a cell in the absence of stimulation, it is clear that patches of activity can appear simultaneously, either far from each other (Figure 7.2) or sufficiently close to give the appearance of a single, wider crescent. Among these random activities,some are more persistent than others because of the contribution from the

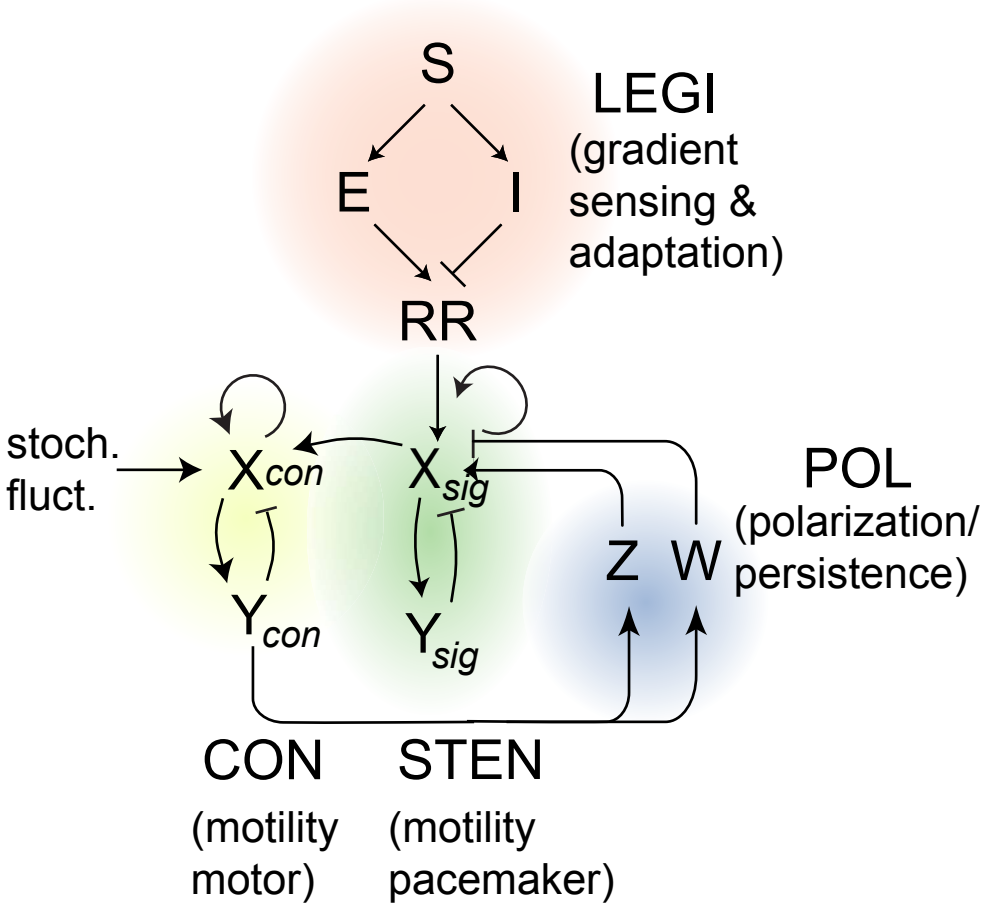

Figure 7.1: A complete scheme of chemotaxis. In this scheme, there are four modules: LEGI, STEN, CON and POL. LEGI perceives chemoattractant signals through receptor and biases the STEN excitable activities. STEN amplifies signal from LEGI and directs cytoskeletal activities. CON oscillates at cell boundary and provides "idling" motor force. POL is intrinsic cell polarity.

Table 7.1: Coupling of modules

STEN input			
B	−0.063 A.U.	R_{init}	1.25 A.U.
λ	2	φ	2
STEN to CON			
X_{sig-th}	0.3 A.U.		
g_B	1.29 A.U.	g_s	1.25 A.U.
CON to POL			
X_{con-th}	0.07 A.U.		
P_B	1 A.U.	P_s	0 A.U.

POL module. These persistent activities can last several hundred seconds before the cell resumes seemingly random firings. The CON responses display oscillatory behaviors at the cell boundary. Wherever the STEN fires, the CON oscillations are synchronized and increase in size. These wider activities propel the cell. The CON also activates the POL network wherever STEN fires, leading to persistent activity

7.2.2 Uniform stimulus

A uniform stimulus applied at 300 s gave rise to a burst of activity that covered nearly the entire perimeter of the cell (Figure 7.3). This response subsided rapidly by 30 s due to the negative feedback loop within the STEN. Eventually, the system adapted and the spontaneous activity returned completely to the prestimulus level,

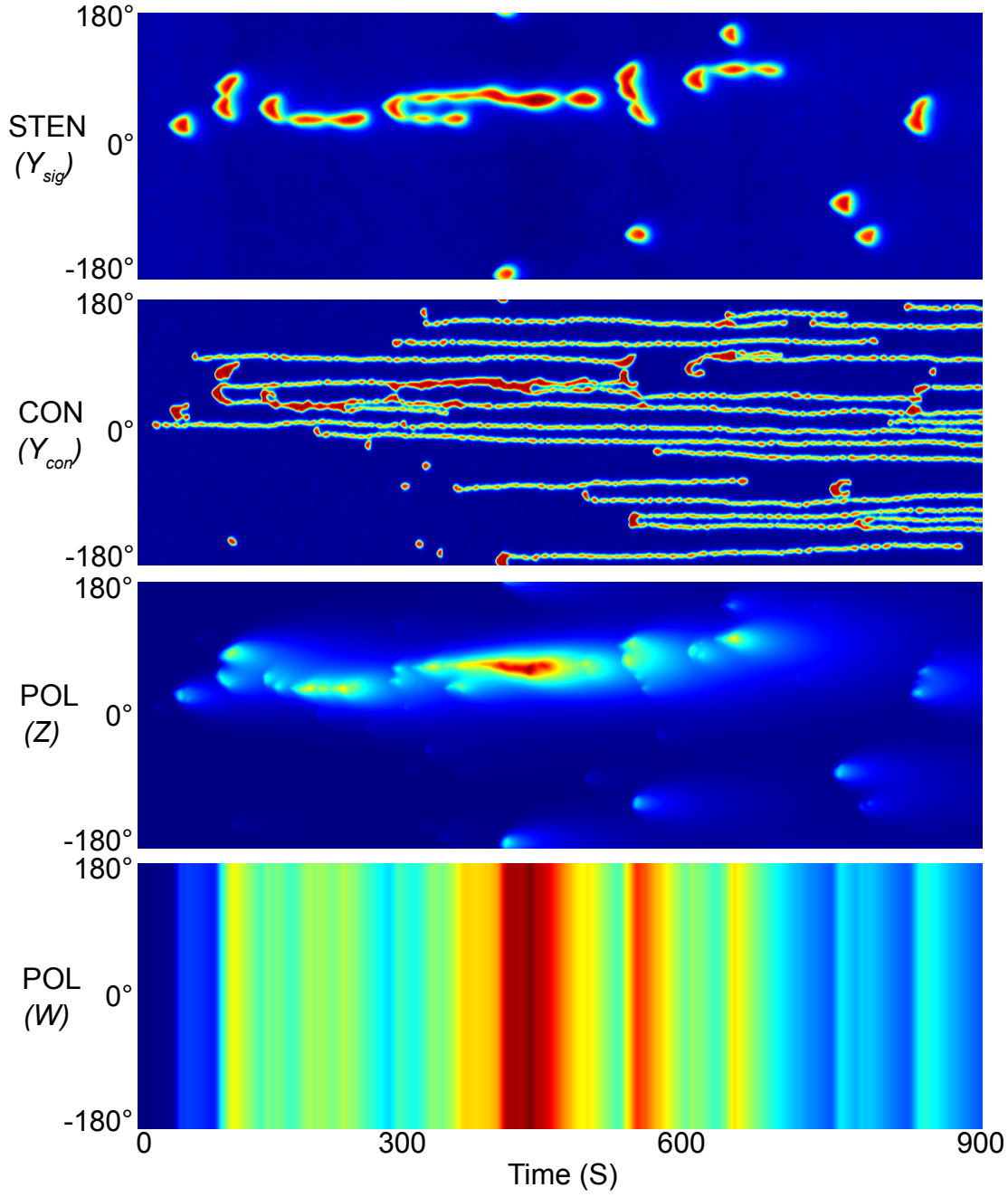

Figure 7.2: Simulated cell behavior in absence of stimulus..

as the response regulator disappeared. The CON was also activated all around cell at time slightly delayed after STEN. This process generated protrusive forces all around the cell membrane which correspond to cell "cringing."

7.2.3 Gradient

We next simulated the model's response to the application of a spatial gradient to the cell. The application of a chemoattractant gradient caused a sudden increase in the activity of the STEN across the cell. As observed in the spatially homogeneous input, this activity disappeared. Thereafter, a series of localized patches appeared with temporal regularity, primarily aligned with the external gradient (Figure 7.4). The activities of the CON and POL modules also increased along this axis.

7.3 Discussion: corresponding biological networks

The modular framework of the polarized LEGI-STEN-CON model gives rise to the entire spectrum of reported behaviors of cells but it is a conceptual model where individual biochemical entities are not assigned to specific model components or modules. An advantage of the modular approach is that, as additional data becomes available, the biochemical network within each module can be modeled in detail without altering the overall behavior of the other modules. Nevertheless, we can use several criteria to begin to assign various biochemical entities to the different modules (Table 7.2). First, the kinetic behaviors of certain biochemical and model components match under different conditions. Second, when levels of components and strengths of feed-

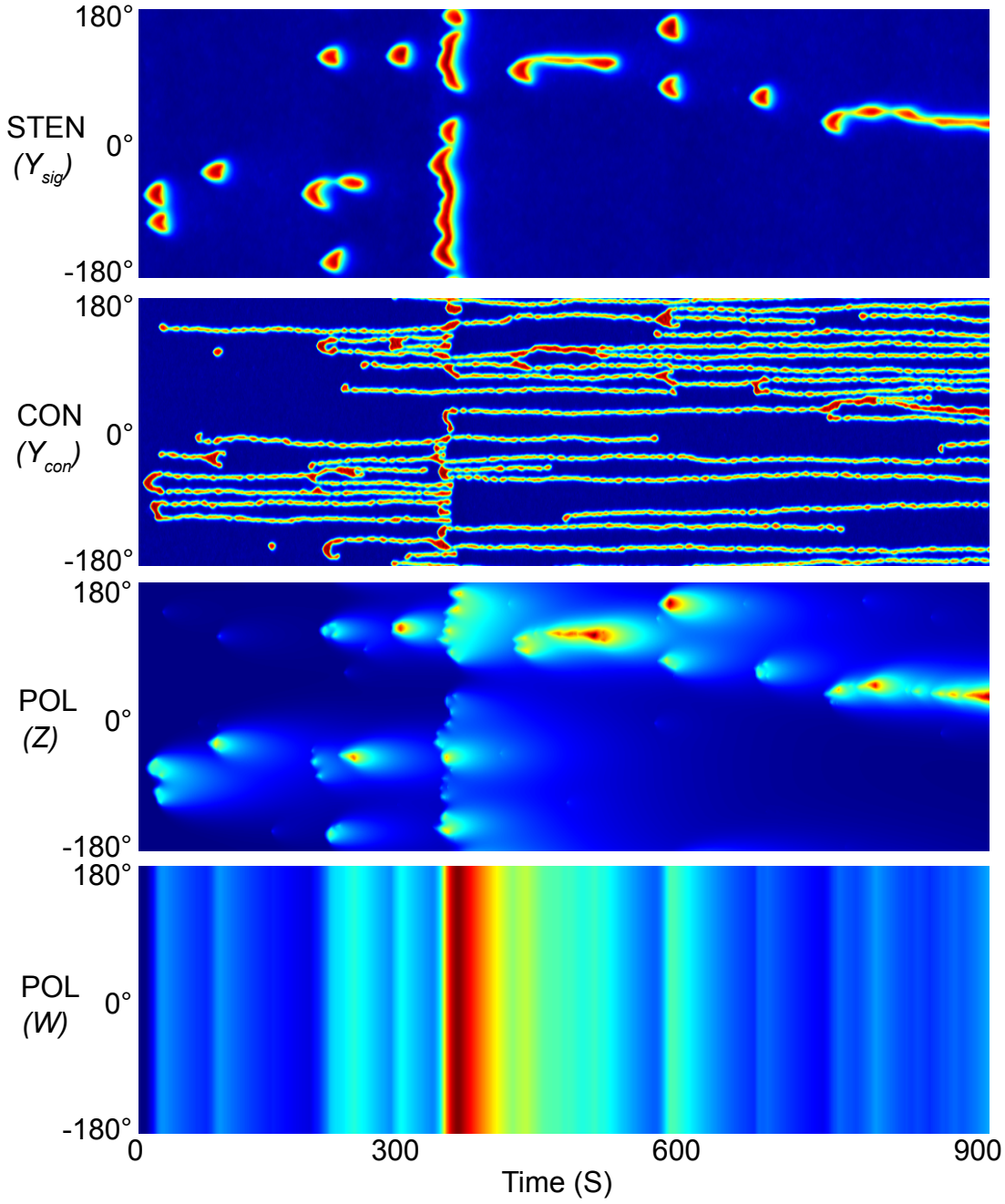

Figure 7.3: Simulated cell response to a spatially uniform stimulus.

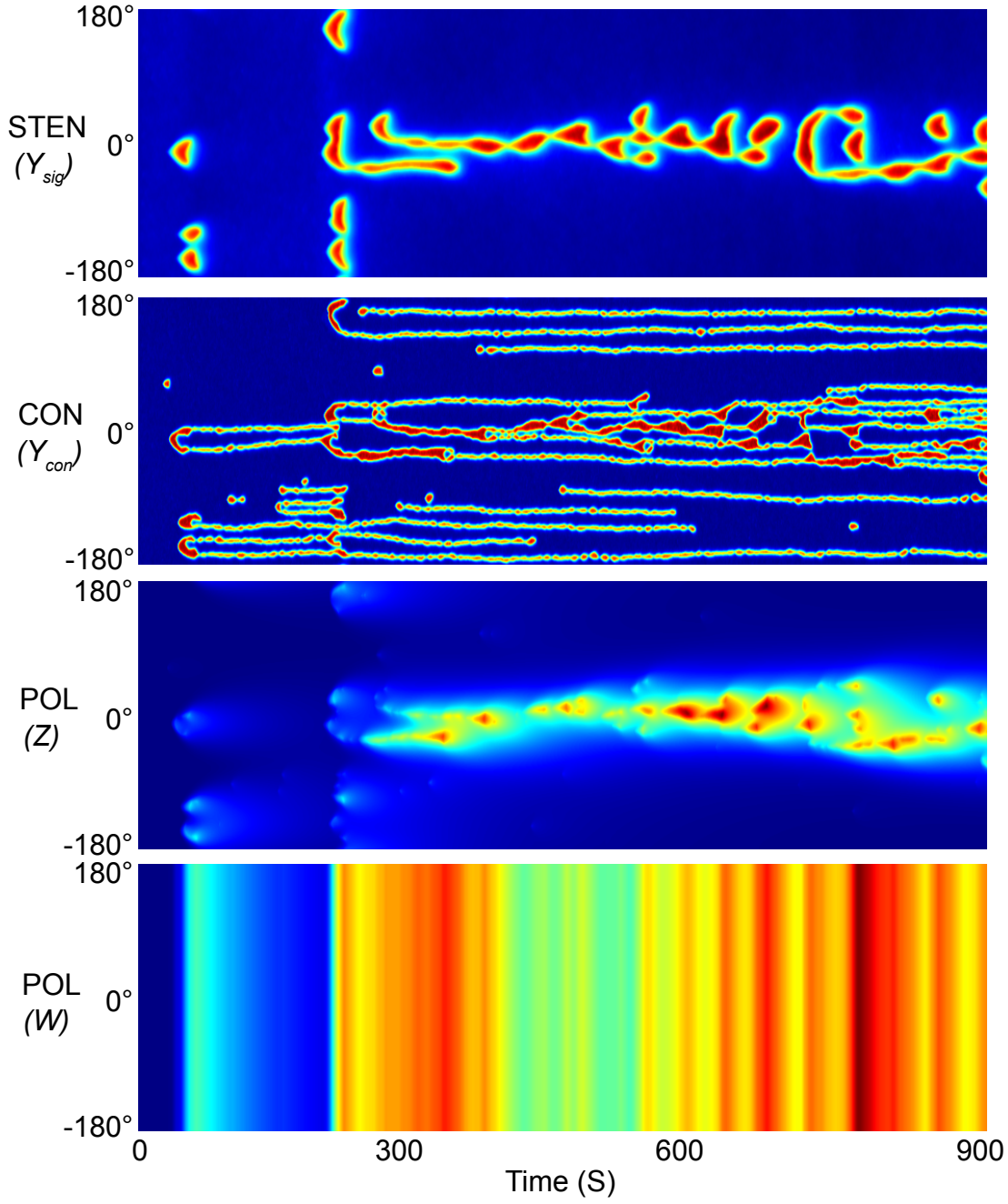

Figure 7.4: Simulated cell behavior with gradient stimulus.

Table 7.2: Putative model components

Modules	**Possible components**
LEGI	Chemoattractant receptors (GPCRs), G-proteins, global inhibitor (unknown)
Excitable Network	Ras GTPases, Ras GEFs, Ras GAPs, PI3K, PTEN, PIP3, TorC2, PDKs, PKBs, PKB substrates, Rho family GTPases
Protrusion	Scar complex, Arp complex, formins, actin, actin-binding proteins
Polarity	Cytoskeletal proteins, membrane tension

backs within modules are varied, our simulated cells can "phenocopy" the behavior of various loss- and gain-of-function mutants.

We propose that the LEGI module incorporates the "upstream" components of the receptor signaling pathway (the chemoattractant-sensing GPCRs and associated G-proteins). Receptor-mediated G-protein dissociation is consistent with the local excitation process since during uniform or gradient stimulation they both rise rapidly and reach a steady-state level proportional to the level of receptor occupancy. Unfortunately, the biochemical identity of the global inhibition process that is expected to rise slowly and balance the persistent G-protein dissociation to bring about adaptation remains unknown. The receptors and G-proteins are not part of the excitable

network since cells in the absence of chemoattractant or lacking G-protein function display excitability [48].

We propose that Ras and PI3K activity as well as other components traditionally viewed as elements of signal transduction pathways are part of the excitable network. Some of these, including Ras, PIP3, and Rac display excitable behavior such as wave propagation along the basal surface of the cell. Furthermore, constitutive Ras activity and inhibition of PIP3 degradation cause excessive cytoskeletal activity and cellular extensions while inhibition of PI3K activity reduces this spontaneous activity. We have also included many signal transduction components that either regulate, or are regulated by, Ras, PI3K, or Rac in this module. While biosensors are not available to directly test the premise, the participation of these components in propagating waves is expected since most of them behave coordinately with Ras and PI3K during uniform chemotactic stimulation.

The CON consists of SCAR/WAVE, Arp2/3, F-actin (represented by LimE and dynacortin), and coronin, which all show rapid oscillations. The temporal relationship and the fact that it is involved in actin depolymerization suggest that coronin may be part of a negative feedback loop in the CON.

The polarity module is likely to include both cytoskeletal and signaling proteins and well as "polarity-specific" components. Cells with elevated levels of PIP3 or Ras activity or lacking myosin II appear to have decreased polarity [92–94]. However, it may be difficult to assign these components specifically to the polarity module

since simulations in which the strengths of the negative feedback loops in either the polarization or excitable network modules are reduced lead to signaling levels and morphologies that are quite similar. Recently, it has been suggested that an activity akin to that achieved by W in the polarization module could be provided by membrane tension thus arguing for a role for cell mechanics [95]. Cells with impaired dynacortin, a global actin linking protein, are softer and also form more pseudopods that are less aligned with the gradient, reminiscent of simulations in which W is reduced.

7.4 Summary

Understanding the signaling cascades that link cell surface receptors to motility and chemotaxis is a challenging task. For this reason, we have first focused on smaller systems in an effort to understand how gradient sensing, motility and polarization are achieved individually. The underlying molecular network, akin to a wiring diagram of an electrical circuit, is then dissected into modules, each comprised of a few components. This chapter has linked them together to assemble a complete model that can account for most of the experimental observations we have collected so far. This complete model helps to understand the underlying mechanism governing chemotaxis.

Chapter 8

A Computational Model of Mitotic Matrix Formation

The formation of the mitotic spindle represents one of nature's most fascinating examples of self-assembly, requiring the concerted action of microtubules (MTs), mitotic motors and associated proteins [5]. A long-standing hypothesis is that a static, non-MT structure might support the assembly of the mitotic spindle by functioning as a scaffold both to restrict diffusion and counteract motor forces [6,96]. Until recently, the existence, much less the nature and molecular identity, of this spindle matrix was uncertain. However, experiments have now provided support for the formation of a mitotic membraneous network by some nuclear proteins including the nuclear lamina protein lamin-B. Tsai et al. showed that the intermediate filament protein lamin B assembles during mitosis into a matrix-like and membrane-containing network in a

RanGTP-dependent manner in Xenopus egg extracts [7]. This lamin-B network appears to both permeate and ensheath spindles assembled in egg extracts. Subsequent experiments have demonstrated that the matrix contains a number of spindle assembly factors, including dynein and Nudel [8]. Interestingly, Drosophila embryos, which are known to perform partially 'open mitosis' with a fenestrated nuclear envelope and nuclear lamina surround the prometaphase and metaphase spindles, assemble a matrix containing nuclear proteins Skeletor, Megator and Chromator that permeates mitotic spindles [97, 98]. Phenotypic analyses of embryos depleted of Skeleton, Megator or Chromator indicate that these proteins are required for proper spindle morphogenesis or function.

How these proteins assemble into spindle matrix remains unclear. Depletion of lamin-B in Xenopus egg extracts or Drosophila early embryos leads to defects in spindle morphology [6, 7, 99, 100]. Lamin-B co-immunoprecipitates with both dynein and Eg5, the plus and minus-end directed motors, respectively, in Xenopus egg extracts [99]. Additionally, lamin-B counteracts the Eg5 forces to help maintaining spindle length, width, and pole focusing [99]. Since upon nuclear envelope breakdown lamin-B-containing nuclear envelope remnants are observed to be transported toward the minus ends of spindle microtubules by dynein [101, 102], the assembly of lamin-B containing mitotic spindle envelope and matrix may require both dynein and microtubules. Consistent with this, depolymerizing microtubules or inhibiting dynein in egg extracts severely inhibited lamin-B assembly [7, 8].

Although the above experiments suggest that nuclear proteins could use microtubules and motors to assemble into the spindle envelope and matrix, how such assembly occurs in conjunction with spindle formation is unclear [9]. Based on the known interactions between lamin-B and motors, we develop a computational model to describe the formation of the lamin-B spindle envelope and matrix and use the model to consider a number of open questions. In the absence of any other structures, are MT dynamics sufficient for a spindle to form, or are additional structures necessary? How is the morphology of the spindle affected by having spatially dependent regulation of the polymerization/depolymerization rates, as might arise because of the RanGTP gradient that develops during mitosis? Can freely diffusible lamin, present throughout the cell after nuclear envelope breakdown, be captured and used to build a network around the spindle? Moreover, what effect does this matrix have on spindle morphology? What possible role does the mitotic matrix play in helping to establish the spindle?

8.1 Computational model of mitotic matrix formation

Given the multitude of possible regulatory models governing spindle formation and the difficulty of isolating them experimentally, computational models are a particularly useful means of testing their respective effects. Mitosis, and in particular, spindle formation has received considerable attention of mathematical and computational models [103–105]. Computational models of spindle assembly come in varying

forms [106]. They may include individual elements (e.g. MTs and MT-motors) and, using first principles from physics, describe the discrete interactions in Monte Carlo simulations [107–109]. Alternatively, continuum models do not attempt to track the interaction of discrete elements. Instead, the filament network is described by a system of coupled differential equations whose solution describes the concentration of the key components over both time and space. As such, they provide information about macroscopic properties of the system. They may be more powerful as they enable consideration of larger systems over longer time scales [110]. Because of the meshwork nature of the spindle matrix which is likely to include numerous interacting discrete filaments, we use a continuum description of the relevant components

Here, a computational model based on a continuum description to represent the abundance and location of the various molecular species involved during mitosis was developed. Specifically, the dynamics of free and polymerized tubulin, microtubules (MTs), the GTPase Ran in both GDP- and GTP-bound forms, and the intermediate filament lamin were tracked. These species are described by continuous concentrations within a two-dimensional spherical cell model.

8.1.1 Model components

Free tubulin (T) diffuses freely throughout the cell. It binds to and dissociates from existing microtubules (Figure 8.1A). Initially, tubulin is uniformly distributed throughout the cell at 12 μM concentration [111].

Microtubules (MTs) describe polymerized tubulin. Initially, all MTs are found

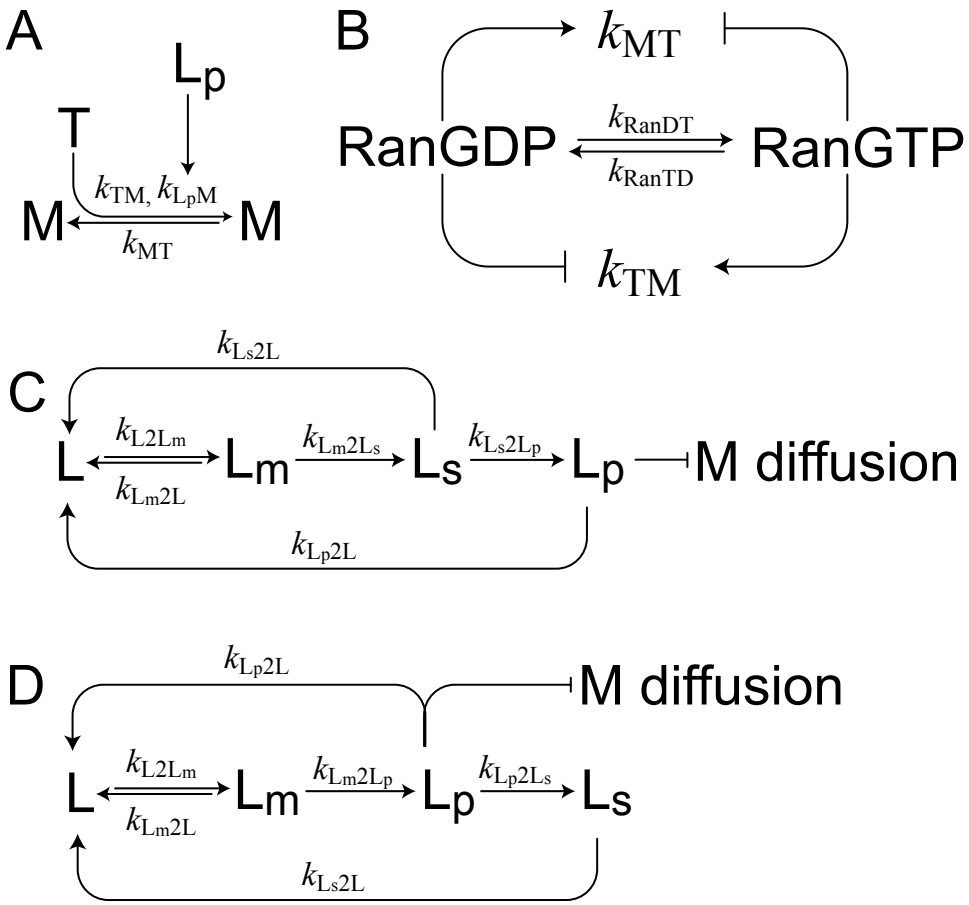

Figure 8.1: Reactions and associated kinetics included in the model. (A) Tubulin (T) attaches to existing microtubules (M) in a reversible reaction. Lamin attached to plus-end directed motors (L_p) increases the rate of polymerization. (B) RanGTP promotes MT polymerization and inhibits depolymerization by decreasing and increasing the corresponding rates (k_{TM} and k_{MT}, respectively). RanGDP acts in a complementary manner. (C) After nuclear envelope breakdown, free lamin (L) is captured by minus-end directed motors moving along MTs - this lamin is labeled L_m. For this lamin we consider two models. In the default model, L_m is stabilized by the matrix (denoted L_s). This can then be captured by plus-end directed motors (denoted L_p). (D) In the second model, lamin that is captured by minus-end directed motors, can then be passed on to plus-end directed motors. The latter can be stabilized by the matrix. In both cases, L_p inhibits MT diffusion.

concentrated at two 1-μm diameter disks, representing asters, 4 μm apart (Figure 8.2A), with initial concentration 30 μM [111]. This concentration is not fixed, but is allowed to vary as MT polymerizes/depolymerizes. The centers of these asters are used as markers for directing the movement of plus- or minus-end motors or motor-associated proteins. To this end, the model tracks whether MTs are associated with one or the other aster. For simplicity, we do not include explicitly the effect of poleward microtubule flux in our model [112]. This flux, which appears to be a conserved process, is coupled to the depolymerization at the minus-ends and is a primary driver of chromosome segregation, though it may also play a role in determining spindle size [113]. In our model, MT growth is restricted by depolymerization.

The model includes the effects of RanGTP on MT polymerization [114]. During mitosis, RanGTP is found preferentially around the chromatin because RCC1, the GEF responsible for nucleotide exchange is chromosome bound [115]. This leads to a high RanGTP to RanGDP ratio near the chromosomes and a low ratio far away. In this model, we restrict production of RanGTP to an ellipsoidal region between the MT asters corresponding to the approximate location of chromosomes during metaphase (Figure 8.2A). RanGTP can diffuse from this region throughout the cytoplasm, where it is hydrolyzed. Initially, all Ran is in the GDP-bound form at a concentration of 2 μM uniformly distributed around the cell. RanGTP stimulates MT assembly by increasing the rescue frequency of MTs [114]. In this model, RanGTP increases MT polymerization and decreases depolymerization rates; RanGDP functions in a

complementary manner (Figure 8.1B).

The lamin mitotic matrix is also part of the model. Lamin B assembles into a matrix-like network during mitosis [7]. Lamin B is assumed to exist in one of several states: free, unbound lamin (L), lamin that is attached to minus- (L_m) or plus-end (L_p) directed motors moving along MTs, and stable lamin bound to and forming the spindle matrix (L_s). Initially, all lamin is in the free state, and concentrated at 12 μM within a 4 μm diameter circle that represents the site of the nucleus just before nuclear envelope breakdown (Figure 8.2A). We assume that lamin that is bound to plus-end directed motors affects MT dynamics by increasing MT nucleation from tubulin, and by stabilizing MTs through reduced diffusion (Figure 8.1C, D). Evidence that lamin may promote MT polymerization comes from the MT assembly promoter XMAP215 which has been shown to associate with the lamin matrix. Lamin may reduce MT diffusion through MT cross-linking proteins, such as NuMA [7] or Rab5 [100], that associate with the matrix.

8.1.2 Geometric description

Our simulations are not meant to represent any specific cell type, as the information on the mitotic matrix comes from variety of sources, including Xenopus egg extracts and Drosophila embryo. We do assume that the reactions take place in a cell surrounded by an impermeable circle, 20 μm in diameter (Fig. 2a). Moreover, we assume complete breakdown of the nuclear envelope. These intracellular compartments are used solely to locate species at the onset of the simulations. Thereafter, all

species diffuse freely within the cell with varying diffusion coefficients (8.1).

8.1.3 Modeled biological process

The dynamics of MT growth are highly stochastic, a process known as dynamic instability. However, as we seek a deterministic description of the system, we model MT polymerization and depolymerization using simple first order reactions, representing average MT growth [116].

After breakdown, components of the nuclear envelope translocate towards centrosomes aided by minus-end-directed MT motors [101]. In our model, free lamin can be captured by minus-end directed motors found on MTs, converting this into minus-end directed lamin (L_m). These motors pull the lamin towards the aster from which the MT emanates.

After lamin capture by minus-end directed motors, we consider two putative pathways. The first scheme, used as the default for most of the simulations in the paper, assumes that lamin held by the minus-end directed motors joins the matrix where it is stabilized - that is, L_m is converted to L_s - at a constant rate. This stable lamin can then be captured by plus-end directed motors (Figure 8.1C). Our second pathway assumes that lamin attached to minus-end directed motors is captured by plus-end directed motors, and it is this lamin that can be stabilized by joining the existing mitotic matrix ($L_m \rightarrow L_p \rightarrow L_s$; (Figure 8.1D)). As there is no experimental basis for preferring one scheme over the other, we use our simulations to test the effect of the two cases. In both cases, lamin that is attached to motors (L_m or L_p) or the matrix

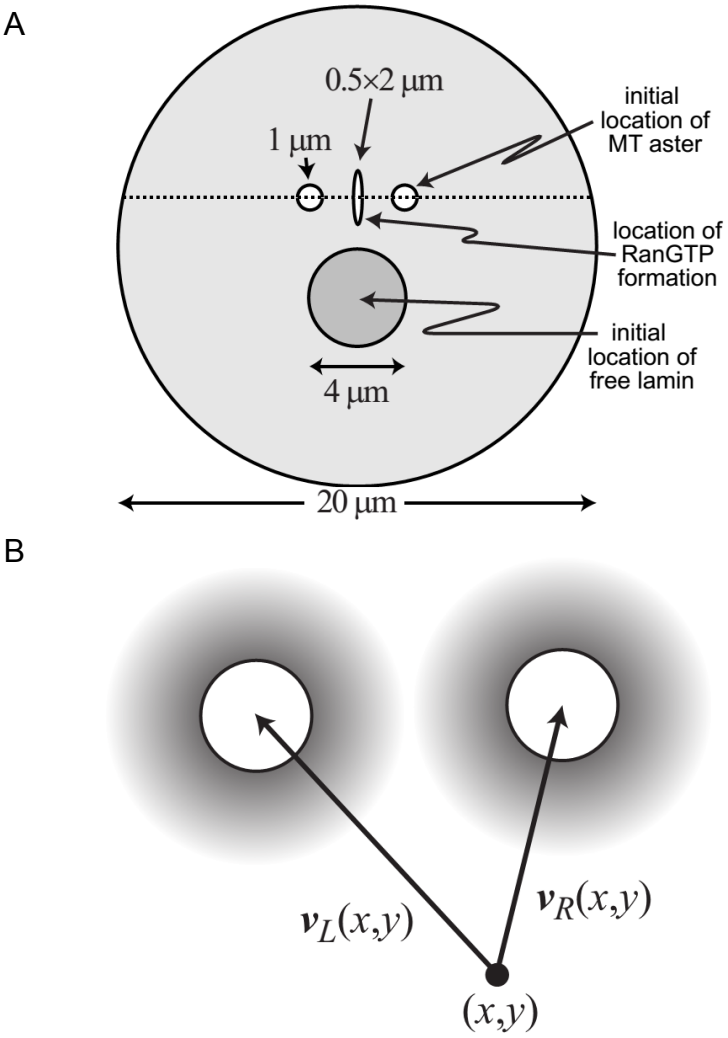

Figure 8.2: Geometric description of the model. (A) The cell is represented by an impenetrable circle, 20 μm in diameter. Lamin and MTs are initialized to one and two circles 4 and 1 μm in diameter, respectively. These species are free to diffuse, however. The ellipse marks the region where RanGDP is converted to RanGTP and where hydrolysis of RanGTP cannot take place. The dotted line shows a cross-section used to plot concentration in subsequent figures. (B) Schematic of the vector field used to describe the movement of motor-associated lamin. Minus-end directed lamin moves along the vector which point to the minus end it attaches ($v_L(x, y)$ and $v_R(x, y)$). Plus-end directed lamin (L_p) in the opposite direction.

(L_s) can become free lamin (L) at constant rates.

8.1.4 Mathematical description

The dynamics of MT polymerization are described first. We track whether MTs are attached to the left (M_L) or right (M_R) asters. Because the equations for the two are the same, we write only one:

$$\begin{aligned}\frac{\partial T}{\partial t} &= D_T\nabla^2 T + k'_{MT}(M_L + M_R) - k'_{TM}(M_L + M_R)T \\ &\quad - k_{L_pM}(L_{pL} + L_{pR})T \\ \frac{\partial M_L}{\partial t} &= D_{MviaL_p}\nabla^2 M_L - k'_{MT}M_L + k'_{TM}M_L T + k_{L_pM}L_{pL}T - v_L{\cdot}\nabla M_L\end{aligned}$$

The first terms in both of these equations represent diffusion. Plus-end directed lamin (L_p) inhibition of MTs diffusion is implemented by:

$$D_{MvialL_p} = (1 - H(L_{pL}, \tau_{L_pDM}))D_M,$$

where D_M is the diffusion coefficient for free MTs. The function:

$$H(x, x_{th}) = 1/(1 + e^{-2(x-x_{th})}),$$

serves as a smooth continuous switch-like function: as x decreases below the threshold x_{th}, the function $H(x, x_{th})$ approaches zero; as x increases above x_{th}, it approaches one.

Polymerization (k'_{TM}) and depolymerization (k'_{MT}) rates depend on the local con-

centrations of RanGTP and RanGDP according to:

$$k'_{TM} = k_{TM}\left(1+\beta\frac{RanGTP}{RanGTP_{\max}}\right)\left(1-\alpha\frac{RanGDP}{RanGDP_{\max}}\right)$$
$$k'_{MT} = k_{MT}\left(1-\alpha\frac{RanGTP}{RanGTP_{\max}}\right)\left(1+\beta\frac{RanGDP}{RanGDP_{\max}}\right)$$

Here, $RanGTP_{\max}$ and $RanGDP_{\max}$ are maximum concentrations obtained within the cell during simulations, and $\alpha = 2$, $\beta = 1/2$ are constants.

The term $k_{L_pM}(L_{pL} + L_{pR})$ in the first equation represents enhancement of MT polymerization by lamin B that has been captured by plus-end directed motors. Finally, the last term $v_L \cdot \nabla M_L$ in the MT equations represents the movement of the asters, and is described in more detail below.

Now we present the model equations for the lamin states. We do this only for the first model (Figure 8.1C); the changes required for the second (Figure 8.1D) are straightforward:

$$\begin{aligned}
\frac{\partial L}{\partial t} &= D_L\nabla^2 L + k_{L_m2L}L_{mL} + k_{L_p2L}L_{pL} + k_{L_s2L}L_{sL} \\
&\quad - k_{L2L_m}L\big(H(M_L,\tau_{ML_m}) + H(M_R,\tau_{ML_m})\big) \\
\frac{\partial L_{mL}}{\partial t} &= D_{L_m}\nabla^2 L_{mL} + k_{L2L_m}LH(M_L,\tau_{ML_m}) - k_{L_m2L_s}L_{mL}H(L_{mL},\tau_{L_mL_s}) \\
&\quad - k_{L_m2L}L_{mL} - v_{L_{mL}}\cdot\nabla L_{mL} \\
\frac{\partial L_{sL}}{\partial t} &= D_{L_s}\nabla^2 L_{sL} + k_{L_m2L_s}L_{mL}H(M_L,\tau_{L_mL_s}) - k_{L_s2L_p}L_{sL}H(L_{sL},\tau_{L_sL_p}) \\
&\quad - k_{L_s2L}L_{sL} \\
\frac{\partial L_{pL}}{\partial t} &= D_{L_p}\nabla^2 L_{pL} + k_{L_s2L_p}L_{sL}H(M_L,\tau_{L_sL_p}) - k_{L_p2L}L_{pL} - v_{L_{pL}}\cdot\nabla L_{pL}.
\end{aligned}$$

The first terms in these equations all represent diffusion of the respective species. The terms $v_{L_{mL}} \cdot \nabla L_{mL}$ and $v_{L_{pL}} \cdot \nabla L_{pL}$ are convection terms and model the movement of captured lamin along MTs (directed either to the left or right asters). All other terms describe the transformation between different states of lamin according to the scheme in (Figure 8.1).

The conversion between RanGDP and RanGTP is assumed to follow first order reactions:

$$\frac{\partial RanGTP}{\partial t} = D_{RanGTP}\nabla^2 RanGTP + k_{RanDT} RanGDP - k_{RanTD} RanGTP$$
$$\frac{\partial RanGDP}{\partial t} = D_{RanGDP}\nabla^2 RanGDP - k_{RanDT} RanGDP + k_{RanTD} RanGTP.$$

The rate constants k_{RanDT} and k_{RanTD} apply only inside and outside the ellipsoidal area around the chromosomes, respectively (Figure 8.2A). However, both species diffuse freely throughout the cell.

Directed MT motors, like kinesins and dynein, move directionally along MTs. In our model, these motors have two functions: they capture lamin and transport it, and they exert force to drive the separation of asters [117].

In our model, the location of the asters is not fixed in space. The force that drives the asters' movement comes from the effects of motors moving along the MTs, which elongates the spindle and separate the asters. Because only motors moving along anti-parallel MTs can exert force [104, 105], we assume that this force is proportional to the product of the concentrations of left- and right-associated MTs (i.e., $ML \times MR$). Because of geometric symmetry of two half spindles, the vertical forces pushing the

asters apart cancel each other. Thus, we only resolve forces in the horizontal direction. Assuming a viscous environment for the cytoplasm, we model aster movement as proportional to the force: $v \propto F = k_f \times ML \times MR$. The proportionality constant, k_f, incorporates such variables as motor concentration, binding/unbinding rates, duty cycle, and cytoplasmic viscosity.

The movement of motor-associated lamin at a point (x, y) is the sum of the movement of MTs relative to the cell, and that of motors relative to the MTs. For simplicity, we propose that MTs have the same velocity as the aster to which they are attached. If $C_i(x, y)$ ($i \in \{L, R\}$, representing the left and right asters, respectively) is the position of the asters' centers, then $W_i = (C_i - P(x, y))/||C_i - P(x, y)||$ is the unit vector pointing to the aster. Let μ_{L_m} and μ_{L_p} be the velocities of lamin captured by minus- and plus-end directed motor, respectively. The velocity of the lamin is given by

$$v_{L_{m_i}} = \mu_{L_m} \cdot W_i H(M_i, \tau_{ML_m}) + v_i$$

$$v_{L_{p_i}} = -\mu_{L_p} \cdot W_i H(M_i, \tau_{ML_p}) + v_i.$$

The switch-like functions $H(M_i, \tau_{ML_m})$ and $H(M_i, \tau_{ML_p})$ ensure that motors can move only if the MT concentration is sufficiently high (above 18 μM) representing the outer extant of the plus end of MTs. The speed of each type of lamin is determined by a mobility parameter. Plus-end directed lamin moves anywhere from 0.1 to 8 μm/s, while the plus-end directed motor kinesin has been observed processing at 0.5 μm/s in vitro [118]. Minus-end directed lamin moves 0.5 to 8 μm/s in the simulation, while the

minus-end directed motor dynein was been observed moving MTs at 0.47 to 6.1 μm/s and averaging 3.5±1.3 μm/s [119].

To determine the elongation of the spindle, we measure the distance between the two asters by tracking the position where the peak MT concentration of each aster occurs.

8.1.5 Parameters

The parameters used in the simulations are shown in Tables 8.1 and 8.2. The kinetic parameters of the RanGTP network were selected based on similar published simulations [120, 121]. As there is relatively little kinetic data on the lamin network, the values selected were chosen through trial and error. In this case, simulations with altered dynamics (doubling or halving the rates) were carried out and gave qualitatively similar results. The diffusion coefficients for the molecule species were obtained using the Stokes-Einstein equation: $D = k_B T/6\rho u R$, where $k_B = 1.38\times10^{-23}\mathrm{JK}^{-1}$ is Boltzmann's constant, $T = 300\,\mathrm{K}$ is temperature in Kelvin, $u = 5\times10^{-3}\,\mathrm{Pa}$ is the viscosity of the cell (assumed to be five times that of water), and R is the Stokes radius of the molecules. We used 2.9 nm for RanGDP and 8.7 nm for RanGTP [120].

8.1.6 Model implementation

Simulations were carried out for 900 seconds using COMSOL Multiphysics.

Table 8.1: Parameters of mitotic spindle matrix formation

Diffusion coefficients		
Tubulin [122]	D_T	48 μm^2/s
Microtubules	D_M	0.005 μm^2/s
RanGDP	D_{RanGDP}	5.0 μm^2/s
RanGTP	D_{RanGTP}	2.0 μm^2/s
Free lamin	D_L	0.1 μm^2/s
Lamin captured by minus-end directed motor	D_{L_m}	0.001 μm^2/s
Lamin associated to matrix	D_{L_s}	0.001 μm^2/s
Lamin captured by plus-end directed motor	D_{L_p}	0.001 μm^2/s

8.2 Results

8.2.1 MT and tubulin interactions alone do not generate a spindle

To establish a benchmark, we simulated our model under the assumption that the only interacting components are MTs and free tubulin. These simulations showed that, without other regulation, MTs formed two aster-like MT rich formations around which a steep MT concentration gradient was established (Figure 8.3A). The region where MTs bound to either aster overlap formed an elliptically shaped region with the MT concentration approximately flat (Figure 8.3A, B). At steady-state, the free tubulin concentration was uniformly distributed throughout the cell (not shown).

We next tested the effect that motors have on the MTs. The force generated by

Table 8.2: Parameters of mitotic spindle matrix formation (cont.)

Kinetic constants		
Microtubule depolymerization	k_{TM}	0.06 s^{-1}
Tubulin polymerization	k_{MT}	0.002 s^{-1}
Ran (GTP to GDP)	k_{RanTD}	0.05 s^{-1}
Ran (GDP to GTP)	k_{RanDT}	2.5 s^{-1}
Lamin (minus-end directed to free)	k_{L_m2L}	0.05 s^{-1}
Lamin (free to minus-end directed)	k_{L2L_m}	0.3 s^{-1}
Lamin (minus- to plus-end directed)	$k_{L_m2L_p}$	0.01 s^{-1}
Lamin (plus-end directed to stable)	$k_{L_p2L_s}$	0.003 s^{-1}
Lamin (stable to free)	k_{L_s2L}	0.001 s^{-1}
Lamin (plus-end directed to free)	k_{L_p2L}	0.001 s^{-1}
Other constants		
Minus-end motor speed [119]	μ_{L_m}	4 $\mu m^2/s$
Plus-end motor speed [119]	μ_{L_m}	0.5 $\mu m^2/s$
Anti-parallel motor force coefficient	k_f	0.2 $\mu ms^{-1}\mu M^{-1}$
Threshold (M effect on -end motor)	τ_{ML_m}	35 μM
Threshold (M effect on +end motor)	τ_{ML_p}	35 μM
Threshold (Lp effect on M diffusion)	$\tau_{L_pD_m}$	1.4 μM
Threshold (Lm effect on Ls)	$\tau_{L_mL_s}$	0 μM
Threshold (Ls effect on Lp)	$\tau_{L_sL_p}$	5 μM

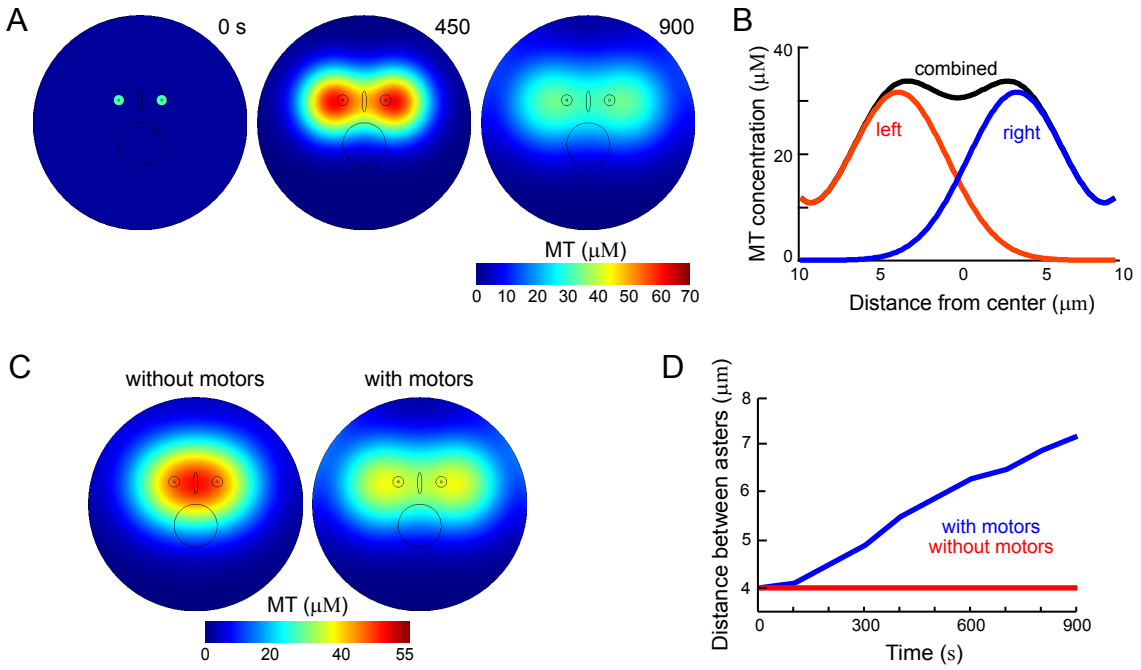

Figure 8.3: MT polymerization gives rise to two asters which are pushed away by the MT-based motors. (A) Dynamic of MT concentration during simulation. MTs grow away from the two initial locations. This simulation includes the effect of MT motors which push the two asters away from each other. This force is generated in the region where MTs from both asters overlap (anti-parallel MTs). (B). Concentration profile at steady state of MTs associated with the two asters along the dotted line of Figure 2(A). (C, D) Comparison of MT profile without and with motors. Though the peak concentration is higher without motors, the asters are not pushed away from each other.

the motors pushed the two asters away, allowing the spindle region to elongate. This had the effect of separating the two asters as well as reducing the peak concentration of MTs (Figure 8.3C). A plot of the length of the interacting MTs (Materials and methods) revealed steady MT growth during the first 100 s (Figure 8.3D). Thereafter, once the MTs from each aster begin to overlap, the force generated by the MT motors pushes the asters apart at a steady rate ((Figure 8.3D). No such separation is achieved in the absence of motors.

8.2.2 Spindle formation and lamin transportation

The previous simulations showed that a spindle region can form without additional components. We next sought to determine the effect that a lamin network could have on the spindle-like region of high MT concentration observed. To this end we introduced the lamin network into our model (Materials and methods). We use the default pathway (Figure 8.1C) to show the effects of lamin. We also included the spatial effects of the RanGTP model. At the onset of these simulations, lamin quickly diffused away from its initial placement, mimicking the release of lamin into the cytoplasm after nuclear envelope breakdown (Figure 8.4A, 20 s). After this initial diffusion, lamin was captured by minus-end directed motors whereupon it was transported towards the two minus ends (Figure 8.4B). As lamin accumulated near these two asters, it detached from the minus-end directed motors and started to bind to the two plus-end directed motors. Thereafter, lamin was transported outwards along the MTs and distributed forming two ring-like patterns (Figure 8.4C, 500–900 s). At

steady-state, lamin attached to minus-end motors was found primarily at the minus ends of the asters (Figure 8.4B). The MTs formed a spindle-like pattern (Figure 8.5A) with higher concentration than in the absence of lamin (peak concentration around 55 μM compared to around 35 μM in Figure 8.3B). More striking was the lack of MTs outside of the spindle region. Because the lamin matrix inhibits MT growth and diffusion, the initial phase of MT growth was reduced, however, a steady state, the MTs form a much more distinct spindle (Figure 8.5B). The asters separated under the action of the MT-associated motors and the average length of the MTs in the spindle was about 4.3 μm (Figure 8.5C).

8.2.3 Ran's effect on MTs dynamics

Previous simulations using agent based models suggested that spatial differences in the regulation of MT interactions can improve spindle morphology [108]. We first established that a RanGTP gradient was formed with the concentration around the center of the spindle approximately three-fold higher than that away from the spindle, which is similar to that reported [120] (Figure 8.6A). This gradient has the effect of increasing the MT polymerization rate by up to 21.4% and decreasing the depolymerization by up to 20% in the spindle region. To test the effect that this spatial regulation has on our spindle morphology we carried out simulations without (Figure 8.6B) and with differentiated production of RanGDP and RanGTP (Figure 8.6C) and compared the localization of the MTs. RanGTP's local enhancement of MT polymerization gave rise to a more distinctive spindle region: in the region between the

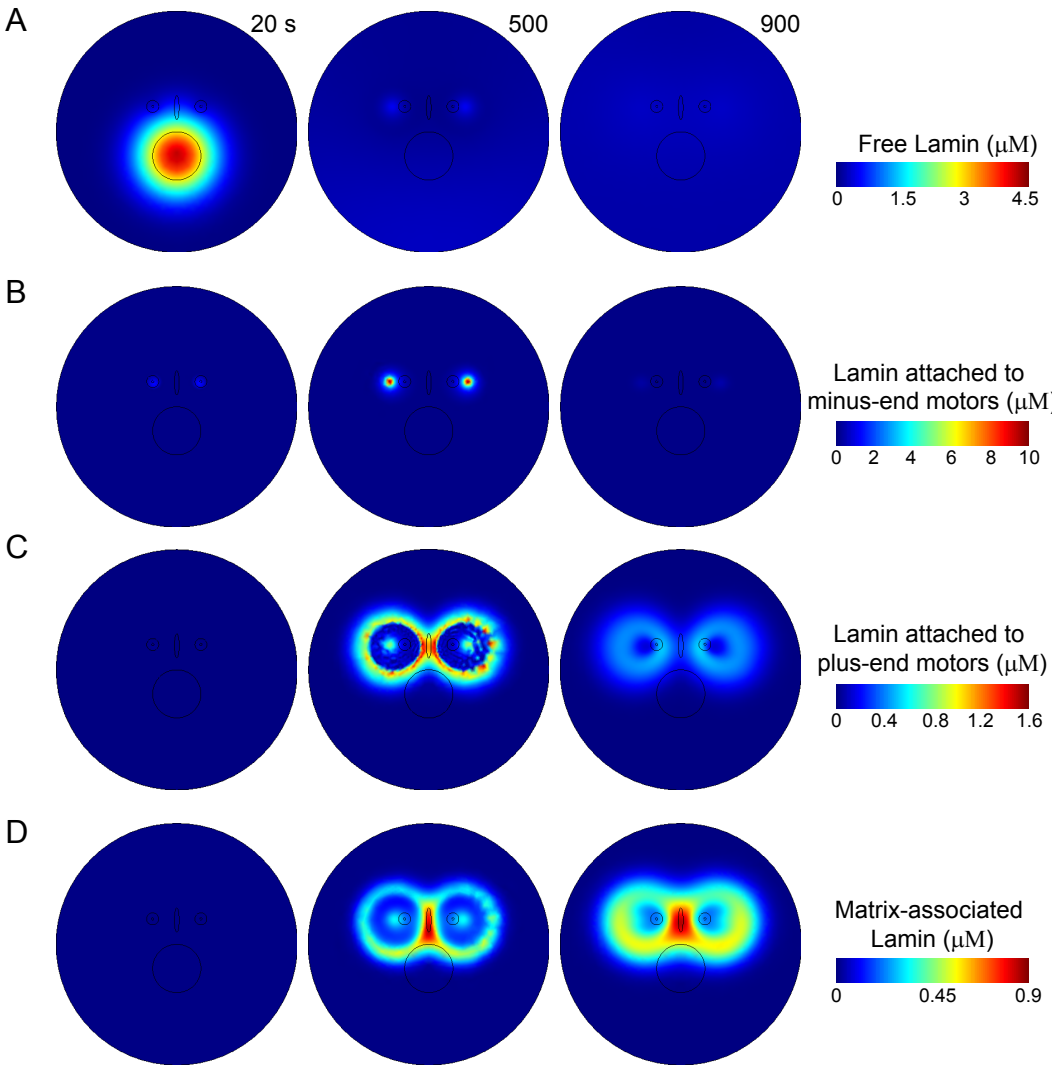

Figure 8.4: Lamin matrix formation around the MT spindle region. Profiles for the free lamin (A), lamin attached to minus- (B) and plus-end (C) directed motors, matrix-associated lamin (D).

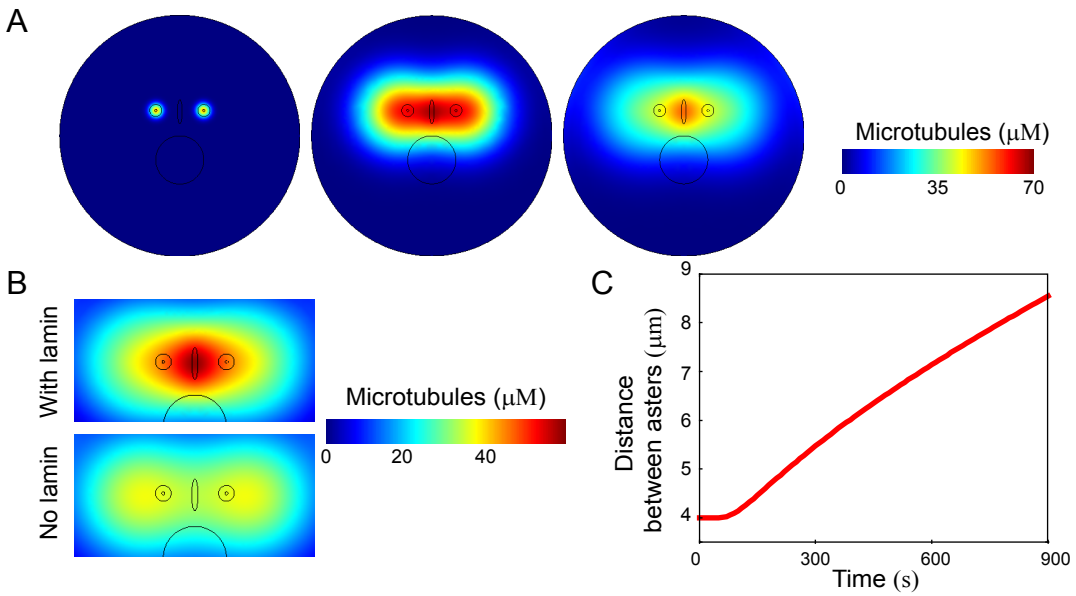

Figure 8.5: MT spindle formation under lamin regulaton. (A) The spatial prfile of MT with lamin. (B) Comparison of MT spindle with and without lamin. (C) With lamin, the distance between the asters grows more gradually because of the resistance provided by the lamin network.

two asters, the concentration of MTs increased from approximately 35 to 55 μM, whereas outside this region, the concentration dropped to nearly zero.

8.2.4 Comparison of two lamin reaction pathways

Also, we contrasted effects of the two proposed mechanisms which determined the transformation after lamin was captured by minus-end directed MT-associated motors (Figure 8.1C, D). The first scheme assumes that lamin captured by minus-end MT motors will then be captured by plus-end directed motors, and then attach itself to the developing lamin matrix as the latter is being formed during spindle assembly. The second scheme assumes that minus-end lamin will transition directly to the matrix from where it can be captured by plus-end directed motors. Both pathways gave

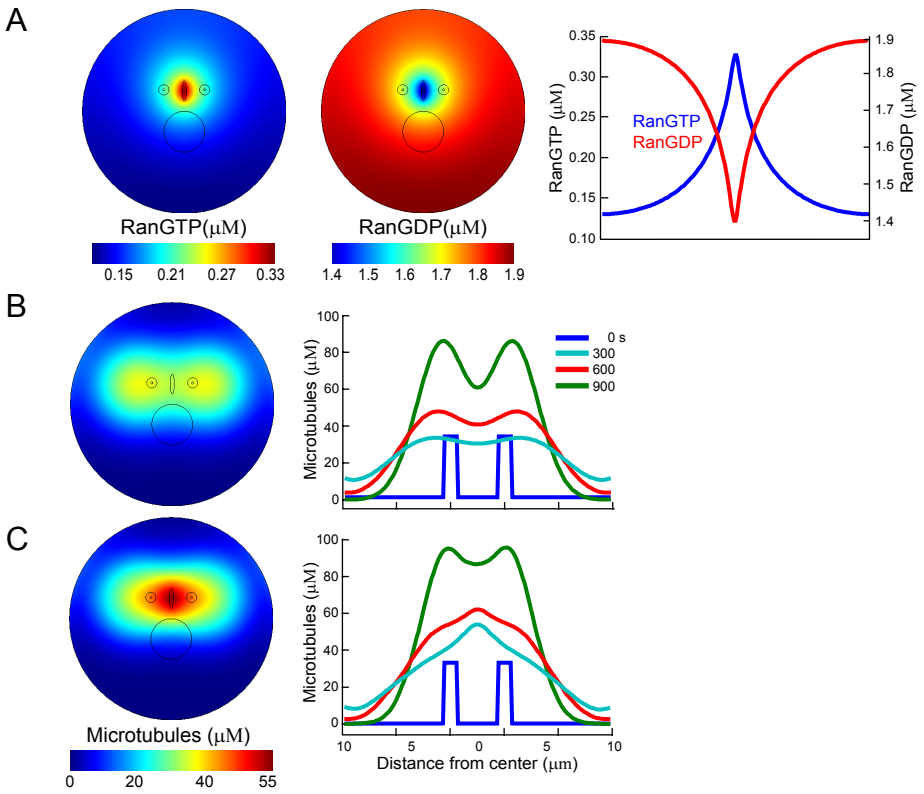

Figure 8.6: Effect of RanGTP on the produfction of the spindle. (A) Spatial distribution of RanGTP and RanGDP concentrations after 900 seconds of simulated time. (B, C) MT concentrations without (B) and with (C) the RanGTP network around the cell, and profiles at four different time points.

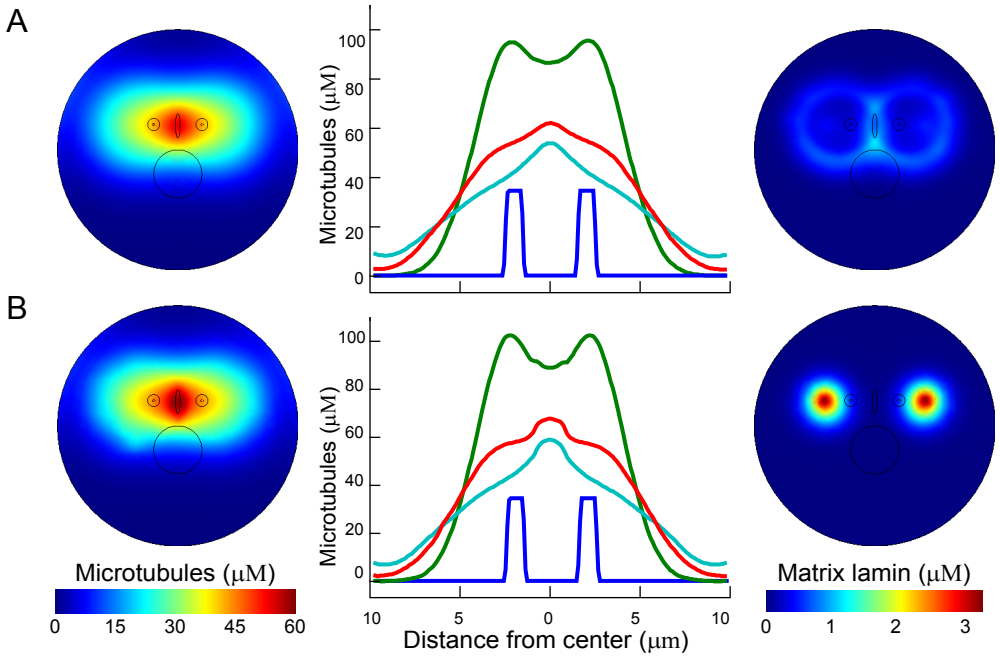

Figure 8.7: Comparison of two putative networks for lamin matrix formation. MT and lamin (L_s) profiles for the scheme of Figure 1C (A) and Figure 1D (B).

rise to similar MT morphologies, though the concentration was somewhat higher in the second scheme (Figure 8.7). However, the effect on the lamin matrix was quite different. In the first scheme, lamin joined the matrix after being transported by the plus-end directed motors, giving rise to two outer rings which join at the center of the spindle region (Figure 8.7A). In the second scheme, because lamin joined the matrix immediately after being captured by the minus-end directed motors, there was high concentration of lamin matrix at the minus-end of the MTs (Figure 8.7B). Two weaker rings were seen as well.

8.2.5 Parameter sensitivity

By necessity, our model requires a number of parameters that have not been measured experimentally. We sought to determine how robust the system is to several of the assumptions made. To this end we varied the initial concentrations of the various species involved (Figure 8.8). Our results indicate that the formation of a spindle, and its enclosure by a lamin matrix, are robust to changes ($\pm 30 - 50\%$) in the concentrations of the individual components. The robustness of spindle assembly upon varying lamin-B concentration is consistent with the observation that lamin-B depletion in egg extracts does not prevent spindle assembly, but it does lead changes of spindle morphology. Consistently, changing the total concentration of lamin in our model affects the degree to which the spindle pole is focused. Interestingly, lamin-B has been implicated in limiting tubulin diffusion in mitosis [123]. How this function of lamin-B might affect spindle assembly remains unclear. Our modeling show that more lamin leads to a bigger spindle. It will be interesting to experimentally vary lamin-B concentration and analyze whether spindle size increases.

Changing the initial MT concentration in the asters had a small effect on the steady-state levels of the MT spindle or lamin matrix. This might be expected since the total tubulin concentration (in MT and free form) is dominated by the free tubulin. As expected, changing this latter value did have a greater effect on both the size of the spindle and on the resultant lamin matrix. When the concentration of free tubulin was increased, there was some interaction between the spindle and the cell membrane that

disrupted the shape of the lamin matrix. Although RanGTP is required for assembly of both spindle (and lamin-B spindle envelope/matrix in egg extracts [7, 124], we found that varying the concentration of Ran had limited effect on either the spindle or lamin matrix.

Although lamin-B is shown to interact with dynein and Eg5, the dynein minus end transport of lamin-B observed upon nuclear envelope breakdown suggest that dynein-lamin-B interaction play a role in assembly of the lamin-B spindle envelope and matrix.

We considered the effect of varying the force component between the antiparallel MTs. Increasing the plus end-directed motor force, as might be the effect of having more motors, leads to greater aster separation (Figure 8.9) and hence a longer spindle. With reduced force, the spindle is smaller, but does have more concentrated MTs.

8.3 Discussion

The hypothesis that a spindle matrix could aid in spindle formation was proposed decades ago, but relatively little evidence has existed until recently. More recently, experimental evidence has been provided for a mitotic lamin B matrix whose absence leads to increased defects in spindle assembly [7]. Here we developed a computational model to investigate the formation of a lamin matrix and to test whether the lamin matrix can function as the proposed spindle matrix.

Simulations that involve only tubulin, MTs and MT-associated motors give rise

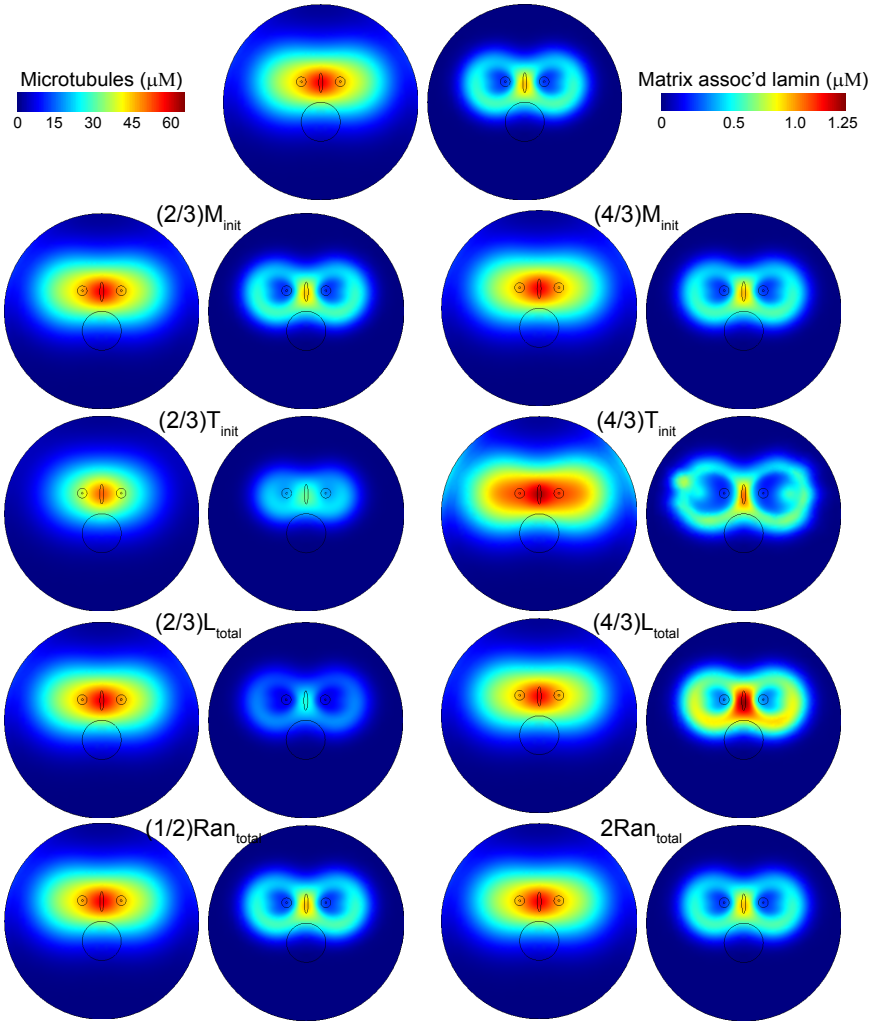

Figure 8.8: Sensitivity analysis for various model parameters. The initial concentrations of the various components was altered (as noted). Plots show the MT and lamin (L_s) profiles.

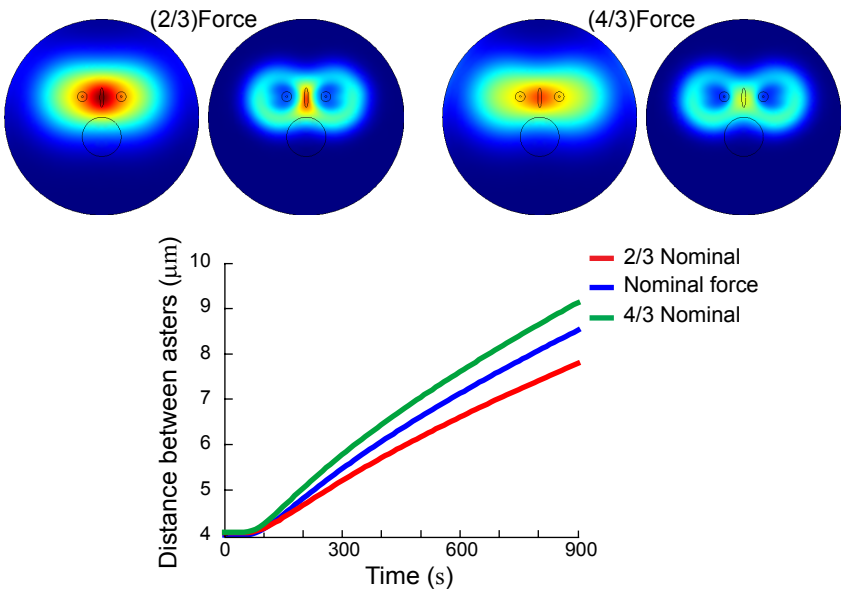

Figure 8.9: Change in the force driving aster separation. Shown are the MT and lamin profiles as well as the aster separation as a function of time.

to a region of high MT concentration between the two asters where a mitotic spindle would be expected to form. MT motors, acting on antiparallel MTs help to push the two asters from each other. The resultant spindle region, however, is relatively unfocused (Figure 8.3C). These simulations show that though the MT network is sufficient for the formation of a spindle, the tightly focused spindles observed in cells likely benefit from other factors.

Introduction of the Ran and Lamin networks into the model improved the morphology of this putative spindle. The Ran network has been extensively studied for its role during mitosis [120, 121]. RanGTP forms a steep gradient emanating from the location of the chromosomes and that it can induce changes in the dynamic instability of the MT network. Previous modeling effort demonstrated that this spatial

regulation could give rise to improved spindle morphology alone [116]. Our model of RanGTP production and hydrolysis, though greatly simplified relative to other models, gave rise to gradients similar to those seen experimentally (Figure 8.6).

After nuclear envelope breakdown, disassembled lamin B is transported to the spindle poles along MTs. Thereafter, lamin B surrounds/permeates the spindle and is concentrated at the spindle poles [8, 101, 125–127]. Our simulations showed that lamin initially found far away from the spindle region can be captured and transported effectively by minus-end directed MT motors (Figure 8.4, Figure 8.5). This lamin was then induced to form a shell-like region of stable lamin around the high concentration of MTs between the two asters, similar to that seen experimentally (Figure 8.4D). Under lamin regulation, microtubules in our simulations formed into a bipolar spindle shape and the increased interaction between the MTs in the spindle region, greatly improving the focusing of this spindle (Figure 8.5A). These simulations are consistent with experimental findings in which disruption of lamin-B lead to disorganized spindles [8, 99]. Moreover, by helping to focus the spindle which allows more microtubule motors to act on overlapping MTs, the lamin matrix helps in the consistent separation of asters and MTs elongation (Figure 8.5B). The model with lamin and Ran finally generates MTs length on the order of 4.5 μm which is close to the experimental measured length in mitotic egg extracts [128]. Our simulations suggest that lamin B, captured by MT-motors after NEB, can act as part of the proposed spindle matrix. There is no direct evidence that lamin is transported along

MTs, though kinesin has been implicated in the MT-dependent transport, leading to assembly of other intermediate filament networks [129]. Moreover, kinesins are seen to remain after disassembly of the spindle by removal of MTs, suggesting that they bind to a non-MT structure, which could be the spindle matrix [130, 131]. Though lamin-B can interact with both dynein and kinesin Eg5 [99], the role of Eg5-lamin-B interaction in spindle morphogenesis or lamin-B matrix assembly is still unclear. Moreover, dynein is required for formation of the lamin B matrix [8]. However, as the mechanism by which lamin captured by minus-end directed motors transitions to the matrix is unclear, we tested two hypothetic pathways. Our simulations suggest that both pathways lead to similar MT spindles (Figure 8.7). The real difference is the shape of the lamin matrix. The scheme in which lamin is captured by plus-end directed motors before stabilizing to the lamin matrix gives two highly concentrated rings along the spindle poles. This is consistent with experiments aimed at deciphering the mechanical interaction between the matrix and MTs [122]. These experiments, which observed the movement of microneedles during spindle elongation, suggest that there is little role for the presence of an isotropic matrix. However, they support a role for a matrix near the spindle poles.

Previous theoretical studies have suggested that the lamin matrix functions to regulate spindle formation by balancing the force generated by the spindle and, in doing so, focusing the spindle [99, 109, 127]. In contrast to these studies, where the effect of the lamin matrix is primarily mechanical [109, 127], our simulations demon-

strate that the matrix spindle, by providing an anchor for spindle assembly factors that regulate MT polymerization, and by physically restricting the movement of MTs (through the coupling of the two networks), can also improve spindle focusing.

8.4 Summary

This chapter has introduced a continuum mathematical model of mitotic matrix formation. Our simulations suggest that lamin B, captured after NEB, can act as part of the long proposed spindle matrix.

Chapter 9

Conclusions

9.1 Contributions

As reported in this dissertation, I have applied mathematical tools to study two eukaryotic cell processes.

9.1.1 Chemotaxis

To understand chemotaxis, I developed a modular framework which allowed me to develop gradually a complete model that can describe chemotaxis in amoeboid cells. Specifically:

1. Chapter 3 considered whether adaptation and gradient sensing could be achieved using a local-excitation, global-inhibition network in which the excitation and inhibition processes form a negative feedback loop (NFB). As demonstrated, this LEGI-NFB also achieves adaptation and gradient sensing, though it is un-

likely that the adaptive properties of *Dictyostelium* cells are implemented in this way, since removal of the stimulus led to significant damped oscillations, which are not observed in the response of amoebae. Nevertheless, showing that there is a second means of achieving adaptation and static spatial sensing may be of importance in describing the gradient sensing capabilities other systems. Simulations in this chapter further tested the feasibility of the LEGI-BEN system under various situations.

2. Chapter 4 described a mathematical framework for simulating changes in cellular morphology based on level set methods (LSM). Using this framework, we linked the responses of the signaling network to describe cell migration. By connecting the LEGI-BEN system to the viscoelastic model as described using LSM, we generated realistic cell shape changes under various conditions recreating experimental findings. This is a powerful tool, not only for testing current hypotheses, but also in suggesting new research directions. Based on our simulations, we concluded that the LEGI-BEN cannot fully recreate the chemotactic behaviors as cells following this scheme show no persistence when migrating randomly, and no polarity.

3. In Chapter 5, I developed a polarity module (POL) and added it to the LEGI-BEN. Using this new module, we could explain the intrinsic polarity existing in chemotaxis cells. After formulating the model with partial differential equa-

tions, I carried simulations under various experimental conditions. When coupled to the LSM framework, this Polarized-LEGI-BEN recreated most of the experimentally observed features of chemotactic, amoeboid cells.

4. Chapter 6 reports on new experimental findings that demonstrate the presence of oscillatory behavior in the cytoskeletal network of migrating cells. To account for these findings, we developed a new model for a cytoskeletal oscillatory network (CON) that is separate from the excitable network, renamed the signal transduction excitable network (STEN). This coupled STEN-CON system accounts for the migration of cells.

5. In Chapter 7, I combined the various modules, LEGI, STEN, CON and POL, to form a complete model describing chemotaxis. I also discussed the potential biological networks corresponding to each module.

9.1.2 Mitosis

Besides chemotaxis, I carried out research into another important cell behavior: the formation of a lamin matrix surrounding the mitotic spindle during mitosis. In particular:

6. In Chapter 8, I developed a computational model based on a continuum description to represent the abundance and location of the various molecular species involved during mitosis, and used it to test a number of hypotheses regarding the formation of the mitotic matrix. My simulations showed that lamin can be used

to build a shell-like region that envelopes the mitotic spindle, which helps to improve the focusing of the mitotic spindle by spatially restricting microtubule polymerization and limiting the effective diffusion of the free microtubules. Simulations also confirm that spatially dependent regulation of the spindle network through the Ran system improves spindle focusing and morphology. The results agreed with experimental observations that lamin-B reorganizes around the spindle and helps to maintain spindle morphology.

9.2 Future directions

Here I make three broad recommendations for future research, two relating to the chemotaxis model, and the third to the model of spindle matrix formation.

1. Though this dissertation reports the development of a complete model that describes chemotaxis, the model could be tested further. I considered the behavior of the model in the absence of stimuli, under spatially uniform stimuli and spatial gradients. Further tests could be done. For example, a greater range of chemoattaractant levels, as well as shifts in the gradient. These experiments can help to target better parameter sets. By incorporating the model within the LSM, more complex cell migration behaviors can also be simulated, including flow chamber migration and maze path findings.

2. The description of each module in the model is abstract, not tying it to specific biochemical entitites. We have hypothesized that components of the re-

ceptor signaling pathway (the chemoattractant-sensing GPCRs and associated G-proteins) forms the LEGI module and that Ras and PI3K activity as well as other components traditionally viewed as elements of signal transduction pathways are part of the STEN. The CON consists of SCAR/WAVE, Arp2/3, F-actin (represented by LimE and dynacortin), and coronin, which all show rapid oscillations. The POL is more elusive now and is likely to include both cytoskeletal and signaling proteins and well as "polarity-specific" components. The precise assignment of these components will require further investigation. Moreover, the role of feedback loops is essential in these modules but, experimentally, these mechanisms are not well understood.

3. In the description of the mitotic matrix, the nature of the interaction between the microtubule-motors and lamin is still hypothetical. Further experiments will need to be carried to specify this interaction before the model can be extended.

Bibliography

[1] K. F. Swaney, C.-H. Huang, and P. N. Devreotes, "Eukaryotic chemotaxis: A network of signaling pathways controls motility, directional sensing, and polarity," *Annual Review of Biophysics*, vol. 39, no. 1, pp. 265–289, 2010.

[2] A. D. Luster, "Chemokines chemotactic cytokines that mediate inflammation," *New England J. Medicine*, vol. 338, no. 7, pp. 436–445, 1998.

[3] D. Kedrin, J. Rheenen, L. Hernandez, J. Condeelis, and J. E. Segall, "Cell motility and cytoskeletal regulation in invasion and metastasis," *J. Mammary Gland Biology and Neoplasia*, vol. 12, no. 2-3, pp. 143–152, 2007.

[4] I. C. Schneider and J. M. Haugh, "Mechanisms of gradient sensing and chemotaxis: Conserved pathways, diverse regulation," *Cell Cycle*, vol. 5, no. 1, pp. 1130–1134, 2006.

[5] E. Karsenti and I. Vernos, "The mitotic spindle: A self-made machine," *Science*, vol. 294, no. 5542, pp. 543–547, 2001.

Bibliography

[6] J. M. Scholey, G. C. Rogers, and D. J. Sharp, "Mitosis, microtubules, and the matrix," *J. Cell Biology*, vol. 154, no. 2, pp. 261–266, 2001.

[7] M.-Y. Tsai, S. Wang, J. M. Heidinger, D. K. Shumaker, S. A. Adam, R. D. Goldman, and Y. Zheng, "A mitotic lamin B matrix induced by RanGTP required for spindle assembly," *Science*, vol. 311, no. 5769, pp. 1887–1893, 2006.

[8] L. Ma, M.-Y. Tsai, S. Wang, B. Lu, R. Chen, J. R. Y. III, X. Zhu, and Y. Zheng, "Requirement for nudel and dynein for assembly of the lamin B spindle matrix," *Nature Cell Biology*, vol. 11, no. 1083, pp. 247–256, 2009.

[9] K. Johansen, A. Forer, C. Yao, J. Girton, and J. Johansen, "Do nuclear envelope and intranuclear proteins reorganize during mitosis to form an elastic, hydrogel-like spindle matrix?" *Chromosome Research*, vol. 19, no. 3, pp. 345–365, 2011.

[10] Y. Xiong, C.-H. Huang, P. A. Iglesias, and P. N. Devreotes, "Cells navigate with a local-excitation, global-inhibition-biased excitable network," *Proc. National Academy Sciences, U.S.A.*, vol. 107, no. 40, pp. 17 079–17 086, 2010.

[11] L. Bosgraaf and P. J. M. Van Haastert, "The ordered extension of pseudopodia by amoeboid cells in the absence of external cues," *PLoS ONE*, vol. 4, no. 4, p. e5253, 04 2009.

[12] C. A. Parent and P. N. Devreotes, "A cell's sense of direction," *Science*, vol. 284, no. 5415, pp. 765–770, 1999.

Bibliography

[13] C. Janetopoulos, L. Ma, P. N. Devreotes, and P. A. Iglesias, "Chemoattractant-induced phosphatidylinositol 3,4,5-trisphosphate accumulation is spatially amplified and adapts, independent of the actin cytoskeleton," *Proc. National Academy Sciences, U.S.A.*, vol. 101, no. 24, pp. 8951–8956, 2004.

[14] P. Devreotes and C. Janetopoulos, "Eukaryotic chemotaxis: Distinctions between directional sensing and polarization," *J. Biological Chemistry*, vol. 278, no. 23, pp. 20 445–20 448, 2003.

[15] N. Andrew and R. H. Insall, "Chemotaxis in shallow gradients is mediated independently of ptdins 3-kinase by biased choices between random protrusions," *Nature Cell Biology*, vol. 9, no. 2, pp. 193–200, 2007.

[16] C. A. Parent, B. J. Blacklock, W. M. Froehlich, D. B. Murphy, and P. N. Devreotes, "G protein signaling events are activated at the leading edge of chemotactic cells," *Cell*, vol. 95, no. 1, pp. 81–91, 1998.

[17] R. Meil1i, C. Ellsworth, S. Lee, T. Reddy, H. Ma, and R. A. Firtel, "Chemoattractant-mediated transient activation and membrane localization of Akt/PKB is required for efficient chemotaxis to cAMP in *Dictyostelium*," *EMBO J*, vol. 18, no. 8, pp. 2092–2105, 1999.

[18] M. Postma, J. Roelofs, J. Goedhart, T. W. Gadella, A. J. Visser, and P. J. Van Haastert, "Uniform cAMP stimulation of *Dictyostelium* cells induces lo-

calized patches of signal transduction and pseudopodia," *Molecular Biology of the Cell*, vol. 14, no. 12, pp. 5019–5027, 2003.

[19] M. G. Vicker, "Reaction-diffusion waves of actin filament polymerization/depolymerization in *Dictyostelium* pseudopodium extension and cell locomotion," *Biophysical Chemistry*, vol. 84, no. 2, pp. 87–98, 2000.

[20] G. Gerisch, T. Bretschneider, A. Müller-Taubenberger, E. Simmeth, M. Ecke, S. Diez, and K. Anderson, "Mobile actin clusters and traveling waves in cells recovering from actin depolymerization," *Biophysical J.*, vol. 87, no. 5, pp. 3493–3503, 2004.

[21] O. D. Weiner, W. A. Marganski, L. F. Wu, S. J. Altschuler, and M. W. Kirschner, "An actin-based wave generator organizes cell motility," *PLoS Biology*, vol. 5, no. 9, p. e221, 08 2007.

[22] Y. T. Maeda, J. Inose, M. Y. Matsuo, S. Iwaya, and M. Sano, "Ordered patterns of cell shape and orientational correlation during spontaneous cell migration," *PLoS ONE*, vol. 3, no. 11, p. e3734, 11 2008.

[23] Y. Arai, T. Shibata, S. Matsuoka, M. J. Sato, T. Yanagida, and M. Ueda, "Self-organization of the phosphatidylinositol lipids signaling system for random cell migration," *Proc. National Academy Sciences, U.S.A.*, vol. 107, no. 27, pp. 12 399–12 404, 2010.

Bibliography

[24] Y. Xiong, C. Kabacoff, J. Franca-Koh, P. Devreotes, D. Robinson, and P. A. Iglesias, "Automated characterization of cell shape changes during amoeboid motility by skeletonization," *BMC Systems Biology*, vol. 4, no. 1, p. 33, 2010.

[25] R. P. Futrelle, J. Traut, and W. G. McKee, "Cell behavior in *Dictyostelium discoideum*: preaggregation response to localized cyclic AMP pulses." *J. Cell Biology*, vol. 92, no. 3, pp. 807–821, 1982.

[26] K. Takeda, D. Shao, M. Adler, P. G. Charest, W. F. Loomis, H. Levine, A. Groisman, W.-J. Rappel, and R. A. Firtel, "Incoherent feedforward control governs adaptation of activated Ras in a eukaryotic chemotaxis pathway," *Science Signal.*, vol. 5, no. 205, p. ra2, 2012.

[27] C. J. Wang, A. Bergmann, B. Lin, K. Kim, and A. Levchenko, "Diverse sensitivity thresholds in dynamic signaling responses by social amoebae," *Science Signal.*, vol. 5, no. 213, p. ra17, 2012.

[28] L. Chen, C. Janetopoulos, Y. E. Huang, M. Iijima, J. Borleis, and P. N. Devreotes, "Two phases of actin polymerization display different dependencies on PI(3,4,5)P3 accumulation and have unique roles during chemotaxis," *Molecular Biology of the Cell*, vol. 14, no. 12, pp. 5028–5037, 2003.

[29] M. Postma, J. Roelofs, J. Goedhart, H. M. Loovers, A. J. W. G. Visser, and P. J. M. Van Haastert, "Sensitization of *Dictyostelium* chemotaxis by

phosphoinositide-3-kinase-mediated self-organizing signalling patches," *J. Cell Science*, vol. 117, no. 14, pp. 2925–2935, 2004.

[30] A. Samadani, J. Mettetal, and A. van Oudenaarden, "Cellular asymmetry and individuality in directional sensing," *Proc. National Academy Sciences, U.S.A.*, vol. 103, no. 31, pp. 11 549–11 554, 2006.

[31] M. D. Onsum, K. Wong, P. Herzmark, H. R. Bourne, and A. P. Arkin, "Morphology matters in immune cell chemotaxis: membrane asymmetry affects amplification," *Physical Biology*, vol. 3, no. 3, p. 190, 2006.

[32] R. Tranquillo, D. Lauffenburger, and S. Zigmond, "A stochastic model for leukocyte random motility and chemotaxis based on receptor binding fluctuations," *J. Cell Biology*, vol. 106, no. 2, pp. 303–309, 1988.

[33] L. Bosgraaf and P. J. M. Van Haastert, "Navigation of chemotactic cells by parallel signaling to pseudopod persistence and orientation," *PLoS ONE*, vol. 4, no. 8, p. e6842, 08 2009.

[34] H. U. Bödeker, C. Beta, T. D. Frank, and E. Bodenschatz, "Quantitative analysis of random ameboid motion," *EPL (Europhysics Letters)*, vol. 90, no. 2, p. 28005, 2010.

[35] L. Li, E. C. Cox, and H. Flyvbjerg, "'Dicty dynamics': *Dictyostelium* motility as persistent random motion," *Physical Biology*, vol. 8, no. 4, p. 046006, 2011.

[36] H. Takagi, M. J. Sato, T. Yanagida, and M. Ueda, "Functional analysis of spontaneous cell movement under different physiological conditions," *PLoS ONE*, vol. 3, no. 7, p. e2648, 07 2008.

[37] J. A. Swanson and D. L. Taylor, "Local and spatially coordinated movements in *Dictyostelium discoideum* amoebae during chemotaxis," *Cell*, vol. 28, no. 2, pp. 225–232, 1982.

[38] A. M. Turing, "The chemical basis of morphogenesis," *Philosophical Trans. Royal Society of London. Series B, Biological Sciences*, vol. 237, no. 641, pp. 37–72, 1952.

[39] H. Meinhardt and A. Gierer, "Applications of a theory of biological pattern formation based on lateral inhibition," *J. Cell Science*, vol. 15, no. 2, pp. 321–346, 1974.

[40] S. J. Altschuler, S. B. Angenent, Y. Wang, and L. F. Wu, "On the spontaneous emergence of cell polarity," *Nature*, vol. 454, no. 7206, pp. 886–889, 2008.

[41] Y. Mori, A. Jilkine, and L. Edelstein-Keshet, "Wave-pinning and cell polarity from a bistable reaction-diffusion system," *Biophysical J.*, vol. 94, no. 9, pp. 3684–3697, 2008.

[42] M. D. Onsum and C. V. Rao, "Calling heads from tails: the role of mathematical

modeling in understanding cell polarization," *Current Opinion in Cell Biology*, vol. 21, no. 1, pp. 74–81, 2009.

[43] A. Jilkine and L. Edelstein-Keshet, "A comparison of mathematical models for polarization of single eukaryotic cells in response to guided cues," *PLoS Computational Biology*, vol. 7, no. 4, p. e1001121, 04 2011.

[44] A. Levchenko and P. A. Iglesias, "Models of eukaryotic gradient sensing: Application to chemotaxis of amoebae and neutrophils," *Biophysical J.*, vol. 82, no. 1, pp. 50–63, 2002.

[45] H. Levine, D. A. Kessler, and W.-J. Rappel, "Directional sensing in eukaryotic chemotaxis: A balanced inactivation model," *Proc. National Academy Sciences, U.S.A.*, vol. 103, no. 26, pp. 9761–9766, 2006.

[46] A. Mogilner, "Mathematics of cell motility: have we got its number?" *J. Mathematical Biology*, vol. 58, no. 1-2, pp. 105–134, 2009.

[47] T. Bretschneider, S. Diez, K. Anderson, J. Heuser, M. Clarke, A. Müller-Taubenberger, J. Köhler, and G. Gerisch, "Dynamic actin patterns and Arp2/3 assembly at the substrate-attached surface of motile cells," *Current Biology*, vol. 14, no. 1, pp. 1–10, 2004.

[48] T. Bretschneider, K. Anderson, M. Ecke, A. Müller-Taubenberger, B. Schroth-Diez, H. C. Ishikawa-Ankerhold, and G. Gerisch, "The three-dimensional dy-

namics of actin waves, a model of cytoskeletal self-organization," *Biophysical J.*, vol. 96, no. 7, pp. 2888–2900, 2009.

[49] P. A. Iglesias and P. N. Devreotes, "Biased excitable networks: how cells direct motion in response to gradients," *Current Opinion in Cell Biology*, vol. 24, no. 2, pp. 245–253, 2012.

[50] J. Allard and A. Mogilner, "Traveling waves in actin dynamics and cell motility," *Current Opinion in Cell Biology*, vol. 25, no. 1, pp. 107–115, 2013.

[51] B. L. Kutscher, P. N. Devreotes, and P. A. Iglesias, "Local excitation, global inhibition mechanism for gradient sensing: An interactive applet," *Science STKE*, vol. 2004, no. 219, p. pl3, 2004.

[52] L. Yang and P. A. Iglesias, "Positive feedback may cause the biphasic response observed in the chemoattractant-induced response of *Dictyostelium* cells," *Systems & Control Letters*, vol. 55, no. 4, pp. 329–337, 2006.

[53] A. L.Hodgkin and A. F. Huxley, "A quantitative description of membrane and its application to conduction and excitation in nerve," *J. Physiology*, vol. 117, no. 1, pp. 500–544, 1952.

[54] R. FitzHugh, "Impulses and physiological states in theoretical models of nerve membrane," *Biophysical J.*, vol. 1, no. 6, pp. 445–466, 1961.

Bibliography

[55] S. Y. J. Nagumo, S. Arimoto, "An active pulse transmission line simulating nerve axon," *Proc. IRE*, vol. 50, no. 1, pp. 2061–2070, 1962.

[56] L. Yang, J. Effler, B. Kutscher, S. Sullivan, D. Robinson, and P. A. Iglesias, "Modeling cellular deformations using the level set formalism," *BMC Systems Biology*, vol. 2, no. 1, p. 68, 2008.

[57] S. Osher and J. A. Sethian, "Fronts propagating with curvature-dependent speed: Algorithms based on Hamilton-Jacobi formulations," *J. Computational Physics*, vol. 79, no. 1, pp. 12–49, 1988.

[58] W. Mulder, S. Osher, and J. A. Sethian, "Computing interface motion in compressible gas dynamics," *J. Computational Physics*, vol. 100, no. 2, pp. 209–228, 1992.

[59] C. C. Poirier, W. P. Ng, D. N. Robinson, and P. A. Iglesias, "Deconvolution of the cellular force-generating subsystems that govern cytokinesis furrow ingression," *PLoS Computational Biology*, vol. 8, no. 4, p. e1002467, 04 2012.

[60] L. Ma, C. Janetopoulos, L. Yang, P. N. Devreotes, and P. A. Iglesias, "Two complementary, local excitation, global inhibition mechanisms acting in parallel can explain the chemoattractant-induced regulation of PI(3,4,5)P3 response in *Dictyostelium* cells," *Biophysical J.*, vol. 87, no. 6, pp. 3764–3774, 2004.

Bibliography

[61] N. Barkai and S. Leibler, "Robustness in simple biochemical networksy," *Nature*, vol. 387, no. 6636, pp. 913–917, 1997.

[62] T.-M. Yi, Y. Huang, M. I. Simon, and J. Doyle, "Robust perfect adaptation in bacterial chemotaxis through integral feedback control," *Proc. National Academy Sciences, U.S.A.*, vol. 97, no. 9, pp. 4649–4653, 2000.

[63] W. Ma, A. Trusina, H. El-Samad, W. A. Lim, and C. Tang, "Defining network topologies that can achieve biochemical adaptation," *Cell*, vol. 138, no. 4, pp. 760–773, 2009.

[64] B. Francis and W. Wonham, "The internal model principle for linear multivariable regulators," *Applied Mathematics and Optimization*, vol. 2, no. 2, pp. 170–194, 1975.

[65] B. W. Andrews, P. A. Iglesias, and E. D. Sontag, "Signal detection and approximate adaptation implies an approximate internal model," in *45th IEEE Conference Decision and Control*, 2006, pp. 2364–2369.

[66] J. Krishnan and P. A. Iglesias, "Analysis of the signal transduction properties of a module of spatial sensing in eukaryotic chemotaxis," *Bulletin of Mathematical Biology*, vol. 65, no. 1, pp. 95–128, 2003.

[67] E. D. Sontag, "Remarks on feedforward circuits, adaptation, and pulse memory," *IET Systems Biology*, vol. 4, no. 1, pp. 39–51, Jan 2010.

Bibliography

[68] H. K. Khalil, *Nonlinear systems*, 3rd ed. Upper Saddle River, NJ: Prentice-Hall, 2002.

[69] W. Zhang and D. N. Robinson, "Balance of actively generated contractile and resistive forces controls cytokinesis dynamics," *Proc. National Academy Sciences, U.S.A.*, vol. 102, no. 20, pp. 7186–7191, 2005.

[70] I. Mitchell, "The flexible, extensible and efficient toolbox of level set methods," *J. Scientific Computing*, vol. 35, no. 2-3, pp. 300–329, 2008.

[71] C. Shi, C.-H. Huang, P. N. Devreotes, and P. A. Iglesias, "Interaction of motility, directional sensing, and polarity modules recreates the behaviors of chemotaxing cells," *PLoS Computational Biology*, vol. 9, no. 7, p. e1003122, 7 2013.

[72] L. Li, S. F. Norrelykke, and E. C. Cox, "Persistent cell motion in the absence of external signals: A search strategy for eukaryotic cells," *PLoS ONE*, vol. 3, no. 5, p. e2093, 05 2008.

[73] D. Ambrosi, A. Gamba, and G. Cox, Serini, "Cell directional persistence and chemotaxis in vascular morphogenesis," *Bulletin of Mathematical Biology*, vol. 66, no. 6, pp. 1851–1873, 11 2004.

[74] D. Dormann and C. J. Weijer, "Chemotactic cell movement during *Dictyostelium* development and gastrulation," *Current Opinion in Genetics and Development*, vol. 16, no. 4, pp. 367–373, 2006.

[75] P. T. Caswell, H. J. Spence, M. Parsons, D. P. White, K. Clark, K. W. Cheng, G. B. Mills, M. J. Humphries, A. J. Messent, K. I. Anderson, M. W. McCaffrey, B. W. Ozanne, and J. C. Norman, "Rab25 associates with α51 integrin to promote invasive migration in 3d microenvironments," *Developmental Cell*, vol. 13, no. 4, pp. 496–510, 2007.

[76] M. Onsum and C. V. Rao, "A mathematical model for neutrophil gradient sensing and polarization," *PLoS Computational Biology*, vol. 3, no. 3, p. e36, 03 2007.

[77] A. Van Keymeulen, K. Wong, Z. A. Knight, C. Govaerts, K. M. Hahn, K. M. Shokat, and H. R. Bourne, "To stabilize neutrophil polarity, PIP3 and Cdc42 augment RhoA activity at the back as well as signals at the front," *J. Cell Biology*, vol. 174, no. 3, pp. 437–445, 2006.

[78] K. Subramanian and A. Narang, "A mechanistic model for eukaryotic gradient sensing: Spontaneous and induced phosphoinositide polarization," *J. Theoretical Biology*, vol. 231, no. 1, pp. 49–67, 2004.

[79] M. Otsuji, S. Ishihara, C. Co, K. Kaibuchi, A. Mochizuki, and S. Kuroda, "A mass conserved reaction-diffusion system captures properties of cell polarity," *PLoS Computational Biology*, vol. 3, no. 6, p. e108, 06 2007.

[80] A. B. Goryachev and A. V. Pokhilko, "Dynamics of Cdc42 network embodies a

Turing-type mechanism of yeast cell polarity," *FEBS Letters*, vol. 582, no. 10, pp. 1437–1443, 2008.

[81] U. Picchini, "SDE toolbox: Simulation and estimation of stochastic differential equations with Matlab." [Online]. Available: http://sdetoolbox.sourceforge.net

[82] D. Fuller, W. Chen, M. Adler, A. Groisman, H. Levine, W.-J. Rappel, and W. F. Loomis, "External and internal constraints on eukaryotic chemotaxis," *Proc. National Academy Sciences, U.S.A.*, 2010.

[83] M. Skoge, M. Adler, A. Groisman, H. Levine, W. F. Loomis, and W.-J. Rappel, "Gradient sensing in defined chemotactic fields," *Integrative Biology*, vol. 2, pp. 659–668, 2010.

[84] A. F. M. Marée, V. A. Grieneisen, and L. Edelstein-Keshet, "How cells integrate complex stimuli: The effect of feedback from phosphoinositides and cell shape on cell polarization and motility," *PLoS Computational Biology*, vol. 8, no. 3, p. e1002402, 03 2012.

[85] W. R. Holmes, B. Lin, A. Levchenko, and L. Edelstein-Keshet, "Modelling cell polarization driven by synthetic spatially graded rac activation," *PLoS Computational Biology*, vol. 8, no. 6, p. e1002366, 06 2012.

[86] H. Meinhardt, "Orientation of chemotactic cells and growth cones: models and mechanisms," *J. Cell Science*, vol. 112, no. 17, pp. 2867–2874, 1999.

Bibliography

[87] M. P. Neilson, D. M. Veltman, P. J. M. van Haastert, S. D. Webb, J. A. Mackenzie, and R. H. Insall, "Chemotaxis: A feedback-based computational model robustly predicts multiple aspects of real cell behaviour," *PLoS Biology*, vol. 9, no. 5, p. e1000618, 05 2011.

[88] I. C. Schneider and J. M. Haugh, "Quantitative elucidation of a distinct spatial gradient-sensing mechanism in fibroblasts," *J. Cell Biology*, vol. 171, no. 5, pp. 883–892, 2005.

[89] L. Tang, J. Franca-Koh, Y. Xiong, M.-Y. Chen, Y. Long, R. M. Bickford, D. A. Knecht, P. A. Iglesias, and P. N. Devreotes, "Tsunami, the *Dictyostelium* homolog of the fused kinase, is required for polarization and chemotaxis," *Genes and Development*, vol. 22, no. 16, pp. 2278–2290, 2008.

[90] C. Kabacoff, Y. Xiong, R. Musib, E. Reichl, J. Kim, P. A. Iglesias, and D. Robinson, "Dynacortin facilitates polarization of chemotaxing cells," *BMC Biology*, vol. 5, no. 1, p. 53, 2007.

[91] C.-H. Huang, M. Tang, C. Shi, P. A. Iglesias, and P. N. Devreotes, "An excitable signal integrator couples to an idling cytoskeletal oscillator to drive cell migration," *Nature Cell Biology*, 2013.

[92] S. Srinivasan, F. Wang, S. Glavas, A. Ott, F. Hofmann, K. Aktories, D. Kalman, and H. R. Bourne, "Rac and Cdc42 play distinct roles in regulating PI(3,4,5)P3

and polarity during neutrophil chemotaxis," *J. Cell Biology*, vol. 160, no. 3, pp. 375–385, 2003.

[93] S. K. Yoo, Q. Deng, P. J. Cavnar, Y. I. Wu, K. M. Hahn, and A. Huttenlocher, "Differential regulation of protrusion and polarity by PI(3)K during neutrophil motility in live Zebrafish," *Developmental Cell*, vol. 18, no. 2, pp. 226–236, 2010.

[94] E. Décavé, D. Rieu, J. Dalous, S. Fache, Y. Bréchet, B. Fourcade, M. Satre, and F. Bruckert, "Shear flow-induced motility of *Dictyostelium discoideum* cells on solid substrate," *J. Cell Science*, vol. 116, no. 21, pp. 4331–4343, 2003.

[95] E. S. Welf, S. Ahmed, H. E. Johnson, A. T. Melvin, and J. M. Haugh, "Migrating fibroblasts reorient directionality by a metastable, PI3K-dependent mechanism," *J. Cell Biology*, vol. 197, no. 1, pp. 105–114, 2012.

[96] K. M. Johansen and J. Johansen, "Recent glimpses of the elusive spindle matrix," *Cell Cycle*, vol. 1, no. 5, pp. 312–314, 2002.

[97] W.-L. Lee and P. Wadsworth, "New spindle morphogenesis model by Dynein, Nudel, and the spindle matrix," *Cell Research*, vol. 19, no. 1, pp. 529–531, 2009.

[98] C. Yao, Y. Ding, W. Cai, C. Wang, J. Girton, K. Johansen, and J. Johansen, "The chromodomain-containing NH2-terminus of Chromator interacts with histone H1 and is required for correct targeting to chromatin," *Chromosoma*, vol. 121, no. 2, pp. 209–220, 2012.

[99] B. Goodman, W. Channels, M. Qiu, P. Iglesias, G. Yang, and Y. Zheng, "Lamin B counteracts the kinesin Eg5 to restrain spindle pole separation during spindle assembly," *J. Biological Chemistry*, vol. 285, no. 45, pp. 35 238–35 244, 2010.

[100] L. Capalbo, P. P. D'Avino, V. Archambault, and D. M. Glover, "Rab5 GTPase controls chromosome alignment through lamin disassembly and relocation of the NuMA-like protein Mud to the poles during mitosis," *Proceedings of the National Academy of Sciences*, vol. 108, no. 42, pp. 17 343–17 348, 2011.

[101] J. Beaudouin, D. Gerlich, N. Daigle, R. Eils, and J. Ellenberg, "Nuclear envelope breakdown proceeds by microtubule-induced tearing of the lamina," *Cell*, vol. 108, no. 1, pp. 83–96, 2002.

[102] D. Salina, K. Bodoor, D. Eckley, T. A. Schroer, J. Rattner, and B. Burke, "Cytoplasmic Dynein as a facilitator of nuclear envelope breakdown," *Cell*, vol. 108, no. 1, pp. 97–107, 2011.

[103] A. Mogilner and E. Craig, "Towards a quantitative understanding of mitotic spindle assembly and mechanics," *J. Cell Science*, vol. 123, no. 20, pp. 3435–3445, 2010.

[104] K. S. Burbank, T. J. Mitchison, and D. S. Fisher, "Slide-and-cluster models for spindle assembly," *Current Biology*, vol. 17, no. 16, pp. 1373–1383, 2007.

[105] R. Loughlin, R. Heald, and F. Nédélec, "A computational model predicts *Xeno-*

pus meiotic spindle organization," *J. Cell Biology*, vol. 191, no. 7, pp. 1239–1249, 2010.

[106] A. Mogilner, R. Wollman, G. Civelekoglu-Scholey, and J. Scholey, "Modeling mitosis," *Trends in Cell Biology*, vol. 16, no. 2, pp. 88–96, 2006.

[107] F. J. Nédélec, "Computer simulations reveal motor properties generating stable antiparallel microtubule interactions," *J. Cell Biology*, vol. 158, no. 6, pp. 1005–1015, 2002.

[108] W. E. Channels, F. J. Nédélec, Y. Zheng, and P. A. Iglesias, "Spatial regulation improves antiparallel microtubule overlap during mitotic spindle assembly," *Biophysical J.*, vol. 94, no. 7, pp. 2598–2609, 2008.

[109] C. C. Poirier, Y. Zheng, and P. A. Iglesias, "Mitotic membrane helps to focus and stabilize the mitotic spindle," *Biophysical J.*, vol. 99, no. 10, pp. 3182–3190, 2010.

[110] A. E. Carlsson and D. Sept, "Mathematical modeling of cell migration," in *Biophysical Tools for Biologists, Volume One: In Vitro Techniques*, ser. Methods in Cell Biology. Academic Press, 2008, vol. 84, pp. 911–937.

[111] F. J. Nédélec, T. Surrey, A. C. Maggs, and S. Leibler, "Self-organization of microtubules and motors," *Nature*, vol. 389, pp. 305–308, 1997.

[112] P. Maddox, A. Desai, K. Oegema, T. J. Mitchison, and E. Salmon, "Poleward

microtubule flux is a major component of spindle dynamics and anaphase a in mitotic Drosophila embryos," *Cell Press*, vol. 12, no. 19, pp. 1670–1674, 2002.

[113] N. J. Ganem, K. Upton, and D. A. Compton, "Efficient mitosis in human cells lacking poleward microtubule flux," *Cell Press*, vol. 15, no. 20, pp. 1827–1832, 2005.

[114] A. Wilde, S. B. Lizarraga, L. Zhang, C. Wiese, N. R. Gliksman, C. E. Walczak, and Y. Zheng, "Ran stimulates spindle assembly by altering microtubule dynamics and the balance of motor activities," *Nature Cell Biology*, vol. 3, pp. 221–227, 2001.

[115] M. Hetzer, O. J. Gruss, and I. W. Mattaj, "The Ran GTPase as a marker of chromosome position in spindle formation and nuclear envelope assembly," *Nature Cell Biology*, vol. 4, pp. E177–E184, 2002.

[116] T. Mitchison and M. Kirschner, "Dynamic instability of microtubule growth," *Nature*, vol. 312, pp. 237–242, 1984.

[117] L. N. Weaver, S. C. Ems-McClung, J. R. Stout, C. LeBlanc, S. L. Shaw, M. K. Gardner, and C. E. Walczak, "Kif18a uses a microtubule binding site in the tail for plus-end localization and spindle length regulation," *Current Biology*, vol. 21, no. 17, pp. 1500–1506, 2011.

[118] R. D. Vale, T. S. Reese, and M. P. Sheetz, "Identification of a novel force-

generating protein, kinesin, involved in microtubule-based motility," *Cell*, vol. 42, no. 1, pp. 39–50, 1985.

[119] B. M. Paschal, S. M. King, A. G. Moss, C. A. Collins, R. B. Vallee, and G. B. Witman, "Isolated flagellar outer arm Dynein translocates brain microtubules in vitro," *Nature*, vol. 330, no. 6129, pp. 672–674, 1987.

[120] M. Caudron, G. Bunt, P. Bastiaens, and E. Karsenti, "Spatial coordination of spindle assembly by chromosome-mediated signaling gradients," *Science*, vol. 309, no. 5739, pp. 1373–1376, 2005.

[121] H. Y. Li, W. P. Ng, W. C. Hang, P. A. Iglesias, and Y. Zheng, "Coordination of chromosome alignment and mitotic progression chromosome-based Ran signal," *Cell Cycle*, vol. 6, pp. 1886–1895, 2007.

[122] T. Krouglova, J. Vercammen, and Y. Engelborghs, "Correct diffusion coefficients of proteins in fluorescence correlation spectroscopy. application to tubulin oligomers induced by Mg2+ and paclitaxel," *Biophysical journal*, vol. 87, no. 4, pp. 2635–2645, 2004.

[123] J. Howard, *Mechanics of Motor Proteins and the Cytoskeleton*, 1st ed. Sunderland, Massachusetts: Sinauer, 2001.

[124] D. Salina, K. Bodoor, P. Enarson, W. H. Raharjo, and B. Burke, "Nuclear

envelope dynamics," *Biochemistry and Cell Biology*, vol. 79, no. 5, pp. 533–542, 2001, pMID: 11716295.

[125] Y. Zheng, "A membranous spindle matrix orchestrates cell division," *Nat Rev Mol Cell Biol*, vol. 11, no. 7, pp. 529–535, 2010.

[126] G. Civelekoglu-Scholey, L. Tao, I. Brust-Mascher, R. Wollman, and J. M. Scholey, "Prometaphase spindle maintenance by an antagonistic motor-dependent force balance made robust by a disassembling lamin-B envelope," *J. Cell Biology*, vol. 188, no. 1, pp. 49–68, 2010.

[127] R. E. Carazo-Salas and E. Karsenti, "Long-range communication between chromatin and microtubules in *Xenopus* egg extracts," *Current Biology*, vol. 13, no. 19, pp. 1728–1733, 2003.

[128] V. Prahlad, M. Yoon, R. D. Moir, R. D. Vale, and R. D. Goldman, "Rapid movements of vimentin on microtubule tracks: Kinesin-dependent assembly of intermediate filament networks," *The Journal of Cell Biology*, vol. 143, no. 1, pp. 159–170, 1998.

[129] R. J. Leslie, R. B. Hird, L. Wilson, J. R. McIntosh, and J. M. Scholey, "Kinesin is associated with a nonmicrotubule component of sea urchin mitotic spindles," *Proceedings of the National Academy of Sciences*, vol. 84, no. 9, pp. 2771–2775, 1987.

[130] T. M. Kapoor and T. J. Mitchison, "Eg5 is static in bipolar spindles relative to tubulin: evidence for a static spindle matrix," *The Journal of Cell Biology*, vol. 154, no. 6, pp. 1125–1134, 2001.

[131] J. C. Gatlin, A. Matov, G. Danuser, T. J. Mitchison, and E. D. Salmon, "Directly probing the mechanical properties of the spindle and its matrix," *J. Cell Biology*, vol. 188, no. 4, pp. 481–489, 2010.

Vita

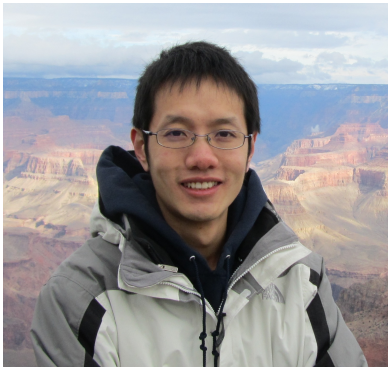

Changji Shi was born on July, 1985 in Changzhou, Jiangsu, China. In 2008, Changji Shi received his B.S. degree in Information Science and Control Theory from Tsinghua University in Beijing, China. Then, he enrolled in the Electrical and Computer Engineering Ph.D. program at Johns Hopkins University in 2008. Changji's research at Johns Hopkins University focuses on applying mathematical modeling to study biological processes: chemotaxis and mitosis.